UNIVERSITÄT DUISBURG ESSEN

Open-Minded

Time-Resolved X-Ray Diffraction from Coherent Acoustic Phonons Analyzed by Combining Microscopic Modeling with Deep Learning Based Strain Retrieval

Der Fakultät für Physik
der Universität Duisburg-Essen vorgelegte

Dissertation

zur Erlangung des akademischen Grades eines Doktors der Naturwissenschaften
(Dr. rer. nat.)

Autor:	Fabian Brinks
1. Gutachter:	Prof. Dr. Klaus Sokolowski-Tinten
2. Gutachter:	Prof. Dr. Sascha Schäfer
Datum der mündlichen Prüfung:	27. September 2022

Hiermit erkläre ich,

- dass ich die eingereichte Dissertation selbstständig verfasst habe.
- dass ich die Erlangung des akademischen Grades eines Doktors der Naturwissenschaften (Dr. rer. nat.) anstrebe.
- dass ich nur die angegebenen Hilfsmittel verwendet habe und alle wörtlich oder inhaltlich übernommenen Stellen als solche kenntlich gemacht habe.
- dass die vorliegende Arbeit weder im Aus- noch im Inland in gleicher oder ähnlicher Form einer anderen Prüfungsbehörde vorgelegt wurde.

Duisburg, 26. Juli 2022

Table of Contents

List of Figures

List of Tables

1 Abstract

A precise knowledge of microscopic processes in solids is key for the fundamental understanding of material properties. Those are determined by a complex interplay between the lattice, the electrons and other degrees of freedom. The dynamics of the different degrees of freedom upon ultrashort stimuli is of special interest, since it determines the reaction to energy deposition into such systems on ultrafast timescales. This defines the behavior of nano-scale devices, which are the backbone of our modern society dominated by electronics.

A very important aspect of this behavior is the dynamics of the lattice on ultrafast timescales. Structural dynamics are an inherent response of solid systems upon ultrashort stimuli. Whenever energy is deposited in a solid, it changes the stress inside the system. This leads to the excitation of strain waves, which represent a coherent superposition of acoustic phonons. Since stress and strain alter material properties, acoustic excitation allows for their transient modification or even manipulation.

A deeper understanding of the underlying microscopic processes opens the opportunity to generate tailored strain pulses. However, this requires a systematic quantitative knowledge over the important processes in relevant material systems.

In this work, the transient response of different metal/semiconductor heterostructures is investigated via time-resolved X-ray diffraction using a laser-plasma based X-ray source. Ultrashort optical pulses excite the electronic system of thin metal layers, whose properties define the shape of the excited acoustic pulse. An optical pump - X-ray probe scheme enables their direct time-resolved observation by monitoring the induced changes in the angle-resolved diffraction intensity.

By modeling the acoustic response and comparing the numerically calculated X-ray diffraction patterns to the experimental data, we aim to disentangle and quantify the relevant microscopic mechanisms. This thesis focuses on two metals - gold and palladium - with different properties in terms of electron-phonon coupling strength and transport on top of the technologically relevant semiconductor GaAs. Our analysis shows, that an interplay of these two mechanisms leads to a very different acoustic response.

Even though it is a proven tool for the analysis of picosecond acoustics, modeling of the acoustic response suffers from various problems. It is often challenging due to the high amount of potential microscopic influences and gets even more complicated for more complex systems and geometries.

Therefore, a new method for direct strain retrieval from time-resolved X-ray diffraction patterns based on deep neural networks is presented in this work. The described algorithm does not require an a priori physical model or any assumptions of the relevant mechanisms. By combining this new analysis tool with the modeling approach, we want to open new perspectives for the analysis of time-resolved X-ray diffraction experiments and their extension to more complex and non-ideal situations.

2 Zusammenfassung

Eine genaue Kenntnis der mikroskopischen Prozesse in Festkörpern ist der Schlüssel zum grundlegenden Verständnis ihrer Materialeigenschaften. Diese werden durch ein komplexes Wechselspiel zwischen dem Gitter, den Elektronen und anderen Freiheitsgraden bestimmt. Die Dynamik der verschiedenen Freiheitsgrade nach ultrakurzen Stimuli ist von besonderem Interesse, da sie die Reaktion auf die Energiedeposition in solchen Systemen auf ultraschnellen Zeitskalen bestimmt. Dies definiert das Verhalten von nanoskaligen Bauteilen, die das Rückgrat unserer modernen, von der Elektronik dominierten Gesellschaft sind.

Ein sehr wichtiger Aspekt dieses Verhaltens ist die Dynamik des Gitters auf ultraschnellen Zeitskalen. Strukturelle Dynamik ist eine inhärente Reaktion von Festkörpersystemen auf ultrakurze Stimuli. Wann immer Energie in einen Festkörper eingebracht wird, ändert sich die Spannung innerhalb des Systems. Dies führt zur Anregung von Verformungswellen, die eine kohärente Überlagerung von akustischen Phononen darstellen. Da Spannung und Dehnung die Materialeigenschaften verändern, ermöglicht die akustische Anregung eine transiente Änderung oder sogar Manipulation dieser Eigenschaften.

Ein tieferes Verständnis der zugrunde liegenden mikroskopischen Prozesse eröffnet die Möglichkeit, maßgeschneiderte Verformungsimpulse zu erzeugen. Dies erfordert jedoch ein systematisches quantitatives Wissen über die wichtigen Prozesse in relevanten Materialsystemen.

In dieser Arbeit wird die transiente Reaktion verschiedener Metall/Halbleiter-Heterostrukturen mittels zeitaufgelöster Röntgenbeugung unter Verwendung einer Laser-Plasma-basierten Röntgenquelle untersucht. Ultrakurze optische Pulse regen das elektronische System von dünnen Metallschichten an, deren Eigenschaften die Form des angeregten akustischen Pulses bestimmen. Ein Schema aus optischer Anregung zusammen mit Röntgenabfrage ermöglicht deren direkte zeitaufgelöste Beobachtung durch Messung der induzierten Änderungen in der winkelaufgelösten Beugungsintensität.

Durch die Modellierung der akustischen Antwort und den Vergleich der numerisch berechneten Röntgenbeugungsmuster mit den experimentellen Daten werden die relevanten mikroskopischen Mechanismen entschlüsselt und quantifiziert. Diese Arbeit konzentriert sich auf zwei Metalle - Gold und Palladium - mit unterschiedlichen Eigenschaften in Bezug auf die Stärke der Elektron-Phonon-Kopplung und den Transport auf dem technologisch relevanten Halbleiter GaAs. Unsere Analyse zeigt, dass ein Zusammenspiel dieser beiden Mechanismen zu einem stark unterschiedlichen akustischen Verhalten führt.

Obwohl sie ein bewährtes Werkzeug für die Analyse der Pikosekundenakustik ist, hat die Modellierung der akustischen Antwort verschiedene Probleme. Sie ist aufgrund der großen Anzahl potenzieller mikroskopischer Einflüsse oft eine Herausforderung und wird bei komplexeren Systemen und Geometrien noch komplizierter.

Daher wird in dieser Arbeit eine neue Methode zur direkten Ermittlung von Verformungen aus zeitaufgelösten Röntgenbeugungsmustern auf Grundlage von tiefen neuronalen Netzen vorgestellt. Der beschriebene Algorithmus erfordert kein physikalisches a priori Modell und keine Annahmen über die relevanten Mechanismen. Durch die Kombination dieses neuen Analysewerkzeugs mit dem Modellierungsansatz wollen wir neue Perspektiven für die Analyse von zeitaufgelösten Röntgenbeugungsexperimenten und deren Erweiterung auf komplexere und nicht-ideale Situationen eröffnen.

3 Introduction and Motivation

Elementary processes in solids such as electron-electron scattering, electron-phonon scattering or nuclear motion in general happen on ultrashort timescales [13]. The advent of sub-picosecond lasers has allowed for the direct observation of such processes leading to a constant growth of the field of pico- to femtosecond physics. These microscopic processes determine the macroscopic properties and the behavior of solids. Hence, a good understanding of condensed matter requires the precise exploration of these processes.

This is important from both a fundamental as well as a technological point of view. Our modern high-tech computers and communication devices depend on nanostructures operating at high frequencies. Technological progress aims to further miniaturize and accelerate devices. To allow for this, certain important questions have to be answered: How do nanostructures respond to ultrafast stimuli? How does energy relax on ultrashort time scales? How does heat in nanostructures flow and how can it be minimized? How can we trigger processes at increasing frequencies?

The lattice structure and its dynamics are an essential part of those microscopic processes. Thus, a good understanding of the lattice degrees of freedom is crucial for solid state physics. The motion of the lattice atoms is in general described by the excitation of acoustic or optical phonons, which can be incoherent as in the case of heating or coherent with a fixed phase relation. Picosecond acoustics, the coherent excitation of acoustic phonons, is an important aspect in this fields for various reasons.

Firstly, picosecond acoustic waves (PAW) can be thought of as the propagation of disturbances of the equilibrium lattice. A change of the lattice constant, also known as strain, travels in form of a wave. Strain is long known to alter material properties such as band structure, deformation potentials or carrier mobility [12, 30]. Accordingly, PAW are considered as a means to dynamically manipulate and control material properties and a deep understanding of them is key to get insight into the functionality of solid devices under non-equilibrium conditions.

Secondly, PAW are an important aspect for energy flow in nanostructures after impulsive excitation. Whenever energy is locally deposited into a system, this leads to heating. If the stimulus is short, this heating may happen on a timescale, on which the volume of the system cannot follow. Subsequently, the lattice relaxes to a new equilibrium state by emission of PAW [17]. These waves transport energy in the specific material at the speed of sound [46]. Therefore, PAW have to be taken into account, when investigating the energy flow in a structure after ultrafast excitation [75].

Thirdly, picosecond acoustics are an interesting tool to either investigate material properties or to control them. For instance, Brüggemann et al. and Czerniuk et al. have shown that they can use a PAW to trigger a layer of quantum dots and by that transiently enhance the photoluminescence efficiency of quantum dot lasers by more than two orders of magnitude [15, 22]. PAW also change the X-ray reflectivity of a sample. This can be deployed for the construction of ultrafast X-ray switches to cut out ultrashort X-ray pulses out of much longer ones [24, 45, 51, 70]. Even other disciplines than physics can benefit from knowledge in ultrafast acoustics. For example, mechanical properties of living cells can be studied non-invasively in their natural environments, which deepens our knowledge about the building blocks of life [91, 102]. This enumeration is far from complete and many more examples could be given (see e.g. [74, 110, 116]).

Consequently, picosecond acoustics is an active field of research for more than three decades. However, the combination of short time and microscopic length scales makes the investigation challenging.

First research has been done with all optical methods, namely optical reflectivity [129], interferometry [87] and deflectometry [138]. However, such methods can only indirectly probe the lattice behavior. Assumptions have to be made about the strain dependencies of the optical properties. This makes it difficult to achieve quantitative information as is discussed exemplary in references [14, 38].

Moreover, optical methods are limited to the penetration depth of the deployed light. In metals for example this limits the achievable depth information to some tens of nanometers depending on the wavelength.

This changed, when ultrashort X-ray and electron pulses became available. In contrast to optical pulses, X-rays can penetrate solids up to the micrometer or even centimeter scale. Accordingly, ultrafast diffraction was established as a powerful complementary tool to all optical methods. It can combine ultrafast (ps/fs) temporal with picometer spatial resolution. By that, they allow for direct probing and quantitative analysis of lattice dynamics.

Early work was done on simple materials to understand the elementary processes starting with common semiconductor materials. Rose-Petruck et al. measured the PAW excited in bulk GaAs after optical excitation with 800 nm pulses of 30 fs pulse duration with X-ray diffraction [100]. They could follow the atomic motion due to the excited strain pulse and were able to explain their results using the thermo-elastic model developed by Thomsen et al. [129]. Furthermore, they could also describe their experimental data by numerically reconstructing the strain pulse using a genetic algorithm. However, the agreement to the data was slightly worse than the result of the modeling.

Chin et al. have performed early work on InSb crystals and found evidence for a delayed onset of the lattice response due to energy relaxation processes and the acoustic traveling time [20]. Experiments with higher resolution by Lindenberg et al., Reis et al. and Larsson et al. allowed for a more detailed analysis [69, 96, 63]. They measured the oscillations of the coherent acoustic phonons directly and showed that a finite electron-phonon coupling time in InSb has to be assumed to describe the diffraction data.

Ge was studied in bulk as well as in thin films. DeCamp et al. used anomalous transmission as a bulk sensitive probe and isolated the effects of electron-phonon coupling and diffusion to be dominant for the relaxation of the excitation energy into stress and subsequently acoustic waves [24, 25].

A new degree of freedom is introduced into the problem, if the confinement of the excitation into a thin film creates a discontinuity, namely an interface, which changes the excitation dynamics of PAW. Cavalleri et al. have studied Ge films on Si crystals [17]. By systematically varying the excitation fluence, they could compare different sources of energy loss in the film. They found loss of energy due to PAW transmission across the interface to be dominant for low fluences, while mode conversion due to anharmonic interactions becomes important for higher fluences.

By going to even higher fluences, non-thermal melting of the Ge sets in. For carefully chosen experimental conditions, this happens only for a fraction of the film. The additional interface between molten and solid Ge provides another source for reflection and transmission and leads to additional acoustic signatures in the ultrafast X-ray diffraction signals [132].

Early work on metals was done by Chen et al. with experiments on gold in 1996 [19]. However, they were only able to analyze the surface strain, because of their limited resolution. More detailed studies were performed by Nicoul et al. who used high temporal and angular resolution experiments of a single crystalline Au film on a Mica substrate to investigate the rocking curve shift. They concluded that a fully thermal model is not sufficient to describe the oscillation of the rocking curve shift and deduced, that a combination of electronic and thermal stress contributions together with a finite electron-phonon coupling time of $\tau = 5\,\mathrm{ps}$ was responsible for the measured changes to the oscillation offset and frequency [83].

Lu et al. looked at a freestanding polycrystalline gold film. They have demonstrated that an analysis of the underlying acoustics is also possible in thin samples in the Debye-Scherrer geometry. They showed, that the results of Nicoul et al. could describe their measurements. Even though, the resolution of the experiment was not sufficient to discriminate the model introduced by Nicoul et al. from a simpler one with an instantaneous increase of the phononic stress [72].

Gao et al. looked at similar Au films on Ge [33]. Their discussion focused on the phonon modes present in the PAW. These depend on the thickness of the films as well as on the relation between the acoustic properties of the film and the substrate. This was shown in a similar manner for Ni films on InSb [88, 89]. Again, the inclusion of diffusion processes was crucial to explain the experimental findings.

Jarnac et al. studied Au films on InSb [51]. They applied a model of masses and springs to understand the stress and strain generation and found their sample system to be suitable for the construction of an X-ray switch [113].

Park et al. [86] and Nie et al. [84] have investigated the lattice response of optically excited Al films using ultrafast electron diffraction. They could show, that a thermal as well as an electronic stress contribution is required to describe the observed lattice vibrations and could by that determine the electronic Grüneisen constant of Al.

Experiments on Cu films found similar effects to gold [66]. The combination of a two temperature model with a finite electron-phonon coupling time and diffusion effects describes the energy relaxation and strain generation.

Aside of that, more complex materials are also accessible for investigations of coherent acoustic phonons using time-resolved X-ray diffraction and yield new insights into such technologically relevant materials. For example, heterostructures of GaAs and AlGaAs can be used for mode selective excitation of strain waves [9]. The periodicity of the superlattice determines the dominantly excited phonon wave vectors.

The coupling of different phonon modes in a heterostructure was systematically studied by Bach and Schäfer by calculating the strain wave propagation after optical excitation in a Pt/Si bilayer for different configurations of the elastic properties [7]. Their theoretical approach allowed for the variation of different material properties and hence gave insight into the coupling of the modes for various configurations.

Magnetic materials give access to another degree of freedom: The spin system and corresponding magnetic components to the stress generation. For instance, this can be seen in the ferromagnets nickel [136] and gadolinium [57] or in heterostructures of $\mathrm{TbFe_2}$/Nb. Excitation of spins can lead to magnetostriction stress, which has the special property, that it can have both signs. It can therefore induce rarefaction as well as compression of a material upon optical excitation in contrast to electronic or thermal stress. This opens up new perspectives and makes these materials an interesting field of study [133, 134, 141].

Another important class of materials are oxides. For their work on $\mathrm{LuMnO_3}$, Lee et al. extended the theory of coherent phonon propagation by taking into account the hexagonal crystal structure of this perovskite. A strong coupling between the strain propagation axis and the perpendicular plane presents an additional loss channel for the excitation energy and results in damping [65].

Coupling to in-plane modes is also important in the structurally imperfect films of $\mathrm{PbZr_{0.2}Ti_{0.8}O_3}$ studied by Schick et al. [112]. However, in this case the coupling strength depends on the sign of the strain. Rarefaction parts cannot further expand the small crystallites in plane, but they can be compressed. Therefore only compression waves can couple.

It is not straight forward to quantitatively measure the strain distribution locally. Feist et al. have used ultrafast convergent beam electron diffraction to probe optically excited graphite membrane nanostructures [28]. By combining their observations with numerical simulations, they were able to extract the relevant transient elements of the strain tensor with high temporal and spatial resolution.

Wen et al. and Schick et al. studied the response of $BiFeO_3$ and found surprisingly long relaxation times. $BiFeO_3$ is a multiferroic material, which means that it combines ferroelectric with ferromagnetic properties, making it an interesting candidate for possible applications. Wen et al. proposed a new mechanism for the energy relaxation to explain their findings. They assume that the excited electrons stay localized due to the polarization field in the unit cell, while they rest in states at the bottom of the conduction band for a long time. The interplay of these electrons with the polarization field yields a long lasting strain (on the order of nanoseconds) in the material [115, 137].

A last example to be mentioned here is the combination of $SrRuO_3$ with $SrTiO_3$. This is a good model system for the study of PAW, because due to the nearly matched acoustic impedances of the two materials, there is no relevant reflection at the interface. This allows for systematic experiments as by Schick et al., where they varied the film thickness in comparison to the relevant excitation length and studied the effect on the ultrafast diffraction signal [114]. By careful preparation of the surface and interface, this system also allows for the investigation of high frequency phonons at the boundary of the Brillouin zone [119].

In a different sample geometry, Shayduck et al. deployed a superlattice of the two materials and by that were able to emit a quasi-monochromatic strain wave [120]. They could analyze the damping of this wave and showed, that it can be well described by Akhiezer's $\frac{1}{\omega^2}$ sound attenuation law [3].

For the controlled emission of PAW waves into arbitrary materials, for instance materials which are transparent for the applied laser light, so called opto-acoustic transducers are an interesting class of heterostructures. They are composed of a thin film, often a metal, on top of the material of interest. By carefully choosing the film material and its properties, the emission of designed acoustic pulses into various substrates is possible.

This work reports about time resolved X-ray diffraction experiments on the transient acoustics of different metal films on a semiconductor substrate. By "forward" modeling the acoustic response upon ultrafast optical excitation, the underlying physical processes of strain generation are disentangled and the influence of transport and electron-phonon coupling on the resulting shape of the PAW are identified.

The approach of forward modeling is widely used in the literature discussed so far. It starts from simulating the physics upon laser excitation and subsequently compares the calculated diffraction signals to corresponding experimental data. The best physical model is identified by the iterative application of this scheme. Contrary, a direct retrieval of the acoustic behavior would circumvent the requirement for a microscopic model, initially.

The wide use of the modeling approach originates from the fact, that diffraction experiments suffer from the phase problem [41]. In experiments, where the intensity of a wave is measured, the phase information is lost and, therefore, a direct retrieval of the wave is challenging.

Translated to ultrafast acoustics this means that on the one hand it is comparably easy to calculate the diffracted X-ray intensity for a known strain distribution using dynamical X-ray diffraction theory (see chapter 4.1.3). On the other hand, it is challenging to calculate back to the strain distribution from a measured diffraction pattern.

One way to work around this is the forward modeling approach described previously. This has proven to be a successful way of analyzing the results of diffraction experiments on PAW in solids. Nevertheless, it suffers from some major problems.

Firstly, different physical processes such as subsystem coupling, electronic and thermal transport or acoustic damping might play a role and have to be taken into account. This often requires a lot of iterations to differentiate between important and negligible effects. Additionally, the modeling is often based on simplifying models such as the two temperature model (TTM) [6], which may be only valid for certain conditions. Secondly, physical constants necessary to model the acoustics may be unknown for certain materials or may have some complicated dependencies on other parameters like the temperature.

Therefore, it would be desirable to have a complementary method to determine the strain directly from a measured diffraction pattern. This would not replace the modeling, but could increase its efficiency. In the following, such an approach will be called *direct strain retrieval.*

There have already been proposals to retrieve the transient strain after optical excitation. Gao et al. separated the strain pulse into single phonon modes and tried to extract their amplitude and phase from the Fourier transform of the time dependent X-ray diffraction intensity [32]. Lai et al. exploited the Fano resonance of an acoustic wave at a free surface in an all optical pump-probe scheme to reconstruct the underlying strain pulse [61]. Since, their method requires the acoustic wave to be reflected inside the sample to travel back to the free surface in order to be reconstructed, it is not generally applicable.

Moreover, both methods require to make assumptions on the underlying physics. Here, we propose a new method based on deep neural networks trained by artificial strain pulses and corresponding calculated X-ray diffraction patterns to analyze the results of time-resolved X-ray diffraction experiments.

Deep neural networks have proven to be very efficient in various fields such as speech recognition [47], language translation [125], particle physics data analysis [21], drug development [73] and image recognition [59, 27, 130]. In fact, the field of image recognition deals with analyzing tasks on 2-dimensional input data. The basic idea of our approach is, that the input data cannot only be real images, but also other 2D data, e.g. time-resolved X-ray diffraction data. We therefore want to build on that and take advantage of the accomplishments already achieved in the field of deep learning.

In this work it is shown, that deep neural networks can be trained to analyze transient diffraction signals from optically excited solids. For training a deep neural network, large sets of already labeled data pairs are required. As has been discussed, calculating the X-ray diffraction pattern for a known strain distribution is possible. We use randomly created strain pulses and corresponding calculated diffraction patterns to train a neural network specialized on image recognition.

Deep neural networks use representation learning. This means, that the features of the input data (e.g. structures in the diffraction pattern) which are important for classification are not defined beforehand by the programmer, but are independently extracted by the network. Hence, the model does not require any "knowledge" on the physical processes to interpret the diffraction data.

The discussed points are elaborated in the course of this thesis. It is structured as follows: Chapter 4 introduces the relevant theoretical concepts. Most importantly, these are the basics of X-ray diffraction and dynamical X-ray diffraction theory, picosecond acoustics in solids and deep neural networks with a focus on image analysis. In chapter 5, the experimental setup for time-resolved X-ray diffraction measurements is introduced. The experimental results are subsequently discussed in the result sections 6 and 7 with a focus on two model systems with very weak and very strong electron-phonon coupling: Gold and palladium. In chapter 6, the experiments are interpreted quantitatively by developing a model for the microscopic processes upon ultrashort optical excitation. Transient as well as fluence dependent analysis of the underlying mechanisms and a comparison to the experimental data justify the given model. In chapter 7 a novel algorithm for the analysis of picosecond acoustic experiments is developed and investigated on artificial as well as on experimental data. Finally, the findings are summarized and an outlook is given in part 8.

4 Theoretical Background

In this section, a brief theoretical background is given, which provides the foundation to understand the content of this dissertation. An exhaustive treatment of all these topics is beyond the scope of this work. Further information can be found in the literature cited in the respective sections.

4.1 X-Ray Diffraction

This introduction into structural analysis with X-ray diffraction is based on the books of Ibach and Lüth, Charles Kittel as well as Als-Nielsen and McMorrow [5, 50, 55]. It gives a short overview of the basic properties of X-rays and their application in the analysis of the atomic structure of matter. Additionally, the generation of ultrashort X-ray pulses is discussed, which allows for the time resolved investigation of structural dynamics.

4.1.1 X-Rays

Since the discovery of X-rays by Wilhelm Conrad Röntgen in 1896 [107], they have become a powerful tool in different fields of research and technology: For example in modern medicine, X-rays are an indispensable tool for diagnostics, in engineering, they allow for non-invasive material testing (e.g. quality of welds, bonds in microelectronics...) and in physics they have opened the opportunity to investigate the structure of matter on an atomic scale. The latter one will be the focus of this work.

X-rays are electromagnetic waves positioned between ultraviolet and gamma radiation in the electromagnetic spectrum. Their wavelength covers a huge range from 10 nm down to 1 pm. This corresponds to photon energies of approximately 100 eV up to 1 MeV.

The exploration of the structure of matter is one of the most important applications of X-rays in natural sciences and will be described in the following.

4.1.2 Crystal Structure and Diffraction

Crystals are of special interest in many fields. A crystal is a very symmetric form of condensed matter, where a general building block, the so called base, is repeated periodically. The positions of all the bases in the crystal are called the lattice. A crystal is therefore defined by its base and its lattice. The base can consist of one atom as for many metals, or it can consist of several atoms as in GaAs or NaCl. Even complex molecules like proteins can crystallize and form crystals with bases of thousands of atoms.

The lattice is spanned by the base vectors $\vec{x}$, $\vec{y}$ and $\vec{z}$. They are defined by the fact, that every lattice vector $\vec{r}$ can be written as a linear combination of the base vectors:

$$\vec{r} = a\vec{x} + b\vec{y} + c\vec{z}, \tag{1}$$

with $a, b, c \in \mathbb{Z}$. The volume spanned by the base vectors is called a unit cell. The unit cell with the smallest possible volume is named the primitive unit cell.

Crystals normally contain a lot of differently oriented lattice planes. The so called Miller indices are a common solution for labeling these families of planes. They are denoted as (hkl) and are defined such that the plane intersects the axes spanned by the base vectors $\vec{x}$, $\vec{y}$ and $\vec{z}$ at position $(\frac{x}{h}, \frac{y}{k}, \frac{z}{l})$, where x, y, and z are the lengths of the base vectors. There are different sets of numbers fulfilling this condition. The Miller indices are the set with the smallest possible integer numbers out of these.

Crystals distinguish themselves from other forms of matter like amorphous solids or liquids by their long range order. The strain waves investigated in this work are perturbations of that order and their extension is large in comparison to the lattice constant.

Therefore, we use diffraction to study these phenomena, which is well suited for measuring long range periodicity and its perturbations.

Crystals are of immense importance, since our modern technology is largely built on crystalline semiconductors like silicon. Because of that, it is essential to understand the structure of crystals and its transient response to short stimuli.

To start with, the structural analysis of equilibrium solids by diffraction will be discussed. Successively, this will be extended to transient effects in chapter 4.2.

To analyze the atomic structure of solids, one has to use a probe with a wavelength in the order of the interatomic distances in the specimen of interest. This could either be high energetic particles with their De Broglie wavelength

$$\lambda_B = \frac{hc}{E}, \tag{2}$$

where $h = 6.63 \times 10^{-34}\,\mathrm{J\,s}$ is Planck's constant, $c = 2.998 \times 10^{8}\,\frac{\mathrm{m}}{\mathrm{s}}$ is the speed of light and E is the energy of the particles. For diffraction experiments, electrons and neutrons are common choices.

The other option is the use of photons. The interatomic distances between lattice planes in solids are in the order of an angstrom, so the suitable electromagnetic waves are X-rays. This is also the experimental tool in this work. For that reason, the following discussion will focus on the diffraction with X-rays.

Imagine an X-ray beam incident on a crystal. Some X-rays may be scattered at atoms of the first lattice plane, while some others are scattered at the second. As can be seen in figure 1, the path difference (shown in red) of the two beams is given by $\Delta s = 2d\sin(\theta)$. The X-rays scattered at the atoms of different lattice planes interfere constructively, if the path difference is an integer multiple of the X-ray wavelength λ. Therefore, the condition for constructive interference is:

$$2d\sin(\theta_B) = n\lambda, \tag{3}$$

with the lattice constant d, the Bragg angle θ_B and the order of the diffraction peak n. This is the famous law formulated by William Lawrence Bragg in 1912.

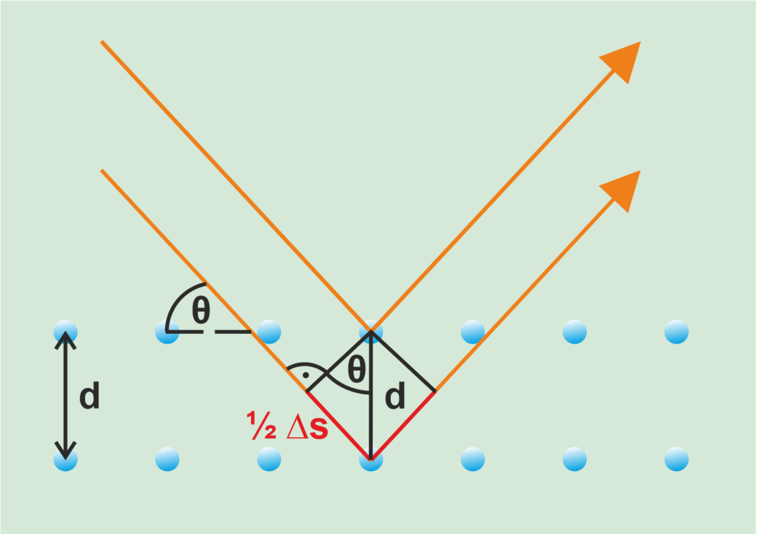

Figure 1: **Derivation of the Bragg equation from geometrical considerations.** Incoming X-rays, which are reflected by atoms of different lattice planes, interfere constructively, if the path difference is an integer multiple of the X-ray wavelength. The path difference is connected to the geometrical parameters by $\sin\theta = \frac{\frac{1}{2}\Delta s}{d}$.

It is instructive to also formulate the diffraction condition in reciprocal space, which is the Fourier transformed real space. The result is the so called Laue equation. The path difference between two rays scattered at lattice points with distance vector $\vec{R} = \vec{r} - \vec{r}'$ is given by $\Delta s = \vec{R} \cdot (\frac{\vec{k}}{k} - \frac{\vec{k}'}{k'})$. Inserting $\Delta s = n\lambda$ and the wave vector definition $k = \frac{2\pi}{\lambda}$ yields:

$$\vec{R} \cdot (\vec{k} - \vec{k}') = 2\pi n. \tag{4}$$

This equation can only be fulfilled, if the difference of the incoming and outgoing wave vectors equals a reciprocal lattice vector $\vec{G}$, which is defined by $e^{i\vec{R}\cdot\vec{G}} = 1$. With this, one gets the Laue equation:

$$\vec{k} - \vec{k}' = \vec{G}. \tag{5}$$

The Laue equation can be represented graphically using the Ewald sphere as depicted in two dimensions in figure 2. The Ewald sphere is a sphere with radius $|\vec{k}|$ in three dimensions and a circle in two dimensions. The points represent the lattice in reciprocal space. Whenever two points of the reciprocal lattice lie on the sphere, a Bragg peak connected to the reciprocal lattice vector between these two points occurs. The wave vectors of the incoming and the diffracted wave $\vec{k}$ and $\vec{k}'$ start at the center of the Ewald sphere and end on the two reciprocal lattice points on it.

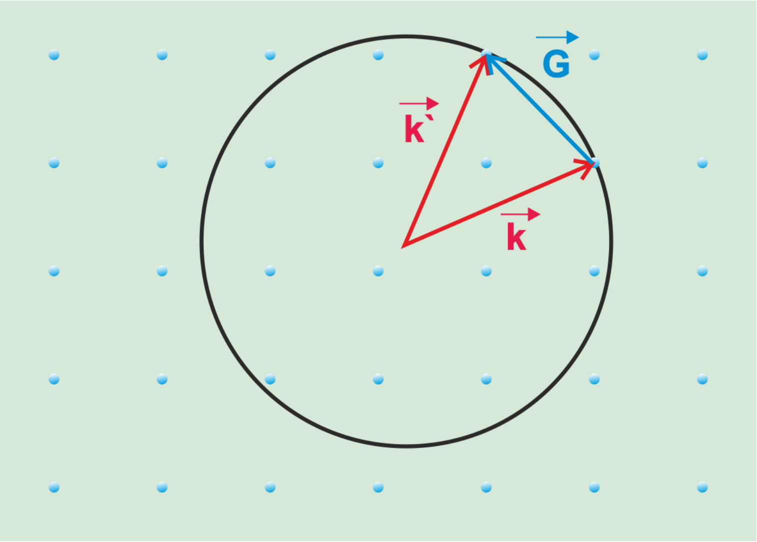

Figure 2: **Diffraction in reciprocal space: The Ewald sphere.** A Bragg peak occurs, when two reciprocal lattice points lay on the Ewald sphere spanned by the k-vector of the incoming and outgoing X-rays. The diffraction peak position is given by the reciprocal lattice vector $\vec{G}$ connecting the two points.

Equations 3 and 5 only predict at which angles or wave vectors, respectively, a Bragg peak occurs. But they do not make any statement about the intensity distribution of the diffracted X-rays. This will be examined in the following.

In a solid, X-rays are scattered by electrons. Therefore, if one wants to calculate the intensity of scattered X-rays, one has to look at the electron distribution. Usually, most of the electrons in a solid are located close to the atom cores, the so called inner shell electrons. Accordingly, the positions of the atoms in the lattice are relevant for the diffraction signal.

The structure factor F is a quantity, which describes how rays are scattered by a material. It is normally given as a function of the scattering vector $\vec{Q}$, which is defined by:

$$\vec{Q} = \vec{k} - \vec{k}' \tag{6}$$

with the wave vectors of the incoming and outgoing waves $\vec{k}$ and $\vec{k'}$, respectively. It is the momentum transfer during the scattering event.

For a crystal, the structure factor for a given scattering vector can be written as:

$$F^{\text{crystal}}(\vec{Q}) = \sum_{r_j} F_j^{\text{atom}}(\vec{Q}) e^{i\vec{Q}\cdot\vec{r_j}} \sum_{R_n} e^{i\vec{Q}\cdot\vec{R_n}}. \tag{7}$$

In this equation, the first sum is the so called unit cell structure factor and describes the scattering of X-rays by a unit cell of the crystal. The sum goes over all the atoms building the unit cell, which are located at the positions r_j. It contains the structure factor of the single atoms F_j^{atom}, which is essentially the Fourier transform of the electron distribution of the specific atom, and a phase factor $e^{i\vec{Q}\cdot\vec{r_j}}$.

The second summation goes over all lattice sites R_n, which are the positions where all the bases are located. It sums up their contributions, which also have to be weighted by a phase factor. This factor gives the maximum contribution, when equation 4 is fulfilled and thus it depicts the Bragg and Laue condition. Only then, the contributions of all the atoms add up.

Equation 7 has to be evaluated in order to describe the intensity in a diffraction experiment. There are two theories dealing with that: The kinematical and the dynamical theory of X-ray diffraction. The kinematical description is a limiting case of the dynamical one, which neglects multiple scattering events, extinction, absorption and refraction. It is therefore only applicable for "small" samples (e.g. thin films), where the probability of multiple scattering events is sufficiently low.

In dynamical diffraction, all these effects are taken into account. The following discussion will focus on dynamical X-ray diffraction theory, since the experiments in this work are done on bulk samples. The thickness of these samples is much larger than the penetration depth of the utilized X-rays and multiple scattering, extinction, absorption and refraction are therefore not negligible.

4.1.3 Dynamical X-Ray Diffraction

There are two ways of solving the problem of diffraction from a thick crystal. The first one is to describe the crystal as a stack of a large number of layers and calculate the reflected and transmitted waves for each of these layers. This approach was described by Darwin in 1914.

An equivalent way is, to view the crystal as a dielectric medium and solve Maxwell's equations with the appropriate boundary conditions. This was first done by Ewald (1916 - 1917) and reformulated by Laue in 1931. This theory was extended to distorted crystals by Takagi and Taupin, who formulated the so called Takagi-Taupin equation [127, 128]. Klar and Rustichelli [56] have introduced a new formulation, which was further elaborated by Larson et al. [62]. They have shown, that the scattering amplitude X fulfills the differential equation:

$$i\frac{dX}{dA} = X^2(1+ik) - 2X(y+ig) + (1+ik). \tag{8}$$

$X(A)$, the complex scattering amplitude, is a function of the reduced spatial coordinate, which is given by:

$$A = \frac{r_{\text{e}} k_{\text{pol}} f'(\psi) e^{-M} \lambda t}{V_{\text{c}}\sqrt{|\gamma_0 \gamma_{\text{H}}|}}, \tag{9}$$

where $r_e = 2.82 \times 10^{-15}\,\mathrm{m}$ is the classical electron radius, $f(\psi)$ is the structure factor for the scattering angle ψ with its real part $f'(\psi)$ and its imaginary part $f''(\psi)$, e^{-M} is the Debye-Waller factor, which describes the reduction of the scattering intensity due to thermal vibrations, λ is the wavelength of the X-rays, t is the depth inside the crystal, V_c is the volume of a unit cell and γ_0 and γ_H are the projections of the incident and diffracted wave vector on the surface normal, respectively.

k_pol is the polarization factor of the X-rays, which is defined by:

$$k_\mathrm{pol} = \begin{cases} 1 & \text{for s-polarization} \\ \cos(\psi) & \text{for p-polarization} \end{cases} \tag{10}$$

Equation 8 can be separated into two differential equations for the real and imaginary part:

$$\begin{aligned} \frac{dX_1}{dA} &= k(X_1^2 - X_2^2 + 1) + 2X_2(X_1 - y) - 2gX_1 \\ \frac{dX_2}{dA} &= -(X_1^2 - X_2^2 + 1) + 2X_1(X_2 k + y) - 2gX_2 \end{aligned} \tag{11}$$

Prior to solving these equations, the included parameters have to be calculated. Absorption of X-rays is described by the parameters g and k, which are defined by:

$$\begin{aligned} g &= -\frac{f''(0)(1+b)}{2k_\mathrm{pol} f'(\psi) e^{-M} \sqrt{|b|}}, \\ k &= \frac{f''(\psi)}{f'(\psi)}. \end{aligned} \tag{12}$$

In this equations, $b = \frac{\gamma_0}{\gamma_\mathrm{H}}$ is a measure of the asymmetry of the reflection.

The dimensionless parameter y gives the deviation of the angle from the Bragg angle:

$$y = \frac{b\pi V_\mathrm{c} \sin(2\theta_\mathrm{B})(\Delta\theta + \eta(A)\tan(\theta_\mathrm{B}))}{k_\mathrm{pol}\lambda^2 r_\mathrm{e} f'(\psi) e^{-M}\sqrt{|b|}} - \frac{(1+b)f'(0)}{2k_\mathrm{pol} f'(\psi) e^{-M}\sqrt{|b|}}. \tag{13}$$

$\Delta\theta = \theta - \theta_\mathrm{B}$ is the deviation from the Bragg angle and $\eta(A)$ is the strain of the sample at depth A.

Given all these results, the system of equations 11 can be solved numerically. The reflectivity of the crystal is then given by:

$$R = |X(0)|^2. \tag{14}$$

One gets the diffraction pattern $I(\theta)$, if this is done for all angles of interest and a given strain distribution. The code for the numerical solution of equation 11 can be found in the appendix of the dissertation of Afshari [1]. The calculated unpumped diffraction patterns have been compared to the ones obtained with the XOP-package [108] to verify the correctness of the code.

The described procedure can be extended to transient effects easily. A time dependent strain distribution $\eta(A, t)$ is assumed instead of a static one. The problem is therefore reduced to the knowledge of the transient strain distribution.

4.2 Ultrashort X-Ray Pulses

Pump-probe schemes are a commonly used tool to investigate transient phenomena in the fs- to ps-time range, because they allow to directly follow the evolution of such phenomena in time. A first short pulse excites the specimen to a non-equilibrium state and a second pulse probes the state after a time delay Δt. This yields a stroboscopic movie of the specimen's evolution in time by repetition with systematical variation of the time delay.

The pump pulse is often an optical or near infrared pulse. Such pulses are commonly generated in a Ti:Sa-oscillator, which uses a titanium doped sapphire (Al_2O_3) crystal as the laser medium. The broad range of supported frequencies in this material allows for the production of very short laser pulses. However, different wavelengths, e.g. UV-pulses or THz-pulses, or even something different like a particle pulse can also serve as the pump. The choice of pump depends on the kind of excitation one wants to make.

The probe pulse has to be chosen regarding the subject of investigation. X-rays are a suitable tool to study structural dynamics, because their wavelength is in the order of the interatomic distances and, therefore, they allow to directly probe lattice dynamics.

The time resolution of a pump-probe experiment is defined by the duration of the probe pulse. Therefore, in order to achieve sufficient time resolution, one has to use correspondingly short pulses. The time scale of the acoustic phenomena studied in this work can be estimated to $t = \frac{s}{c} \approx 2\,\mathrm{ps}$ by assuming a typical length scale to be the penetration depth of light in metals of $s \approx 10\,\mathrm{nm}$ and a typical sound velocity in solids of $c \approx 5\,\frac{\mathrm{nm}}{\mathrm{ps}}$. Hence, X-ray pulses with sub-picosecond duration are well suited for investigating ultrafast acoustics.

In this work, X-rays produced on a laboratory scale in a so called laser-plasma based source are utilized. The general operating principle will be explained in the following. A more detailed description of the actual source can be found in chapter 5.

The principle idea for the generation of ultrashort X-ray pulses is to use a triggering process, which is ultrashort itself. It is long known, that an intense laser pulse creates a high-density surface plasma, when focused onto a solid target [23]. Such a plasma contains free electrons. Some electrons are accelerated to kinetic energies up to a few tens of keV by interaction with the laser field and are often referred to as "hot" electrons [103]. The intensity of the pulse has to be on the order of 10^{16}–$10^{18}\ \frac{\mathrm{W}}{\mathrm{cm}^2}$ to make the creation of "hot" electrons an effective process [2, 95].

If these "hot" electrons penetrate the "cold" solid underneath the surface, X-rays with a spectrum comparable to a common X-ray tube are produced. It contains Bremsstrahlung and characteristic radiation [107]. The process is depicted in figure 3.

Bremsstrahlung is generated by the acceleration of electrons in the vicinity of ion cores and yields a continuous spectrum, which can extend up to the maximum kinetic energy of the laser-accelerated electrons. Characteristic radiation is produced, when hot electrons kick out inner shell electrons from the atoms. For that, their energy has to be higher than the impact ionization threshold. Subsequently, outer shell electrons fall into the empty states and emit X-rays. The energy of that kind of radiation is determined by the shell energies of the solid material and the involved transitions. The following notation is usually used to specify a particular transition. A Latin letter indicates the final shell and a Greek letter the initial shell of the transition. For example, K_α describes radiation emitted in a transition from an L-shell (quantum number 2) to a K-shell (quantum number 1). This can be further divided into two lines with slightly different energy, since the L-orbitals experience a spin-orbit split. This is denoted by an additional subscript number e.g. $K_{\alpha 1}$.

If the duration of the utilized laser pulse is short enough, it is plausible that also the emitted X-ray pulse's duration is in the order of the laser pulse duration. Indeed, Reich et al. [94] have studied the temporal length of such X-ray pulses for different

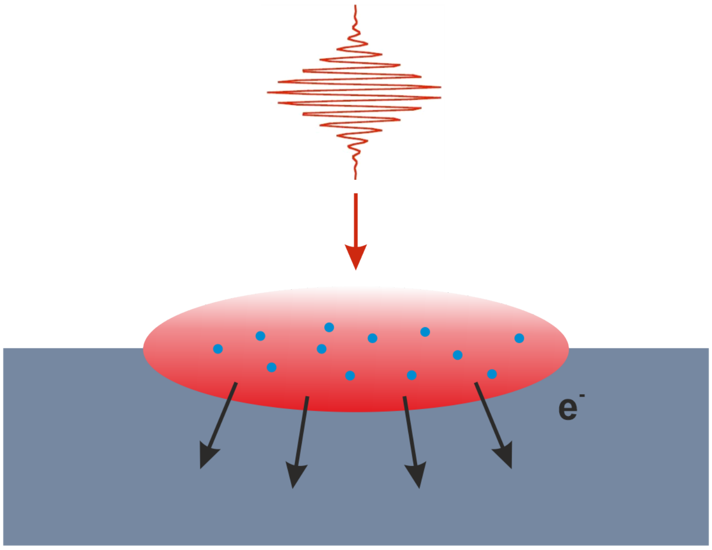

Figure 3: **Production mechanism for X-rays in a laser plasma source.** The X-rays are produced by hot plasma electrons, accelerated by the laser field and subsequently hitting the solid target.

excitation conditions as well as the expected photon yield. They found, that generation of approximately 100 fs short X-ray pulses is possible using a 60 fs laser pulse. The difference is attributed to the so called afterglow: Even when no more electrons get accelerated after the laser pulse has terminated, X-rays are emitted as long as some hot electrons still have energies above the ionization threshold [1, 94].

Anyway, pulse durations well below a picosecond are possible as has been shown in many time-resolved X-ray diffraction experiments [2, 29, 40, 71, 81, 142]. This is more than sufficient for studying ultrafast acoustics.

4.3 Picosecond Acoustics

This section introduces the principles of picosecond acoustics, the connection of elasticity theory and phonon picture and how picosecond acoustic waves change X-ray diffraction patterns.

4.3.1 Acoustic Waves

Solid matter can be deformed by internal and external stimuli, e.g. mechanical stimuli, temperature variations or changes of the potential energy landscape of the lattice. This section introduces the necessary physical quantities to describe such deformations and the propagation of local deformations as waves, namely acoustic or strain waves. These can be described in the linear theory of elasticity. The discussions in this chapter are based on the books of Bedford and Drumheller [10] and Gross [39].

The shape of a rigid solid can be fully characterized by the position vector $\vec{r}$ for every material point. A deformation can then be described by the displacement vector $\vec{u}$, which is defined as the change of position of every material point:

$$\vec{u}(\vec{r}) = \vec{r} - \vec{r}'. \tag{15}$$

If a solid is deformed, the distances between two points might change. The strain tensor $\boldsymbol{\eta}$ is a measure for the change of the length of a line element. It is a second order tensor and its elements can be calculated as

$$\eta_{km}(\vec{r}) = \frac{1}{2}(\frac{\partial u_k}{\partial x_m} + \frac{\partial u_m}{\partial x_k}), \tag{16}$$

where x_i are the respective spatial coordinates.

In general, an object gets strained, if there are internal forces changing the equilibrium positions of the atoms. The significant quantity is the stress tensor $\boldsymbol{\sigma}$ which describes the internal forces per area. For continuous elastic materials, the stress and strain tensor are connected via Hooke's law

$$\boldsymbol{\sigma} = \boldsymbol{E}\boldsymbol{\eta}, \tag{17}$$

where E is the so called elasticity tensor. This fourth order tensor is a material property. It can be shown, that in an isotropic material equation 17 can be written as:

$$\sigma_{ij} = \lambda\eta_{kk}\delta_{ij} + 2\mu\eta_{ij} \tag{18}$$

using the Einstein summation notation. λ and μ are the Lamé constants and δ_{ij} is the Kronecker delta.

So far, this equation only covers mechanical strain. But strain can also occur for other reasons, for instance volume expansion upon heating. This is taken into account by introducing an additional stress term $\boldsymbol{\sigma}_{\mathrm{nm}}$ including the non-mechanical effects:

$$\boldsymbol{\sigma} = \boldsymbol{E}\boldsymbol{\eta} + \boldsymbol{\sigma}_{\mathrm{nm}}. \tag{19}$$

This work focuses on one dimensional problems. By convention, this dimension is the z-direction. In this case, equations 16, 17 and 19 can be further simplified and yield:

$$\begin{aligned} \sigma_{zz} &= 3\frac{1-\nu}{1+\nu}B\eta_{zz} - 3B\beta\Delta T(z), \\ \eta_{zz} &= \frac{\partial u_{zz}}{\partial z}. \end{aligned} \tag{20}$$

In this equations, ν is the Poisson's ratio, B is the bulk modulus, β is the linear thermal expansion coefficient and $\Delta T(z)$ is the temperature change at position z.

A deformation is a perturbation of the equilibrium state of an object. As such, it propagates through the solid. Applying momentum conservation yields the displacement equation of motion:

$$\rho_0\frac{\partial^2 u_m}{\partial t^2} = (\lambda+\mu)\frac{\partial^2 u_k}{\partial x_k \partial x_m} + \mu\frac{\partial^2 u_m}{\partial x_k \partial x_k} \tag{21}$$

with the unperturbed mass density ρ_0. This is also known as the Navier-Cauchy equation. In combination with equations 16 and 18 and reduced to one dimension, this gives

$$\frac{\partial^2 u}{\partial t^2} - c^2\frac{\partial^2 u}{\partial z^2} = \frac{1}{\rho_0}\frac{\partial \sigma}{\partial z}, \tag{22}$$

the one dimensional wave equation for the displacement, where c is the sound velocity. The left hand side of this equation is a homogeneous wave equation. The right hand side is the source term and identifies the gradient of stress as the source for displacement waves.

A similar wave equation can be obtained for the strain by taking the spatial derivative according to equation 20:

$$\frac{\partial^2 \eta}{\partial t^2} - c^2 \frac{\partial^2 \eta}{\partial z^2} = \frac{1}{\rho_0} \frac{\partial^2 \sigma}{\partial z^2}. \tag{23}$$

By combination of equations 20 and 23 together with boundary conditions at surfaces and interfaces, the strain evolution inside solids following the creation of stress can be calculated. In general, an analytical solution is impossible and numerical methods are required. However, for certain situations analytical solutions can be found.

A special case of wave propagation is the transition into another material. Whenever an acoustic wave hits the interface between two different materials, it will be partly transmitted and partly reflected. It is helpful to define the acoustic impedance $Z = \rho c$ of an acoustic medium. With that, the transmission[1] and reflection coefficients for a strain wave traveling across an interface from medium 1 to medium 2 are:

$$\begin{aligned} R &= \frac{Z_2 - Z_1}{Z_1 + Z_2}, \\ \tilde{T} &= \frac{c_1}{c_2} \frac{2Z_1}{Z_1 + Z_2}. \end{aligned} \tag{24}$$

In the special case of the reflection at a free surface, the transmission is zero and the reflection coefficient gets $R = -1$, meaning that the strain changes its sign upon reflection at a free surface.

4.3.2 Coherent Acoustic Phonons

Going from the continuous elastic model to a microscopic picture of the solid gives a complementary view of acoustic waves. If one looks onto the motion of the atoms forming the object, their movement is normally described in terms of phonons. Phonons are collective movements of the lattice atoms.

They have a wavelength λ and an oscillation frequency f. It is often more convenient to talk about the wave vector $q = \frac{2\pi}{\lambda}$ and the angular frequency $\omega = 2\pi f$. The two quantities are connected via the dispersion relation $\omega = \omega(q)$. For acoustic phonons close to the center of the Brillouin zone, which are the relevant ones for describing acoustic waves, the dispersion relation is:

$$\omega = cq, \tag{25}$$

with the sound velocity c as the proportionality constant.

In that sense, acoustic waves can be described as a coherent superposition of acoustic phonons. Therefore, they are often referred to as coherent acoustic phonons.

4.3.3 X-Ray Diffraction from Acoustic Waves

The phonon picture of picosecond acoustic waves yields an intuitive way of understanding the diffraction of X-rays at transiently strained crystals. The Laue equation 5 can easily be expanded to introduce phonons. Instead of scattering with a reciprocal lattice vector only, the incoming wave additionally scatters with a phonon of wave vector $\vec{q}$. Therefore, the phonon momentum has to be included in the momentum balance:

$$\vec{k} - \vec{k}' = \vec{G} \pm \vec{q} \tag{26}$$

---

[1] The transmission coefficient is usually named T in the literature. Since T is used for the time in this work, it is named $\tilde{T}$ instead.

This can be depicted graphically in reciprocal space as shown in figure 4. The incoming and outgoing wave vectors now have to match the reciprocal lattice vector plus the phonon wave vector. This gives rise to additional intensity components apart from the actual Bragg peak.

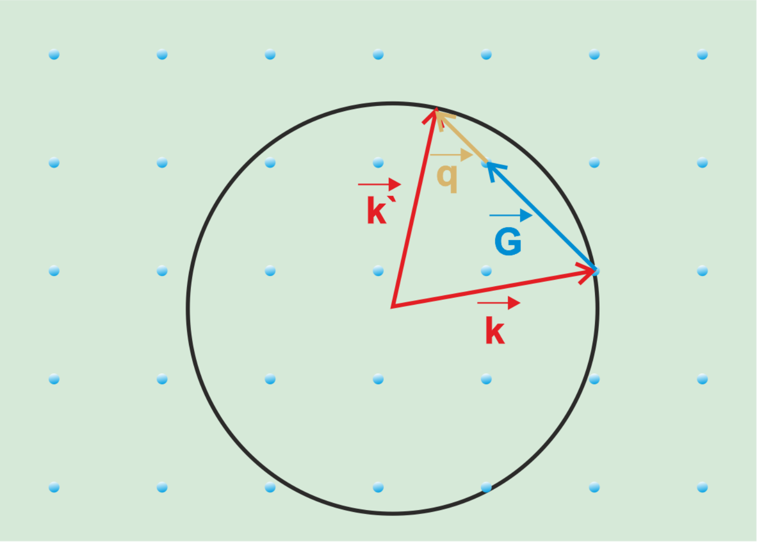

Figure 4: **Scattering with phonons in reciprocal space.** If scattering with phonons is taken into account, the two reciprocal lattice points on the Ewald sphere are connected by the sum of the phonon wave vector and a reciprocal lattice vector.

The relation between the deviation of the diffraction angle from the Bragg angle and the phonon wave vector can be derived with the help of figure 5 comparing the reflection at a reciprocal lattice vector with the situation involving a phonon. Geometrical arguments yield:

$$\begin{aligned} \sin(\theta_B) &= \frac{G}{2k}, \\ \sin(\theta_B + \Delta\theta) &= \frac{G+q}{2k}. \end{aligned} \tag{27}$$

The combination of these equations and performing a Taylor expansion of the trigonometrical function gives:

$$q = \frac{4\pi}{\lambda}\cos(\theta_B)\Delta\theta. \tag{28}$$

In the following, the qualitative impact of the presence of coherent acoustic phonons on X-ray diffraction patterns is shortly discussed. A pure phonon is an infinite sinusoidal dislocation of the atoms in a sample. In this work, we study coherent acoustic phonons in substrate materials, which have a surface coated with a metal. The closest approximation to a pure phonon in this system is a half-infinite sinusoidal strain distribution. Such kinds of acoustic waves have been created by multi-pulse excitation schemes and are discussed in the literature [44].

Figure 6 a) shows such a monochromatic phonon with a wavelength of 100 nm for three different times after an arbitrary time zero. A simulation of the transient diffraction pattern for a GaAs (400) sample with such a strain wave in it is shown in part b). According to equation 28, an oscillation in the diffraction intensity occurs at angles of ± 0.34° additional to the unaffected main peak. This is even clearer in part c), where the upper graph shows the rocking curves for the three snapshots depicted in a) and the

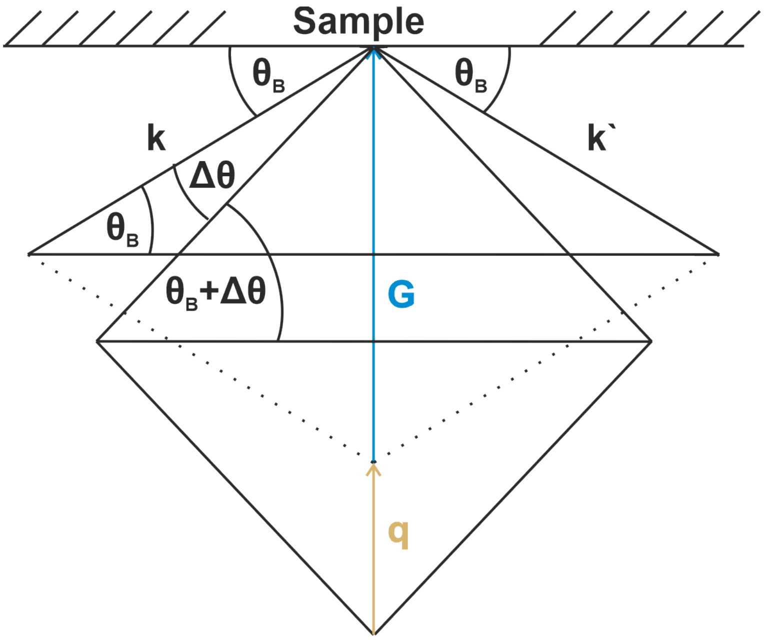

Figure 5: **Derivation of the connection between phonon wave vector and diffraction angle.** The relation between an angular deviation $\Delta\theta$ and the corresponding scattering phonon's wave vector can be derived from geometrical considerations for the experimental configuration.

bottom graph shows the transient intensity oscillation at the angular position marked by the black line in the upper graph.

Hence, X-ray diffraction at acoustic phonons can be interpreted as inelastic scattering with the respective phonon mode[2]. For each wave vector, the diffraction intensity is modulated at an angle connected to q via equation 28. As can be seen in part c) of figure 6, the response in the diffraction pattern is not a δ-function at the specific angle, as one would expect for a pure phonon. This has different reasons. First, the oscillation is located in a half-space in contrast to a pure phonon.

Second, X-rays have a finite penetration depth. In the vicinity of the Bragg peak, this is mainly caused by extinction, while absorption is the dominant effect further apart. The finite penetration depth of the X-rays further restricts the extent of the probed region and, therefore, of the probed oscillation leading to a broadening.

The diffraction patterns change drastically, if instead of an infinite oscillation a strain wave only consisting of one cycle of the sine is traveling into the substrate. Mathematically, this corresponds to multiplying the sine with a gate function which has a value 1 for the cycle and 0 elsewhere. Therefore, the pulse is not monochromatic anymore, but the amplitude is distributed over a an extended range of phonon wave vectors. This can be seen in graph e). In contrast to b), oscillations occur at all angles in the transient rocking curves. This is also obvious in the single rocking curves of graph f). The oscillation frequency is related to the corresponding wave vector via the sound velocity of GaAs $c^{(100)} = 4.73\,\frac{\mathrm{nm}}{\mathrm{ps}}$ and yields an increasing frequency at higher angles.

If one compares the intensity at the fixed angle in the lower part, two differences to graph c) are visible. First, the intensity oscillation does not appear instantaneously, but it builds up within the first tens of picoseconds. The reason is, that the acoustic wave just starts to enter the sample at time zero and has fully entered only after 47 ps. Second, the oscillation is damped after reaching a maximum amplitude. Since the acoustic wave

---

[2] Since the energy of the X-ray photons is much higher than that of the phonons, the energy transfer is negligible in this case. The important aspect is the transfer of momentum.

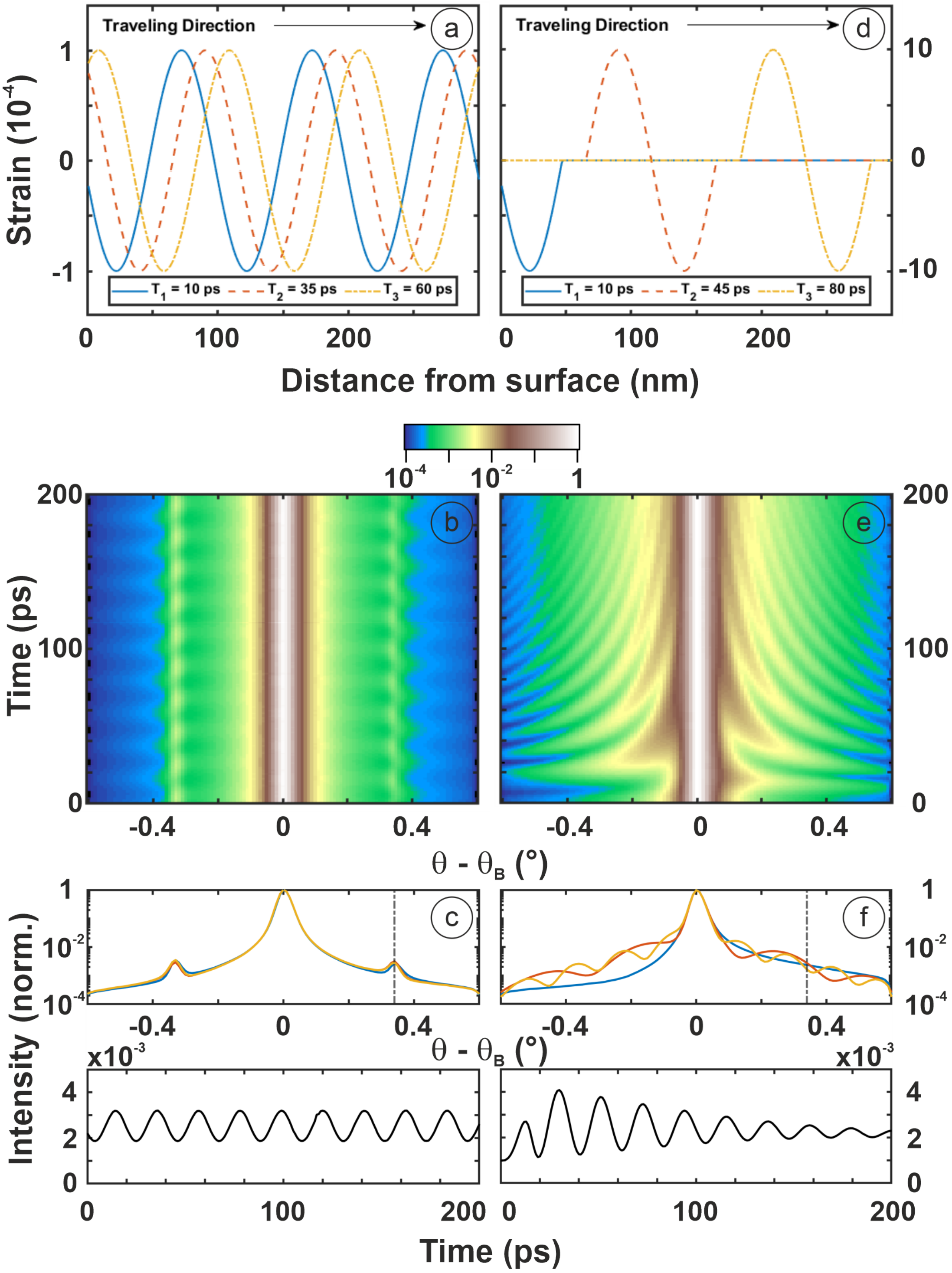

Figure 6: **Influence of pure phonons and gated phonon pulses on transient diffraction patterns.** The left hand side shows the influence of a "pure" phonon mode on the time resolved diffraction pattern of the (400) GaAs Bragg peak. The strain profile of the mode is shown for several points in time in a). b) shows the calculated diffraction pattern in 2D false color representation. c) depicts rocking curves for particular time points and the time dependent diffraction intensity at the angular position, where the signal of the phonon mode occurs (black line). The right hand side graphs show the same for a single cycle of the same sine. The strain enters the system at $T = 0$.

travels deeper into the substrate with time, the X-ray intensity is reduced by absorption and extinction before getting diffracted at the strained part. Therefore, the diffracted signal is reduced accordingly.

In general, any acoustic pulse after laser excitation is a superposition of a spectrum of different phonon modes. Their relative strength defines the shape of the acoustic pulse as well as the X-ray diffraction response. It is therefore possible to learn something about the acoustic behavior of the system and the microscopic processes after optical excitation by analyzing the transient X-ray diffraction intensity.

4.4 Deep Neural Networks (DNN)

This section introduces the concept of deep neural networks, which are used in chapter 7 to directly retrieve the strain distribution induced by optical excitation from transient diffraction patterns. It is structured as follows: First, the general concept of deep neural networks and the training of such networks are discussed. Second, a more detailed discussion of the specific network architecture used in this work, the convolutional neural network, is given.

4.4.1 General Aspects

Deep neural networks are a subclass of artificial neural networks (ANN). ANNs are computational models consisting of layers of neurons. Neurons are building blocks, which can receive, process and pass data on to the next layer. The output of a neuron is called an activation and is delivered to the next neurons via connections named synapses. Every synapse has a weight and a bias determining, how strongly the upcoming neurons input is influenced by a specific previous neuron [34]. It should be noted, that the terminology is based on the human brain, even though it is known today, that the function of the real brain is more complex than the architectures described here.

Each ANN consists of an input layer, an output layer and hidden layers in between. Accordingly, the contained neurons are called input, output and hidden neurons. The first one receive data, e.g. images, from the outside world. The second one present a result, e.g. the classification probabilities for the object in the image, and the hidden layers process the information (compare figure 7). An artificial neural network is called a deep neural network, when it consists of many hidden layers. In general, the deeper a layer is located inside the network, the more abstract the features it processes are. However, there is no strict border for a network being called deep.

Deep neural networks are a method of machine learning. By training the network with pairs of input data and corresponding output data, one can adjust the internal parameters in such a way that the network learns to analyze unknown data. This approach is known as supervised learning. Since the features of the input data used for the prediction of the output data are not predetermined, the system has to define them on its own, which is called representation learning.

The first ideas for the use of neural networks have been proposed as early as 1958, when Frank Rosenblatt published the idea of a Perceptron, the first shallow neural network as a model of information processing in the brain [101]. However, for the efficient use of deep neural networks, three requirements have to be fulfilled:

1. An efficient method for adjusting the network parameters,
2. the computational power to train the network in a feasible time,
3. a sufficient amount of training data.

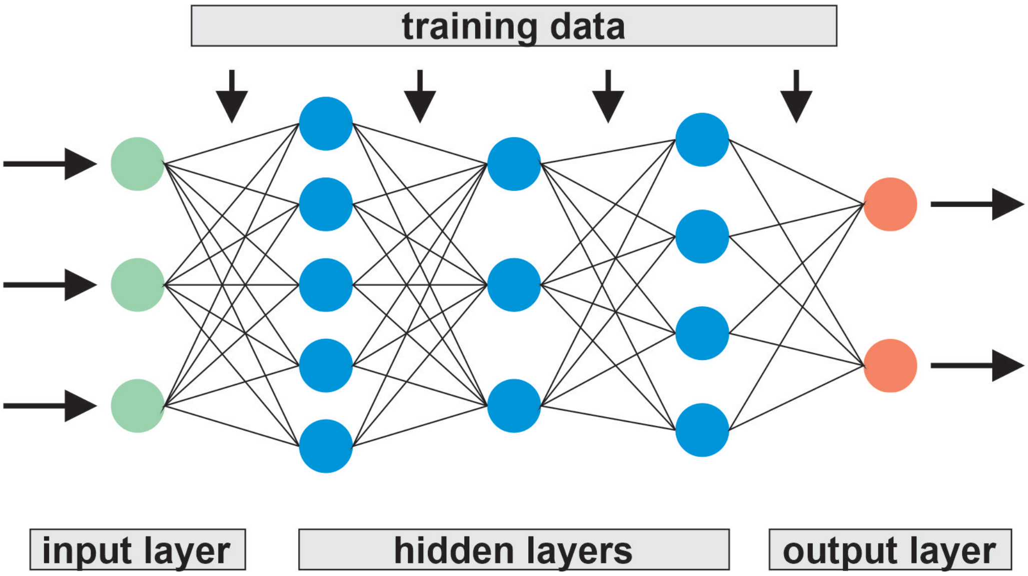

Figure 7: **Basic concept of an artificial neural network.** The colored circles represent neurons, which are connected by synapses indicated by black lines. Each synapse carries a weight and a bias. The network consists of an input and output layer together with three hidden layers. Training data is used to adjust the parameters of the network. The number of neurons in each layer is part of the network architecture.

Number 1. and 2. are solved problems: The backpropagation algorithm [85, 105] together with a suitable parameters update rule discussed in the next chapter and the adaption of graphic processing units (GPU) allow for efficient training of networks with billions of parameters on personal computers. Bullet point 3. has to be tackled for every single application individually.

4.4.2 Training Neural Networks

To train a neural network means updating the free parameters such that the output of the network for a given input comes closer to the 'real' output. The training is steered by so called hyperparameters, which are fixed prior to the training in contrast to the continuously adapted parameters.

Imagine, having a set of training data pairs consisting of inputs x_i together with correct outputs $y(x_i)$. To quantify the performance of the network, some kind of error has to be defined. A commonly used error metric, which is also used in this work, is the mean squared error (MSE) defined as:

$$E(p) = \frac{1}{N}\sum_{i=1}^{N}(y(x_i) - a_i(p))^2, \tag{29}$$

where E is the error of the network, p is the vector of network parameters, N is the size of the training data set and a_i is the output vector of the network for the input x_i. For the ideal case of $a_i(p) = y(x_i)$ the error vanishes. Therefore, the problem reduces to the minimization of the error function with respect to the network parameters p.

A simple approach to this problem is the gradient descent algorithm [99]. Let p_l be the parameter vector of the l-th training iteration. The parameters are then optimized by moving a small step into the opposite direction of the gradient of the error. Since the gradient points in the direction of the steepest increase of a function, the opposite direction decreases the value of the objective function. The $(l+1)$-th parameter vector is therefore given by:

$$p_{l+1} = p_l - \alpha \nabla E(p_l). \tag{30}$$

The parameter α is called the initial learning rate and is a hyperparameter of the network training. It can be optimized to increase the network performance. The principle of gradient descent is shown for a simple example in figure 8.

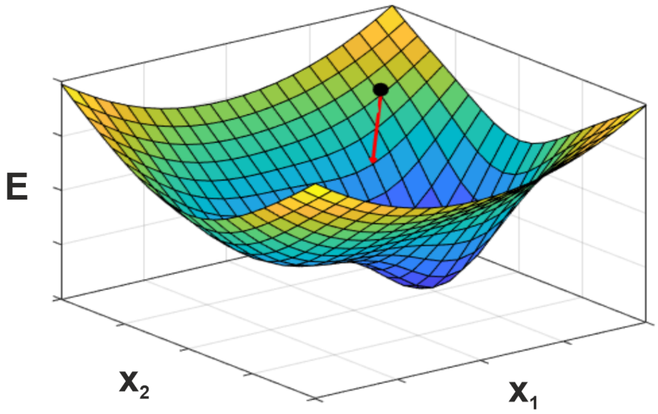

Figure 8: **Optimization in a 2D parameter landscape.** The graph shows an arbitrary error function landscape with two independent parameters x_1 and x_2. At each point in the parameters space, the error function has a specific value (black dot) and the negative gradient shows in the direction of the steepest descent (red arrow). Following this direction, the minimum value of the error function can be found. However, there is no guarantee that the global minimum can be found efficiently and that the optimization does not get stuck in the saddle point on the left hand side of the visualization.

In practice, training data sets can become very large and the calculation of equation 29 for large N can make the network training inefficiently slow. To overcome this problem a small mini-batch of the data is used for each training iteration instead of calculating the error function for the whole data set. This is called stochastic gradient descent and can be interpreted as a noisy approximation to the full batch gradient descent.

Even though stochastic gradient descent can be useful for specific cases, it has some issues. Firstly, it can be inefficient, when partial derivatives of the error function with respect to one parameter are much smaller than to another parameter. In that case the parameter vector oscillates around the parameter with the steepest descent and the optimization needs much longer to converge. Secondly, the optimization gets stuck in saddle points and thirdly it can by no means overcome a local minimum. Lastly, it suffers strongly from noise due to the stochastic character of the method.

There are several more advanced optimization techniques used for the training of neural networks such as stochastic gradient descent with momentum (sgdm) [79] or the adam optimizer (adaptive moment estimation) [54], which overcome these problems. The latter one will be used in this work and is therefore shortly discussed in the following.

When the adam optimizer is applied, the discussed issues are solved by adjusting the update rule of stochastic gradient descent with the first two moments of the gradient (average and uncentered variance):

$$\begin{aligned} m_l &= \beta_1 m_{l-1} + (1-\beta_1)\nabla E(p_l), \\ v_l &= \beta_2 v_{l-1} + (1-\beta_2)[\nabla E(p_1)]^2. \end{aligned} \tag{31}$$

where β_i are the gradient decay rates, which are also hyperparameters of the network training[3].

A network parameter is then updated as following:

$$p_{l+1} = p_l - \frac{\alpha m_l}{\sqrt{v_l} + \epsilon}. \tag{32}$$

Equations 31 describe a moving average of the gradient over the iterations. The first equation can be interpreted as the equivalent of a velocity in a parameter landscape. It helps to overcome saddle points or local minima and reduces the influence of noise on the error optimization, because the movement through the parameter space 'remembers' the previous movement. In a 2D-parameter space, this is analog to the trajectory of a particle in a hilly 2D-landscape.

The second momentum is placed in the denominator of the update rule and ensures that the learning rate is effectively decreased for large gradients and increased for small gradients. This damps out oscillations and increases efficiency. ϵ is a small number, normally chosen around $10^{-7} - 10^{-8}$ and is introduced to prevent division by 0.

It should be noted that the described optimization procedures do not necessarily converge to global minima. They can also get stuck in local minima. This problem can be overcome by repeating the optimization with different starting points and comparing the results.

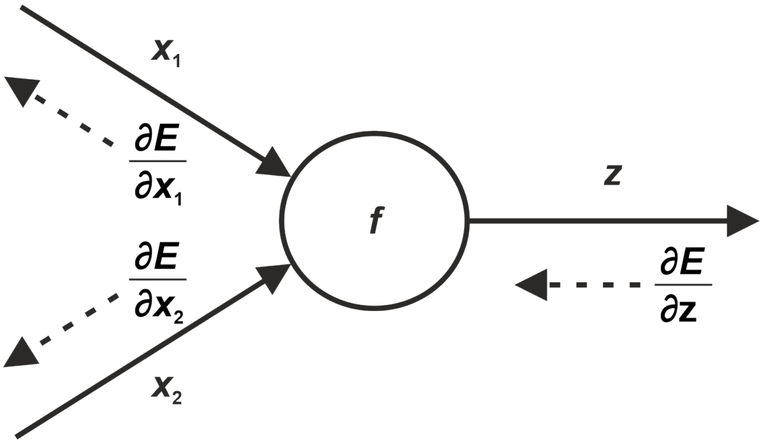

Figure 9: **Principle of Backpropagation.** The gradient of the error function with respect to a parameter x_i of the network can be calculated by backpropagating the gradients through the network using the chain rule.

The only problem left is how to efficiently calculate the gradient of the error function with respect to the adjustable parameters of the network, namely the partial derivatives. This challenge was solved by the introduction of the backpropagation algorithm [105]. The general idea is to backpropagate the gradient through the network by inverse application of the chain rule. Let f be a neuron performing some kind of calculation. It has two inputs x_1 and x_2 and an output z. This is depicted in figure 9. Suppose that the gradient of the

---

[3] In fact, there is an additional transformation $\hat{m}_l = m_l/(1-\beta_1^l)$ and $\hat{v}_l = v_l/(1-\beta_2^l)$ to account for an initialization bias, which is not really relevant for the understanding of the mechanism and is therefore not discussed in detail, here. For further information see [54].

error function E with respect to the output variable $\frac{\partial E}{\partial z}$ is known and we are interested in the gradient regarding the input variables. According to the chain rule, this is given by:

$$\begin{aligned}\frac{\partial E}{\partial x_i} &= \frac{\partial E}{\partial z}\frac{\partial z}{\partial x_i} \\ &= \frac{\partial E}{\partial z}\frac{\partial f(x_i)}{\partial x_i}.\end{aligned} \tag{33}$$

The error can therefore be propagated back through the network, presuming, that the gradients of the single computations of the network with respect to the inputs $\frac{\partial f(x_i)}{\partial x_i}$ are known, which is legitimate for common deep learning architectures. Equation 33 together with a suitable optimization algorithm as described in equations 31 and 32 allows for efficient training of a deep neural network.

Finally, this leads to the following training scheme for a DNN:

1. Sample a mini-batch,
2. forward it through the network and calculate the error,
3. backpropagate the gradient,
4. update the network parameters.

In the end, the network should not only learn to analyze the training data, but to work on unknown data sets. To check for that during the training process, a part of the training data is randomly chosen and separated as a validation set. After a certain number of training iterations, the network is evaluated on the validation data. This training scheme is repeated until the validation error does not decrease anymore or reaches a sufficiently low value.

4.4.3 Convolutional Neural Networks (CNN)

Convolutional neural networks are the most successful method for image classification [59, 126, 43] and other visual analysis tasks such as image tagging [52] or image segmentation [139]. Many convolutional neural networks consist of five types of layers. Figure 10 shows a typical succession of the first three layer types.

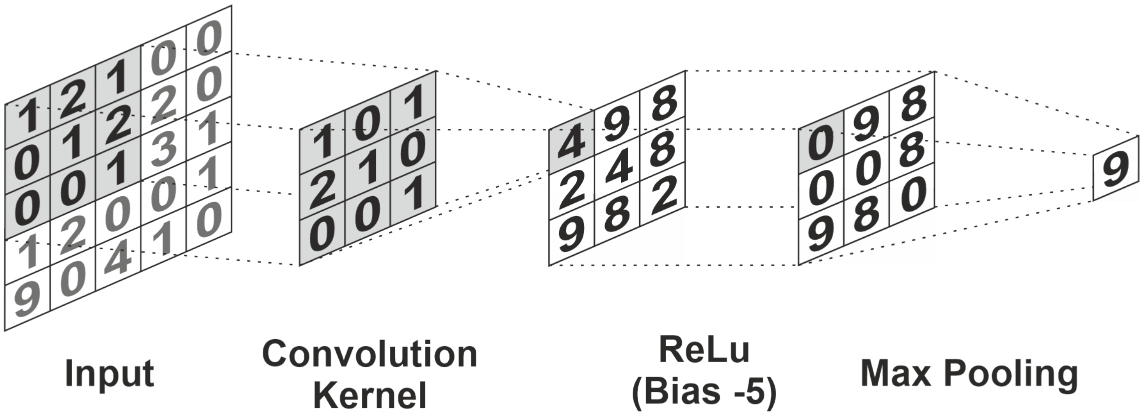

Figure 10: **Operating principles of the basic CNN building blocks.** The figure shows an exemplary processing of a 5x5 input matrix by sequence of a convolutional, a ReLu and a max pooling layer. The output of the sequence would be a scalar with value 9 in this case.

Convolutional Layer Convolutional layers are the main building blocks and the namesake of this architecture. They consist of filter kernels which are moved across the discretized 2D input data horizontally and vertically. At each position, the dot product between the input and the kernel is calculated. Mathematically, this is equivalent to taking the convolution between the input and the kernel. The values of the kernel are trainable parameters of the network.

A convolutional layer preserves the spatial connectivity of adjacent image points (pixels) and is therefore capable of identifying local structures in the input data. Due to that, CNNs are superior to other network architectures in image analysis. Thus, the kernels of the network are feature maps scanning for typical shapes in the input data allowing for pattern recognition.

ReLu Layer Relu is the abbreviation for rectified linear unit. A ReLu layer is an activation function, which is defined by [59]:

$$f(x) = \max(0, x). \tag{34}$$

It is shown in figure 11.

The idea of an activation function is that it only forwards inputs that surpass a certain threshold. This is inspired by neurons in our brain, which only fire, if the applied potential exceeds a limit value. For shifting the threshold away from 0, a bias is introduced as an additional training parameter of the network.

An activation function introduces nonlinearity to a deep neural network. Nonlinearity is necessary, because otherwise a fully linear deep neural network could be replaced by a single linear function with suitable parameters. In that case, one would lose all the advantages of deep neural networks learning to analyze more and more abstract features in the hidden layers. There are lots of other possible activation functions such as hyperbolic tangent or the sigmoid function [64]. However, ReLu has shown to produce good results [36] by simultaneously being effective to train and is therefore used in the architectures of this work.

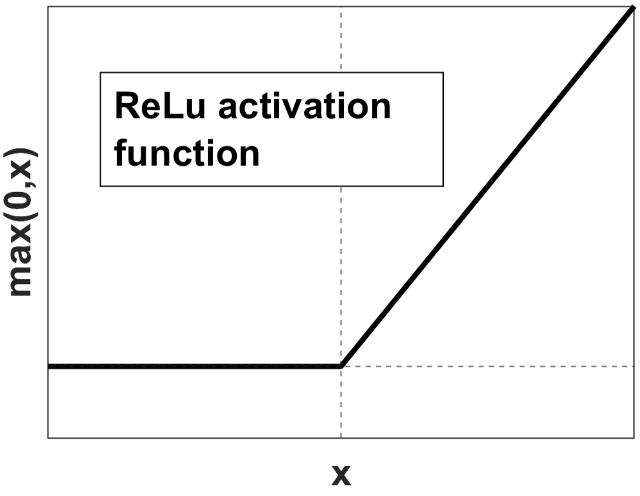

Figure 11: **ReLu activation function.** The ReLu activation function is 0 for $x \leq 0$ and x elsewhere.

Pooling Layer Pooling is a method of down sampling the data. A regularly employed method is average pooling, where the input is divided into rectangles and the average value of a rectangle is passed to the next layer [43]. Another important method is max pooling, where only the highest value of a rectangle is passed [111].

The underlying concept behind pooling is that not the exact position of a detected feature is important but its relation to other features. This comes with several advantages. Pooling reduces the size of the input and therefore the number of parameters of the network. This often results in faster training. At the same time it prevents overfitting, meaning that the network learns to analyze the training data too good and subsequently fails to generalize.

Batch Normalization Layer Batch normalization layers are introduced to increase the stability and speed of deep neural networks. For that purpose, the input to the layer is re-centered and re-scaled. All output of the neurons throughout the entire mini-batch are normalized to have the same mean and variance. Even though, batch normalization is widely used and has proven to be very effective in improving the performance of deep neural networks, it is still an open debate, what the actual reason for this is [109].

Fully Connected Layer The fully connected layer is normally the last layer of a deep neural network. As the name states, all neurons of this layer are connected to all neurons of the previous layer, which are typically the outputs of the whole network. A fully connected layer at the end ensures, that all outputs can be affected by every part of the previous analysis.

All in all, a general convolutional neural network is build up of sequences of convolutional layers, ReLu layers, pooling layers and batch normalization layers closed by a fully connected layer.

4.4.4 Residual Neural Networks

When going to deeper networks, it turns out that the training with current algorithms is not effective anymore and that deeper networks even get outperformed by shallower networks [42, 123], which is called the degradation problem. This is not based on a principle disadvantage of deeper networks. Imagine having a shallow network, where a few layers are added. We assume that by a suitable choice of the parameters, each layer can approximate any nonlinear function. Thus, the parameters can also be adjusted such, that the additionally added layers are equal to the identity. By doing so, the deeper network should at least reach the performance of the shallower network. This leads to the conclusion, that the problem is not the structure of the network, but the commonly applied training procedures.

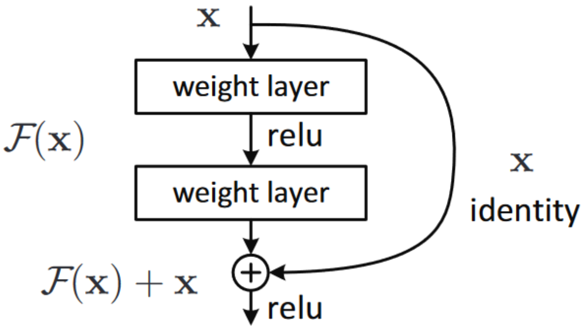

Figure 12: **Residual neural networks.** Residual layers shortcut the training problem in deeper neural networks by passing an identity parallel to the layers of the network (taken from [43] © [2016] IEEE).

A very successful proposal for overcoming this problem is the use of residual neural networks. The idea is to introduce shortcuts as shown in figure 12. In the case described above, the network could easily reach the performance of the shallower network by adjusting the parameters of the layer sequence such that $\mathcal{F}(x) = 0$. It has turned out, that residual neural networks allow for the efficient training of deeper neural networks reaching better results in a shorter training time, while having less parameters than comparable deep networks without residual building blocks [43].

The described network architecture of residual convolutional neural networks has proven to be very successful in solving image analysis tasks. In chapter 7, it will be described how this architecture can be adapted to the problem of strain retrieval from transient diffraction patterns.

5 Experiments

5.1 Setup

The time resolved X-ray diffraction experiments of this work were performed at the modular laser-plasma based X-ray source at the University of Duisburg-Essen. The following section gives an overview about the details of the setup, the investigated samples, the experimental routines and the subsequent data analysis. The general working principle of the source has been described in chapter 4.2. Further details can be found in the work of Afshari et al. [1, 2].

5.1.1 Laser System

The modular X-ray diffraction setup is "driven" by a self-built 10 Hz TW fs laser system. The basis is a Ti:Sa oscillator (see chapter 4.2) generating 5 nJ pulses with a duration of 30 fs full width half maximum (FWHM) at 80 MHz repetition rate centered around 782 nm. The pulses are stretched to 200 ps to be further amplified based on the chirped-pulse amplification (CPA) principle [124].

Amplification is done within two stages: An 8-pass pre-amplifier, pumped by a frequency doubled Nd:YAG laser with a maximum energy of 80 mJ per pulse increases the pulse energy to 0.6 mJ. Prior to that, a pockels cell picks pulses with 10 Hz repetition rate out of the pulse train delivered by the oscillator. In a second amplification stage, a booster amplifier with 4 passes increases the pulse energy up to the optimal working point of 200 mJ. The Ti:Sa crystal of this amplification stage is cooled down to $-170\,^{\circ}\mathrm{C}$ in a vacuum of 5×10^{-7} mbar, which significantly increases the thermal conductivity and thus strongly reduces thermal lensing and avoids damage due to thermal load. The crystal is pumped from both sides with frequency doubled Nd:YAG lasers of 450 mJ pulse energy to ensure homogeneous excitation conditions inside the crystal.

Before recompression, the beam diameter is increased to 25 mm to avoid non-linear effects in air. These would occur due to the high intensities, if the pulse is compressed in time and space simultaneously. At a last step, the pulse is temporally recompressed in a grating compressor. The output pulses have a duration[4] of approximately 100 fs at an energy of 120 mJ. The contrast ratio, which is defined as the ratio of the maximum intensity to the intensity 2 ps before the maximum, is 10^7.

There are three important parameters for the efficiency of the X-ray production:

- Pulse duration
- Intensity
- Contrast ratio

The pulse duration limits the achievable X-ray pulse duration. At the same time, it is one parameter determining the intensity. High peak intensities are only accessible with short pulses.

The intensity is important for the X-ray production process. A sufficient yield of the characteristic X-ray radiation can only be reached, if a surface plasma is created and if this plasma contains enough hot electrons with an energy above the impact ionization threshold. As discussed in chapter 4.2, this is optimal at intensities in the order of $10^{16} - 10^{18}\ \frac{\mathrm{W}}{\mathrm{cm}^2}$, but this depends on the target material.

A high contrast ratio is important for the characteristics of the surface plasma and thus for the X-ray yield. Intensity peaks, which arrive prior to the main pulse, can already

---

[4] The oscillator actually delivers shorter pulses, but the system is not operated at maximum compression.

ignite the plasma. When the main pulse finally arrives, the plasma scale length might be larger than the optimum scale length for X-ray emission.

5.1.2 X-Ray Setup

The thus compressed pulse is used for pump-probe experiments in the X-ray setup. A sketch of the X-ray setup is shown in figure 13. It consists of the optical pump path and the X-ray probe part. Before these two are separated, the center part of the the beam is cut out by a holey mirror (M1). This beam part is called the pre-pulse and contains around 3 % of the total energy. It is passed over a delay stage (D1) before it gets spatially recombined with the main pulse through another holey mirror (M2) allowing for a variable time delay between the two pulses. The delay stage is adjusted such that the pre-pulse arrives a few ps before the main pulse. The role of the pre-pulse is to ignite the plasma before the main pulse arrives, giving it the time to evolve to an optimal plasma scale length. For the given conditions, a time delay of 2 ps has proven to give the maximum K_α yield [2].

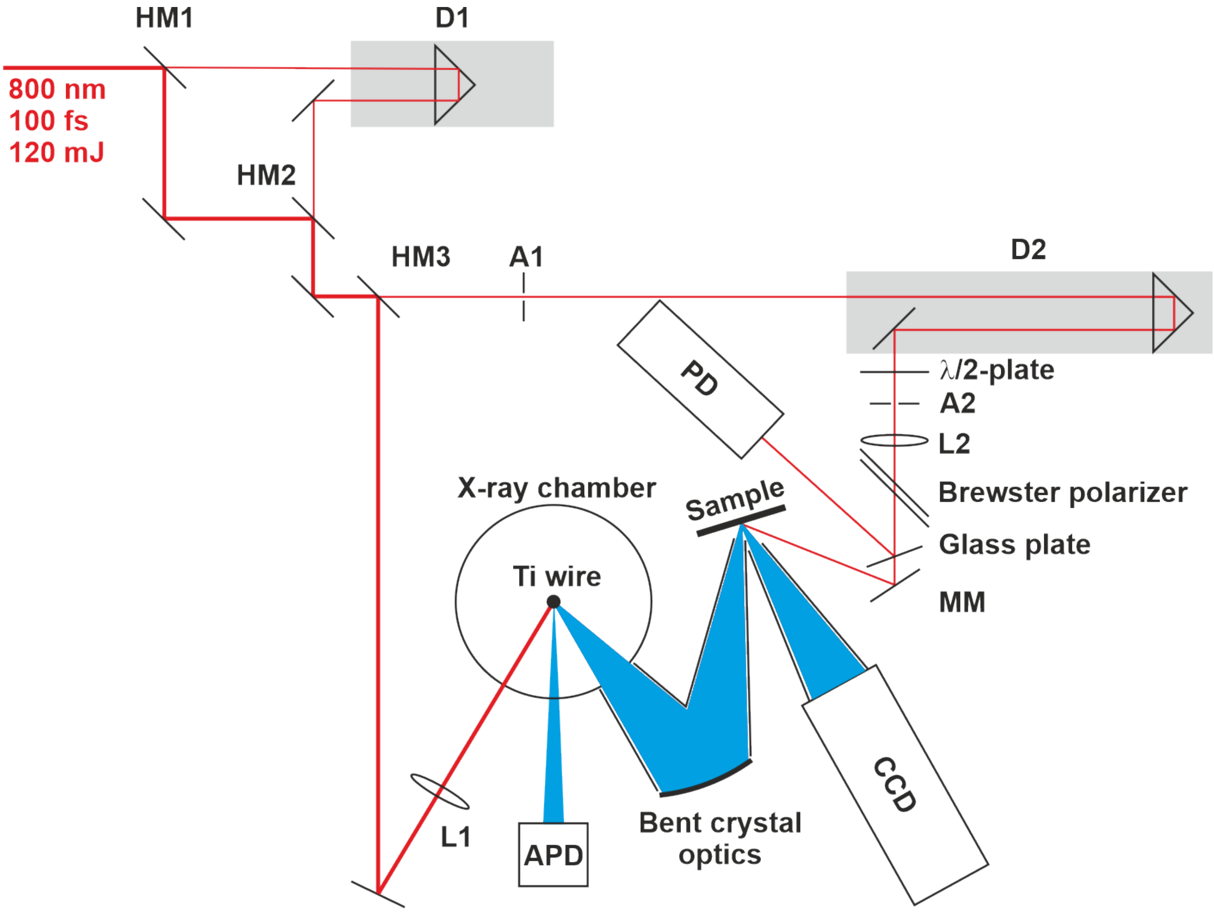

Figure 13: **X-ray setup.** This figure shows the paths of the beams in the X-ray setup. Holey mirrors (HM1 – HM3) divide the beam, delay stages (D1 & D2) allow to impose delays between the different parts, apertures (A1 & A2) shape the pulse, lenses (L2 & L2) focus it and a motorized mirror (MM) is used to create spatial overlap of pump and probe. The diffraction images are taken with a CCD-camera, an avalanche photodiode (APD) and a photo diode (PD) ensure constant experimental conditions.

Optical Part By another holey mirror (M3), a part from the side of the beam is separated to serve as the pump. A second delay stage (D2) imposes the possibility to vary the time delay Δt between the pump and probe beam. A $\lambda/2$-plate together with a dielectric Brewster polarizer allows for adjusting the pump pulse energy. Due to the operation principle of the polarizer, the pump is s-polarized. The beam is focused onto the sample by a $f = 95\,\mathrm{cm}$ lens (L2) down to a size of 560 µm (FWHM). It hits the sample under an angle of incidence of 36°.

Behind the Brewster polarizer, a small portion of the beam energy is reflected at a one-side anti-reflection coated glass plate. This part is sent to a photo diode, which monitors the beam energy on a pulse-to-pulse basis. Monitoring the pulse energy allows for the correction of mid to long term instabilities of the laser energy and small pointing instabilities. Two apertures (A1 & A2) in the beam path act as spatial filters and ensure that the focused pump beam is Gaussian to a good approximation at the position of the sample.

X-Ray Part The main part of the beam is reflected by the third holey mirror (M3) and is focused into the X-ray chamber by a $f = 30\,\mathrm{cm}$ lens (L1). The X-ray generation has to be done in vacuum, because otherwise nonlinear interactions of the focused laser beam with the surrounding air would disturb it [143]. A moving titanium wire serves as the solid target. A motor placed outside the chamber pulls the wire through special teflon gaskets to provide a fresh surface for every shot. This is necessary, because irradiation of the wire with only two pulses at the same position already breaks it.

X-rays are emitted into the whole solid angle as described in chapter 4.2. The spectrum of the source can be seen in figure 14. It contains Bremsstrahlung as well as characteristic radiation.

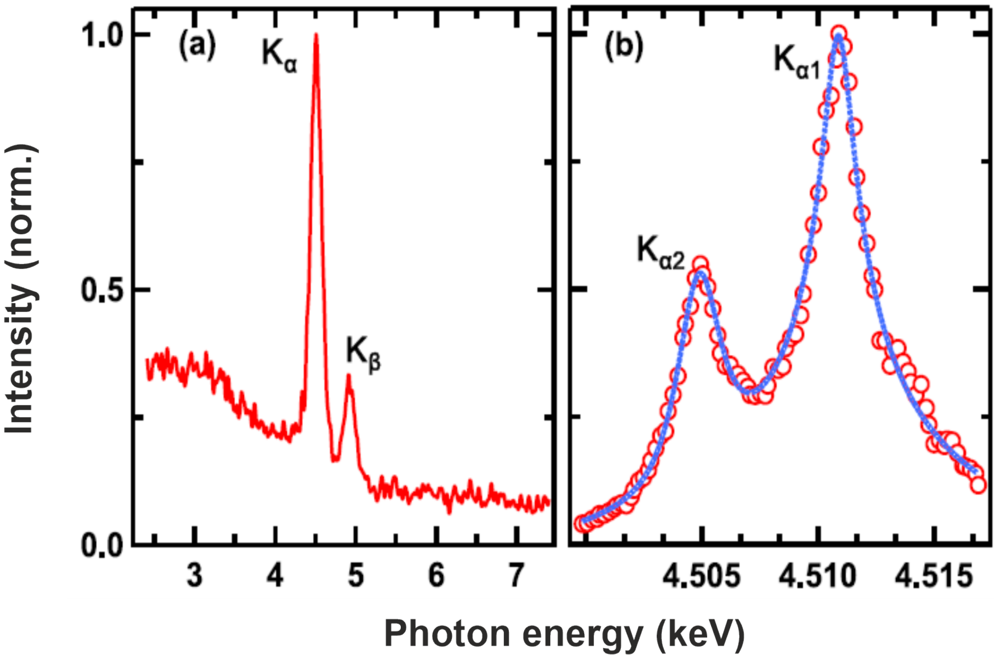

Figure 14: **Spectrum of the emitted X-rays.** The spectrum of the emitted X-rays [2] consists of two components: A background of Bremsstrahlung and discrete peaks of characteristic lines (shown in (a)). The energy of the characteristic lines is typical for the element emitting the X-rays; in this case titanium. The K_α-line is separated into two peaks due to spin orbit coupling (shown in (b)). The blue line is a guide to the eye. The bent crystal optics of the setup isolates the $K_{\alpha 1}$-line at an energy of 4.511 keV and diffracts it onto the sample.

The X-rays leave the chamber through two Kapton foil covered windows. Behind the first one, a toroidally bent Ge crystal collects X-ray photons and focuses them onto the sample [8, 81, 82]. The crystal is bent such that the Bragg condition of the Ge (400) Bragg reflection is fulfilled at every point of the surface. A 1:1 imaging of the source onto the sample is achieved by putting the source, the crystal and the sample in the so called Rowland-circle geometry as is depicted in figure 15 [78, 82]. The X-ray spot size is approximately 80 µm on the sample, which is much smaller than the pump spot size. This ensures, that the probed region is homogeneously pumped.

The bent crystal optics has a second important function: It monochromatizes the emitted X-rays. This is necessary in order to achieve high angular resolution. Since the working principle of the bent crystal optics is Bragg diffraction, only photons in a small energy window get diffracted and focused on the sample. By careful adjustment, the crystal is aligned such that the $K_{\alpha1}$-line of Ti is deflected on the sample with an energy resolution of $\frac{\Delta E}{E} = 10^{-4}$.

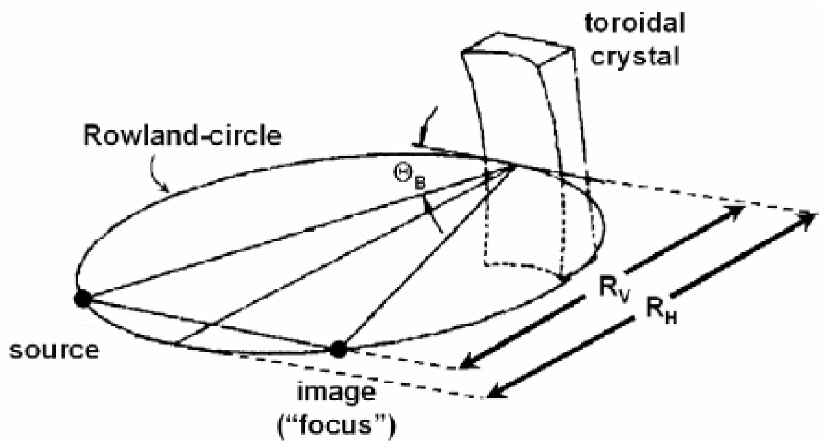

Figure 15: **Bent crystal optics.** The X-ray optics consists of a toroidally bent crystal in a Rowland-circle geometry. $\frac{R_V}{R_H} = \sin^2(\Theta_B)$ has to be fulfilled to ensure a 1:1 imaging of the source onto the sample (taken from [82]).

The bent crystal also determines the angular region, in which the X-ray diffraction patterns can be recorded. The X-rays are diffracted onto the sample with a convergence angle of approximately 1.4°. This is the maximum angular range, in which the diffraction patterns can be recorded at a time.

The path from the source to the sample is covered with He filled pipes. This reduces the loss of X-rays due to absorption in air. The photons get partially diffracted by the sample at a Bragg angle of $\theta_B = 76.5°$ and are detected by a Si based X-ray CCD. The CCD is cooled to $-30\,°\mathrm{C}$, which reduces the dark current. To avoid condensation of water on the cooled chip, the camera is pumped to a vacuum of 1×10^{-2} mbar. A pipe extension in front of the CCD is pumped to the same pressure and reduces the absorption of the diffracted X-rays.

A second window of the chamber allows the detection of X-rays for normalization to account for fluctuations in the X-ray production, e.g. due to laser fluctuations on short and long terms. An X-ray sensitive Si avalanche photodiode (APD) measures the $K_{\alpha1}$ photons diffracted by a GaAs crystal at that output. The APD signal is proportional to the emitted $K_{\alpha1}$ flux. Therefore, it is ideal for normalization of the diffraction images. By that, the diffraction signals can be normalized with an accuracy better than 2 % [2].

5.2 Samples

The samples studied in this work are heterostructures consisting of a thin metal film deposited on a semiconductor substrate, namely GaAs. Thin means film thicknesses in the order of 100 nm (see figure 16). The film thicknesses given in this work are measured via atomic force microscopy (AFM).

Such material systems are frequently used as so called optoacoustic transducers for the launch of picosecond acoustic waves. The metal film is excited with an ultrashort laser pulse and the absorption solely takes place in the metal since typical penetration depths are in the order of 10 nm. The shape of the acoustic pulse is therefore determined by the metal film and its microscopic properties. Hence, such a structure allows for the emission of picosecond acoustic pulses into various bulk materials, for instance even transparent substrates.

The metal films are either deposited by electron beam deposition or anodic vacuum arc. Since we are interested in the propagation of the acoustic pulse in the substrate, X-ray diffraction of a substrate Bragg peak, the (400) of GaAs, is performed.

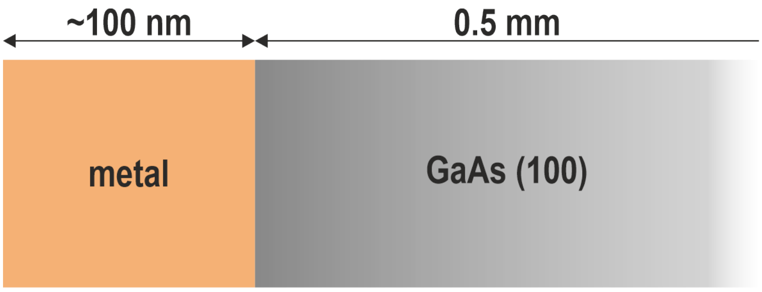

Figure 16: **Sample geometry.** The investigated samples consist of a thin metal film on top of a GaAs substrate. The substrate has a (100) surface orientation.

5.3 Measurements

The measurements for this work are performed using the pump-probe scheme. The sample surface is excited with an optical pump pulse and subsequently probed with a time-delayed X-ray pulse. The size of the pump beam on the sample is much larger than that of the probe beam. This provides homogeneous excitation conditions and since the lateral dimensions of the excitation are much bigger than the probed longitudinal length scales, the investigated problem reduces to one dimension.

The probe pulse is diffracted by the sample and measured by the CCD camera. If it arrives before the pump pulse, the unperturbed diffraction pattern is measured. By systematically varying the time delay Δt between the two pulses, snapshots of the sample at different times after the excitation are taken. As discussed in section 4.3.3, the excitation of picosecond acoustic waves alters the diffraction pattern, which can be measured with the pump-probe technique.

Before taking measurements the sample, pump and probe beam have to be arranged. The X-ray focal spot position is determined by the location of the source and the X-ray optics and therefore fixed in the setup. The sample is carefully positioned to the point of minimal X-ray spot size to avoid the so called "acoustic artifact" [121].

The spatial overlap between the pump and probe beam is found in a two step approach. This complicated procedure is necessary, because the X-rays are invisible and cannot be overlapped with the infrared pulse by visual inspection. First, rough overlap of the two beams is established using a phosphor screen next to the sample. For that the phosphor is illuminated by the X-rays. The weak luminescence is recorded and visualized with a camera at a long exposure time of 30 s. The pump beam is then moved to a coarse overlap with the X-ray spot using the motorized last mirror (MM).

Second, the fine adjustment is done by going to a time delay, where there is a clear, pump induced effect on the diffracted intensity. The pump beam is scanned around a grid surrounding the X-ray spot until the position of maximum change in the diffraction pattern is found, which is the perfect spatial overlap of the two beams.

A proper overlap is important to ensure that the measured fluence is actually deposited homogeneously in the probe area. If the two beams are displaced, the X-ray beam will probe a region with reduced fluence. Moreover, when positioned at the edge of the Gaussian pump beam, even small pointing instabilities/drifts of the beam positions over the duration of the measurement would lead to a significant change of the excitation fluence (see figure 17).

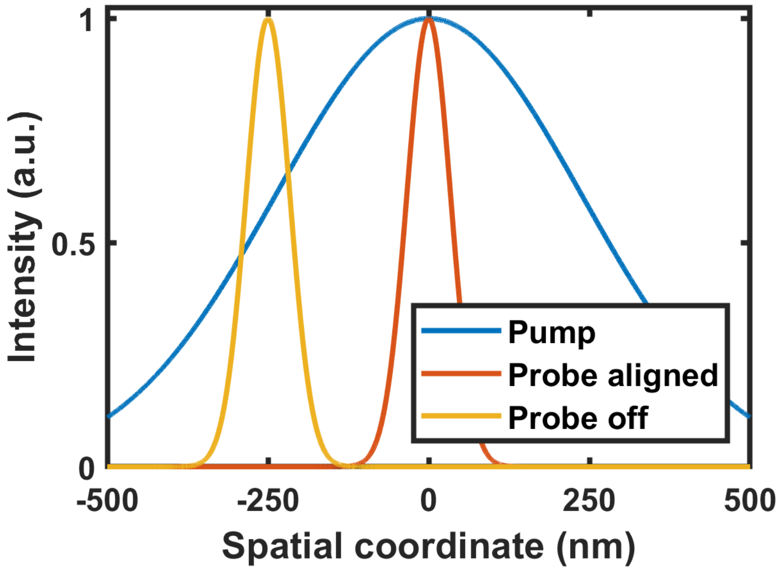

Figure 17: **Importance of spatial overlap.** Precise spatial overlap of pump and probe beam is necessary to ensure homogeneous excitation conditions.

The measuring procedure is as follows: At every given time delay, five images are recorded. Because the diffracted intensity is rather weak, the signal has to be integrated over an exposure time of around 1 min to achieve sufficient data quality.

The first one is an unpumped image, which means that no pump pulse excites the sample. This is taken for reference, to ensure that the experimental conditions remain constant during a typical duration of the measurement of 5 – 10 h. For instance, a spatial drift of the source or a degradation of the sample would lead to a change of the unpumped image curve and could be detected with the reference image. The second one is a dark image without pump and probe, which is used for background correction in the analysis. In principle, it would be sufficient to record one background image. However, having an up to date image for every time step rules out changes of the background.

Afterwards, three images with a pump pulse exciting the specimen at a fixed time delay to the probe pulse are taken. Because of the low repetition rate of the laser system, the deposited energy can fully dissipate between the pulses and every pulse excites a relaxed sample. The final pumped image is a sum of the three single ones.

For every image, the APD signal is measured. This allows for the normalization of all images with respect to the X-ray flux. Additionally, for the pumped images a photo diode is used to measure the integrated pulse energy and adjust the fluence via the motorized $\lambda/2$-plate if necessary.

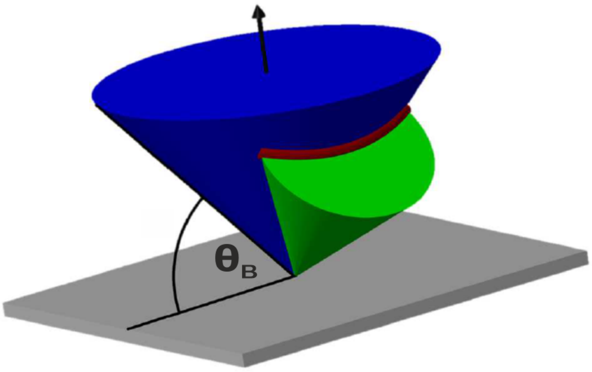

Figure 18: **Cause of bending.** The geometry of the setup leads to bent "rocking curves" on the detector, because the measured curve is the intersection of two cones (taken and adapted from [1]).

5.4 Data Analysis

The diffraction patterns ("rocking curves") are recorded on a 2-dimensional CCD detector. Because of the special geometry, they are bent. The incoming convergent X-ray beam has the shape of cone. What is actually measured is the intersection of this cone with the so called Kossel cone, which is oriented perpendicular to the sample surface for symmetric Bragg diffraction and whose opening angle is equal to (180° - $2\theta_B$). The intersection of these two cones is shown in figure 18.

As a first step in the data analysis, the background images are subtracted from the diffraction images. Secondly, the bending has to be corrected to increase angular resolution. The procedure is shown in figure 19. For this, the image is divided into 24 sections in vertical direction (white lines). A cross section of each one is calculated and a Gaussian function is fitted to the peaks. Fitting a parabola through the maximum position of these Gaussians (purple circles) yields a measure for the shift. The bending is corrected by shifting each line by this amount. Finally, a cross section in y-direction yields the diffraction pattern.

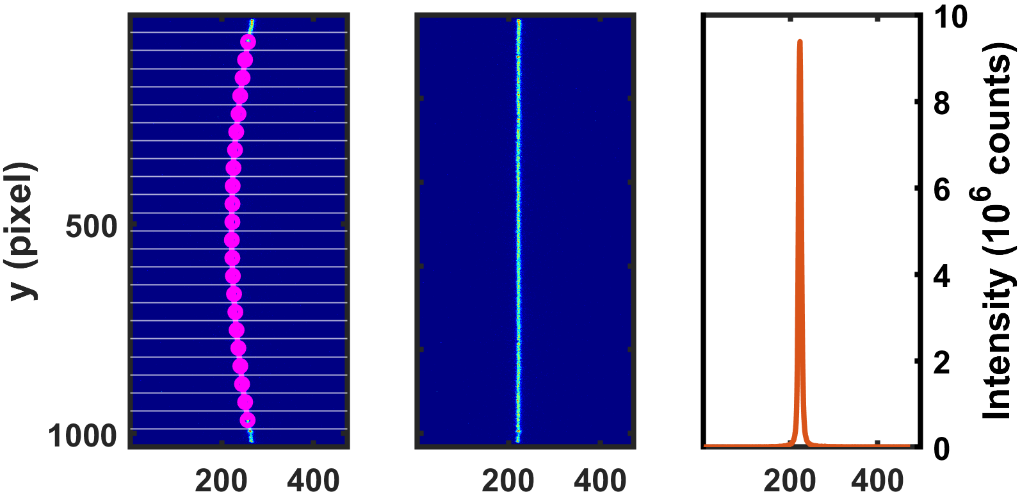

Figure 19: **Bending correction.** Schematic of the bending correction algorithm. The left hand side image shows the bent "rocking curve", the middle image the corrected one. The curve on the right hand side is the cross section in y-direction.

After the unbending procedure, two more steps are executed. For a better noise reduction the average intensity is determined in a region far apart from the main peak, where all intensity recorded is clearly attributed to noise. This background noise is subtracted from the diffraction pattern. At last, the images are normalized to the number of incident photons using the APD signal.

6 Results, Discussion and Modeling

In this section, the results of the previously described experiments are presented and discussed. It is structured as follows: First, the general shape of acoustic pulse trains in the investigated sample geometry is explained. Second, the experimental results are shown and some general features are discussed. Third, the mechanisms of stress generation after optical excitation are described. In the last part of the chapter, a detailed quantitative model is presented for two of the material systems and the simulated diffraction patterns are compared to the experimental results. A comparison with fluence dependent experiments shows the general applicability of the presented model over the observed fluence range.

6.1 Picosecond Acoustic Waves in Metal Semiconductor Heterostructures

The general layout of the metal-on-semiconductor heterostructures studied in this work has been described in chapter 5.2. In the following, the emission of an acoustic pulse in these heterostructures is illustrated with an example.

The simplest possible example of acoustic pulse generation in such a material system is that of a spatially homogeneous and temporally constant stress in the metal film and no stress in the substrate. This is depicted in Fig. 20. Imagine a metal film with thickness t_{M}, which is excited with an ultrashort laser pulse at $T = 0$. The absorbed energy is distributed homogeneously over the whole film, which leads to a constant stress. Direct excitation of the substrate and transport across the interface is omitted, thus there is no stress in the substrate. The characteristic time of the system is given by the traveling time of an acoustic wave through the film: $T_{\mathrm{c}} = \frac{t_{\mathrm{M}}}{c}$ with the metal sound velocity c.

According to equation 23, a non-vanishing second derivative of stress is a source of strain waves. Hence, strain waves are emitted at the surface and the interface between the materials. From a simple thermoelastic point of view this scenario can be understood as an ultrafast heating of the film, which subsequently leads to rarefaction waves starting at the surface and the interface. Correspondingly, since the metal film expands, the GaAs substrate is compressed leading to a compression wave. These strain waves are shown in the third row of figure 20 at a point in time shortly after excitation.

After $T = \frac{t_{\mathrm{M}}}{2c}$ the waves meet in the middle of the film and add up for an even higher rarefaction (fourth row). The next picture shows the waves at $T = T_{\mathrm{c}}$. The metal film is homogeneously strained, because the two expansion waves have reached the surface and the interface, respectively. The strain waves are reflected at the surface and partly reflected and transmitted at the interface. This leads to an expansion wave propagating into the substrate. Meanwhile, the compression wave has propagated into the GaAs substrate. Its length is determined by the ratio of the sound velocities c_{GaAs}, c_{M} and the thickness of the film t_{M}:

$$t_{\mathrm{GaAs}} = \frac{c_{\mathrm{GaAs}}}{c_{\mathrm{M}}} t_{\mathrm{M}} \tag{35}$$

At $T = 2T_{\mathrm{c}}$, a first compression and expansion part have fully entered the GaAs substrate. This combination will be called a "bipolar pulse", because it consists of parts with both signs of strain. The film is homogeneously strained again, but with a decreased strain level, because of the finite transmission of the interface.

The waves in the metal film are repeatedly reflected back and forth. At every cycle a part of the energy is transmitted into the GaAs. This results in a pulse train of alternating compressions and expansions. The amplitude of the single parts decreases with time due

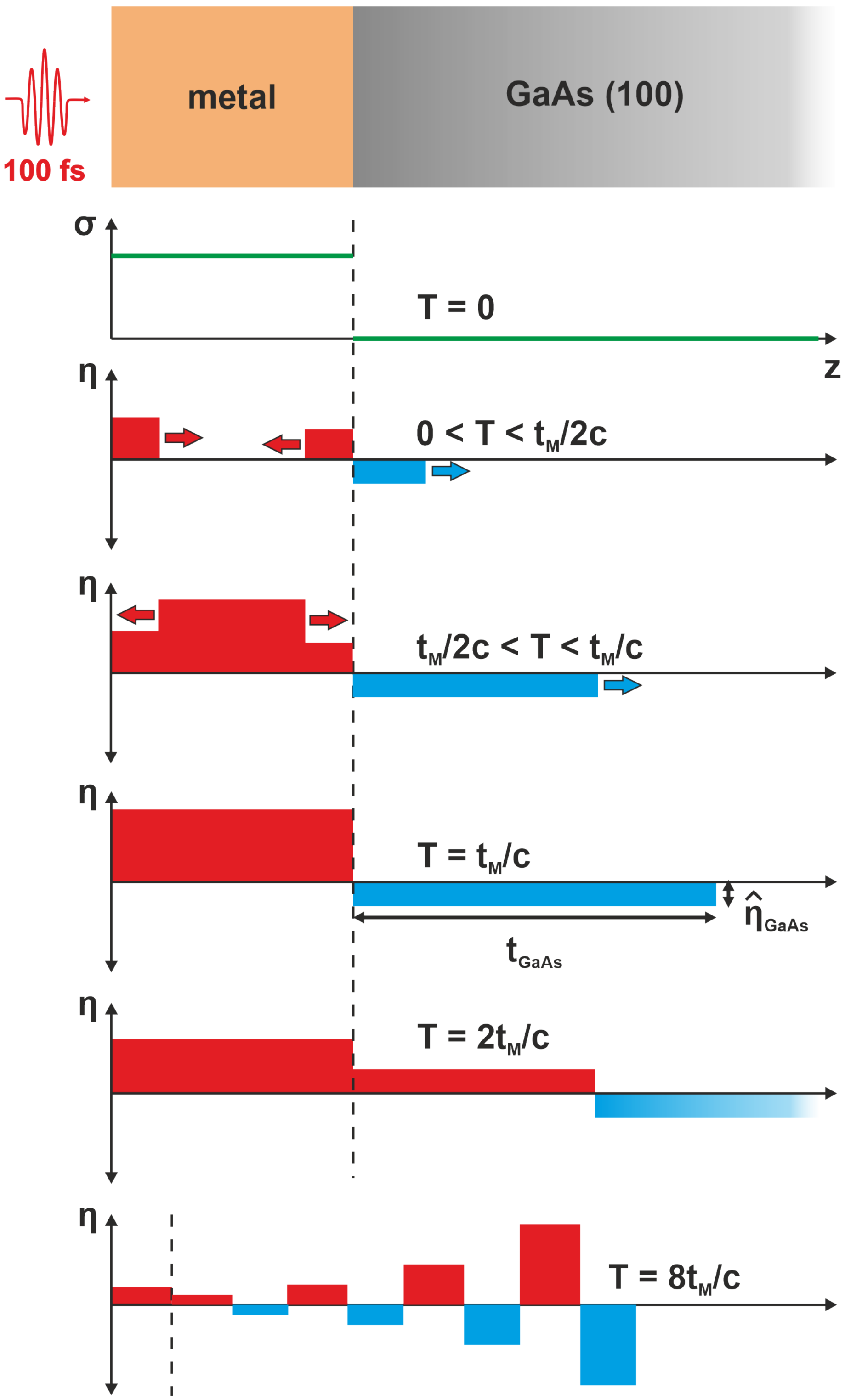

Figure 20: **Emission of picosecond acoustic waves.** The series shows the time evolution of a picosecond acoustic wave in a metal-semiconductor heterostructure for a simple configuration of a spatially homogeneous stressed metal film, which is time independent. Expansion is shown in red and compression is shown in blue. The characteristic time scale of the problem is the acoustic traveling time of a pulse through the film $T_\mathrm{c} = t_\mathrm{M}/c$. After each iteration the next acoustic feature enters the GaAs substrate. The amplitude of the consecutive pulse train components decreases according to the interface acoustic reflection coefficient every two pulses.

to the loss of energy in the transmission at the interface. The resulting pulse train at $T = 8T_\mathrm{c}$ is depicted in the last sketch of figure 20. This pulse train can also be thought of as a repetition of the first bipolar pulse with decreasing amplitude. The amplitude reduction is determined by the interface reflection coefficient R defined in equation 24.

However, this is a simplified picture of stress generation in metal films. In real metals effects like transport or different sources for non-mechanical stress can lead to space and time dependent stress. This changes the shape of the pulse train. A quantitative understanding of the differences in acoustic pulse generation for different metals is desirable for a better knowledge of the underlying processes as well as for their efficient use as optoacoustic transducers. By measuring the transient changes of the (400) Bragg peak of GaAs, we aim to disentangle the stress generation processes in different metal films and thus the acoustic wave emission in opto-acoustic transducers. This will be described in the following.

6.2 Experiments on Metals on GaAs (400)

For the investigation of picosecond acoustics in metal films on GaAs, we performed pump-probe measurements as described in the previous sections. Figure 21 shows the time evolution of the diffracted X-ray intensity in the vicinity of the (400) Bragg peak of GaAs for various excited metal films. The intensity is depicted by the color code and each map is normalized such that the intensity of the unpumped diffraction pattern has a maximum value of unity.

To reduce the influence of noise, the signal has been smoothed using a 5-point moving average filter apart from the rocking curve ($|\theta - \theta_B| > 0.08\,°$) to remove high frequency noise. This was done taking great care, that neither the position nor the strength of the pump induced side maxima was changed. Slightly different angular regions have been chosen for the plots, to focus on the pump induced changes for the different materials and excitation conditions.

To compare the influence of different metals on the acoustics, the experiments were performed for 5 different metals: Aluminum, palladium, gold, platinum and titanium. For aluminum, palladium and gold the measurements were also done at two fluences to compare different excitation conditions. The respective incident fluences are shown in the graphs.

The time resolved X-ray diffraction results exhibit a complex behavior and differences between the various material systems and also dependencies on the excitation conditions are obvious. In the following this will be discussed in more detail and the acoustics will be quantitatively modeled for two cases.

A few observations are common for all samples. At first, it is visible that some picoseconds after the excitation satellites start to appear on both sides of the main peak. With increasing delay, these satellites move towards the main peak and new satellites appear. This behavior is well known for diffraction from acoustic pulses generated in bulk materials (e.g. [100]).

Second, the satellites appear on the two sides alternatingly, always starting at positive angular deviation - the compression side - followed by negative angular deviation. This is a footprint of the form of the acoustic pulse. Due to the structure of the samples, the leading-edge of the pulse is always compressive (i.e. negative strain).

The "fish bone" structure can be understood in real as well as in reciprocal space. In the latter one, the diffraction of X-rays with acoustic waves is the inelastic scattering of the X-rays with phonons (see chapter 4.3.3). Each angle corresponds to a phonon mode with wave vector q and the intensity at that angle oscillates in time with the oscillation frequency given by the dispersion relation in equation 25.

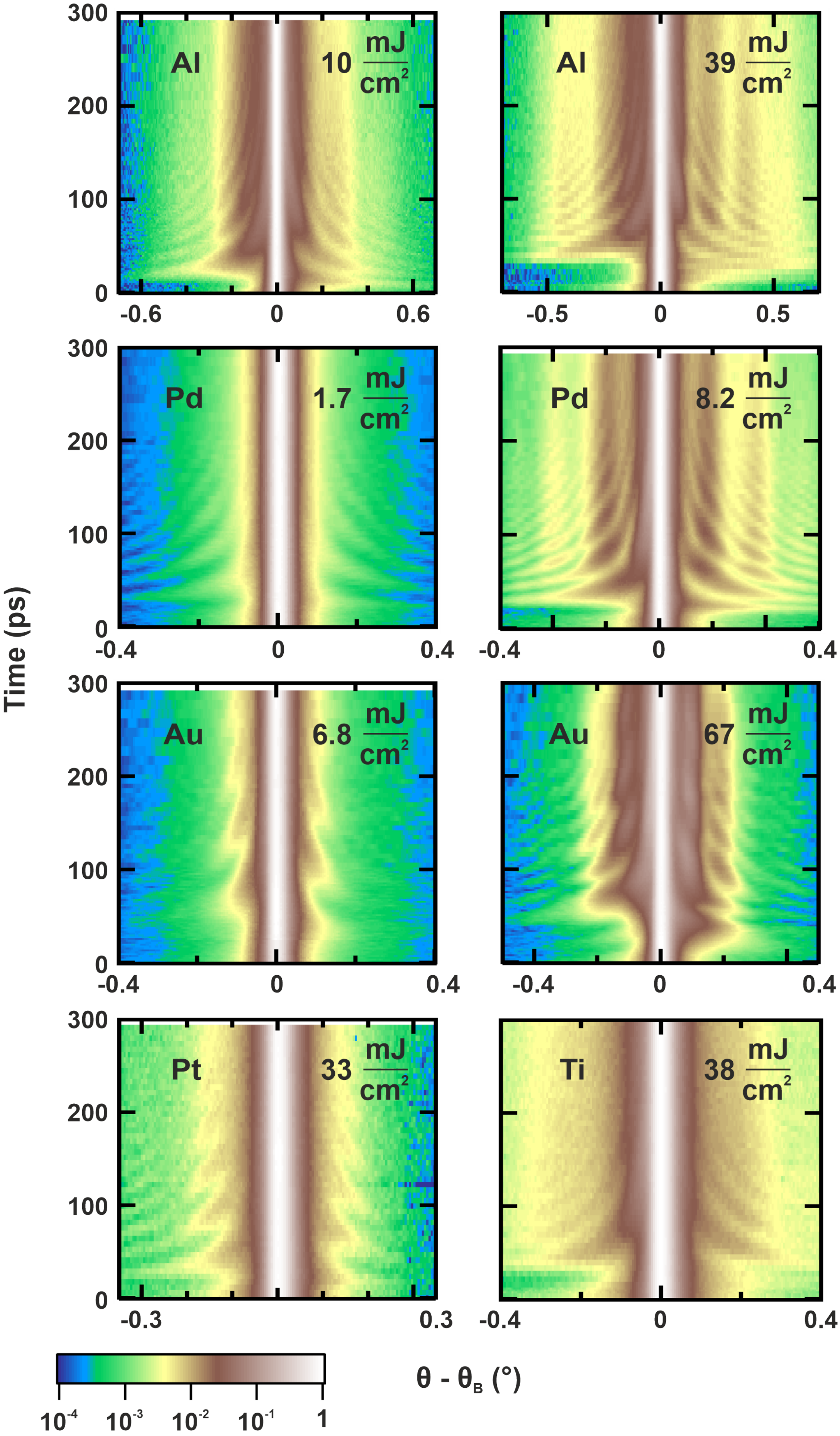

Figure 21: **Experimental results on ultrafast acoustics for different materials.** This figure shows results for various material systems (aluminum, palladium, gold, platinum and titanium) and excitation conditions. The diffracted X-ray intensity is encoded in a color code.

To extract the angular frequency of the phonon modes, the Fourier transform with respect to the delay time has been taken for every angle. Figure 22 shows this in a 2D false color representation exemplary for the low fluence measured on Pd/GaAs. The normalized intensity is encoded in the color code. The x-axis is converted into a wave vector axis following equation 28. Prior to taking the Fourier transform, the diffraction patterns have been multiplied with a function of the form $(1 - G(\Delta\theta))$, where G is a Gaussian. This prevents experimental noise around the main peak from dominating the signal.

As can be seen, the maximum amplitude is located on two branches, starting from the origin and following a linear curve. This reflects the fact that we are looking at low wave vector acoustic phonons, which follow a linear dispersion (compare equation 25).

Indeed, the speed of sound of GaAs in (100) direction can directly be extracted as the slope of the branches from the experimental data. By fitting a linear function to the maximum amplitude for each frequency on both branches, shown as a red dashed line, we can determine the sound velocity to be $c^{(100)}_{\mathrm{GaAs}} = (4726 \pm 22)\,\frac{\mathrm{m}}{\mathrm{s}}$, which is in agreement with the literature value of $4730\,\frac{\mathrm{m}}{\mathrm{s}}$ [16]. The only fit parameters in this model are the origin of the wave vector and the slope of the branches. Values in the black dashed cone are omitted for this analysis. They are not located on the main branch and originate from noise.

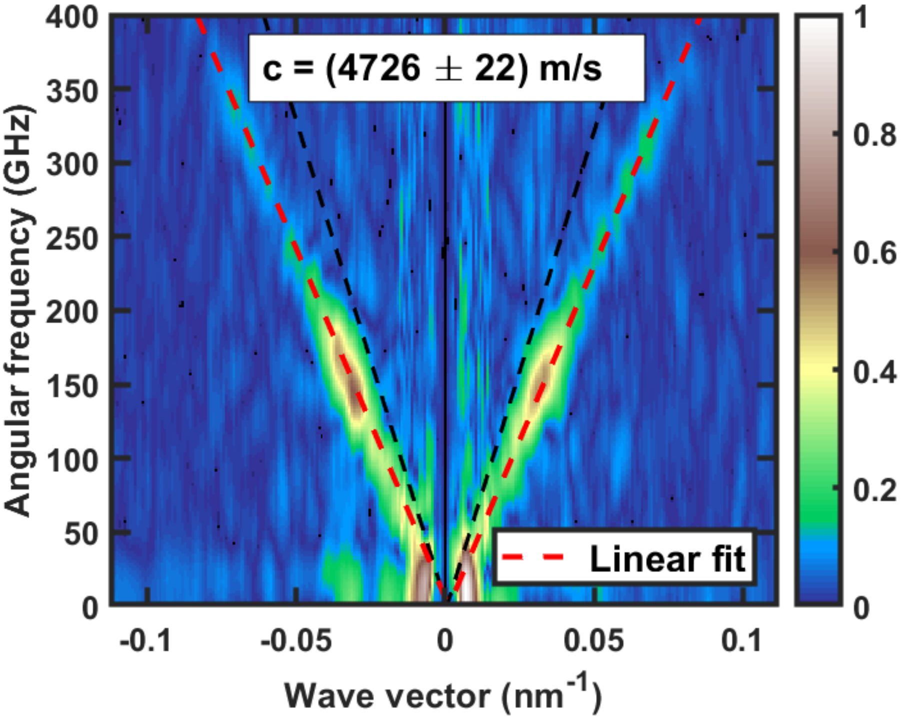

Figure 22: **Acoustic phonon dispersion relation from time-resolved X-ray diffraction.** The linear dispersion relation of the acoustic phonons close to the Brillouin zone center building picosecond acoustic waves can be extracted from time-resolved X-ray diffraction data by taking the Fourier transform in time for every angle. A linear fit (red dashed line) through the branches of maximum amplitudes yields the sound velocity, which is in good agreement to the literature value for (100) oriented GaAs. The data points inside the black dashed cone are omitted in the fitting process, because they are not located on the acoustic phonon branches.

An equivalent real space interpretation of the fish bone structure is explained in the left part of figure 23. The upper part shows the most minimalist view of an acoustic pulse traveling from an interface into a substrate. It consists of two discontinuities in the density: The interface between the film and the substrate, and the most prominent feature of the acoustic pulse train, which is the sign change of the strain in the first bipolar pulse as described in section 6.1. The distance d_1 between these two discontinuities increases with time, since the pulse is traveling into the substrate.

X-rays reflected from the two discontinuities (1 and 2) interfere and the resulting interference pattern is the Fourier transform of the structure, that means the Fourier transform of a rectangle. This is indeed a sinc-function whose side maxima move towards the center with time. The lower left image in figure 23 shows the Fourier transform of the situation shown above. As can be seen, the transient changes of the sinc-function cause a fish bone structure as is visible in our data.

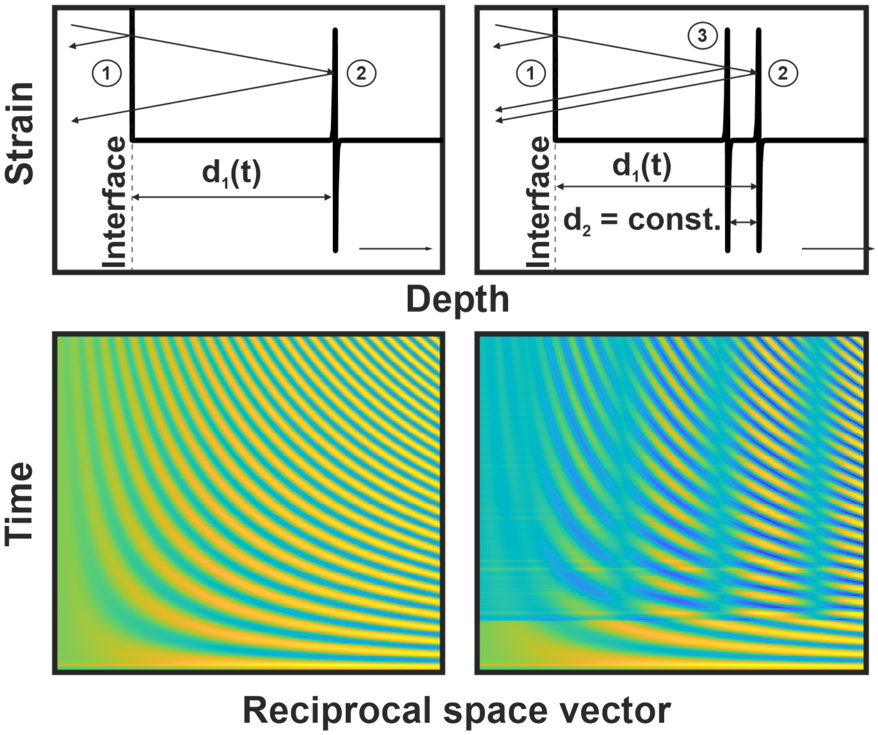

Figure 23: **Visualization of the general appearance of time-resolved X-ray diffraction patterns from acoustic waves in bulk materials.** This figure illustrates the real space interpretation of the creation of fish bone structures in transient diffraction patterns as interference effects of X-rays reflected from an interface and a density discontinuity traveling into a substrate and the corresponding Fourier transform (left column). It also demonstrates the intensity enhancement at distinct wave vectors (angles) as an additional interference from a second traveling discontinuity (right column).

As a last similarity between the different samples, the amplitude of the intensity oscillations at a fixed angle decreases with time delay (see Fig. 24). This effect is independent of the metal used and can also be seen for different fluences. In principle, two effects can be responsible for this. The first one is damping of the acoustic pulse, while traveling through the material. However, even if the pulse is not altered in time, the amplitude of the oscillations would decay. This is caused by the second effect. Since a finite pulse train travels into the substrate, the X-rays have to pass the material above the pulse before scattering with it. They lose intensity due to absorption on that way. Hence, the further the pulse has traveled into the GaAs, the more the oscillation intensity is damped.

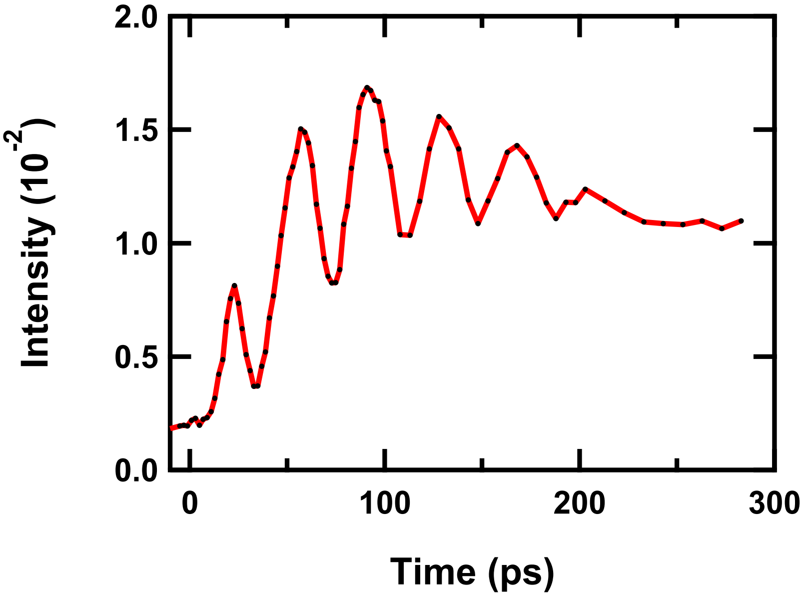

Figure 24: **Oscillation of the diffracted intensity for a specific phonon mode.** This graph shows a vertical cut through the 2D false color plot of the Pd measurement for an incident fluence of $8.2\,\frac{\mathrm{mJ}}{\mathrm{cm}^2}$ at an angle of 0.2°, which corresponds to a phonon wave vector of $q = 0.037\,\mathrm{nm}^{-1}$. The intensity increases shortly after time zero and an oscillation builds up. The initial increase originates in the acoustic pulse train entering the substrate. After approximately 100 ps the oscillation intensity starts to decrease. Several reasons can be responsible for that as acoustic damping, or effects of X-ray absorption as the X-rays have to travel deeper into the sample before scattering with the strain pulse. The red line is a guide to the eye.

Nonetheless, there are also clear differences between the materials. To begin with, experiments at higher fluences generally show more pump induced intensity contributions apart from the main peak. This is plausible, because a higher excitation fluence generally creates higher amplitude acoustic waves, which lead to more diffracted intensity away from the Bragg peak.

Additionally, the measurements at higher fluences show enhancements at particular fixed angles, while the intensity is suppressed at other angles. This behavior can again be interpreted in reciprocal as well as in real space.

In the reciprocal space image, the enhancement is indicative of the amplification of specific phonon modes. These are the dominant phonon modes of the pulse, whose wave vector is connected to the acoustic pulse properties via $q = n\pi/t_{\mathrm{GaAs}}$ with n being an integer.

The right part of figure 23 shows the interpretation in real space. In contrast to the weak excitation discussed before, the amplitude of the second bipolar pulse becomes relevant now. With that, a second moving discontinuity has to be taken into account. This introduces a second thickness d_2 to the system, which is constant as the wave travels. In this situation, three rays interfere with each other. The interaction of the rays 1 and 2, and 1 and 3, respectively, forms the fish bone structure again (see Fourier transform in the lower image). However, this is now overlapped by the interference of the waves 2 and 3, which have a constant phase relation and hence enhance or decrease the signal at fixed wave vectors.

Comparing the different metals, some show a concentration of the additional intensity closer to the rocking curve (Au), while others show a spread of the pump induced intensity over a wider angular range. This effect is not depending on the excitation fluence as it can be seen for low and high fluences.

To conclude, the experiments on different metal films on top of GaAs substrates show a complicated transient evolution of the diffraction intensity in the vicinity of the Bragg peak. To get a deeper material specific and even quantitative understanding, a detailed analysis is necessary. In the following, the stress generation mechanisms and the subsequent acoustic response are discussed in detail. This knowledge will then be applied to two of the systems, where a detailed model is developed.

6.3 Stress Generation upon Optical Excitation

As described in section 4.3, stress leads to an acoustic response of solid materials. Non-mechanical stress according to equation 19 can be caused by several different sources.

First, ultrafast changes of the lattice temperature lead to a thermodynamic non-equilibrium, which is a source of thermoelastic stress. The new temperature is connected to a new equilibrium position of the atoms. Since initially the atoms are still located at their original position, restoring forces occur, which induce stress. This is often referred to as the phononic part of stress.

Second, a change of the electron distribution due to optical excitation of a material gives rise to electronic stress caused by changes of the interatomic potential [104]. Every change of the electronic distribution, e.g. an optical excitation of the electronic system, results in a change of the charge carrier density in the system. This alters the interatomic forces of the lattice represented by the crystal potential and thus yields a new equilibrium position of the atoms. Subsequently, the lattice relaxes to the new equilibrium by excitation of acoustic waves.

Last, there are also other sources for stress in solids such as the inverse piezoelectric effect, electrostriction or magnetostriction. These effects are only relevant in the respective materials (e.g. ferromagnets [57, 58, 115, 133]). Therefore, they are not considered here. Additional information can be found in the literature [104].

6.3.1 Two Temperature Model

A frequently used model to describe the non-equilibrium response of metals to optical excitation with an ultrashort laser pulse is the two temperature model (TTM) [6]. In this model the subsystems of electrons and phonons are described separately by corresponding temperatures T_e and T_l. They exchange energy due to scattering until both systems are in thermal equilibrium. This is the case, when they have reached the same temperature. The strength of the energy transfer is given by the electron-phonon coupling constant G. The temperature evolution of the subsystems is given by the coupled differential equations:

$$\begin{aligned} C_e(T_e)\frac{\partial T_e}{\partial t} &= \nabla[\kappa_e(T_e)\nabla T_e] - G(T_e - T_l) + S(z,t), \\ C_l(T_l)\frac{\partial T_l}{\partial t} &= \nabla[\kappa_l(T_l)\nabla T_l] + G(T_e - T_l), \end{aligned} \tag{36}$$

where C_e and C_l are the electron and lattice specific heat and κ_e and κ_l are the thermal conductivities of the electrons and the lattice, respectively. S is the source term and describes the energy deposition by the laser pulse. Whenever the laser pulse duration is short compared to the relevant timescales of the problem, the excitation can be assumed to happen instantaneously. In that case, S is approximated by a Heaviside function.

In the frame of the TTM the absorption and subsequent energy relaxation of a femtosecond laser pulse can be understood as follows. The whole energy is absorbed by the electrons creating a hot electronic system, while the lattice remains cold. Subsequently, electron-phonon coupling sets in and energy is transferred to the lattice until thermal equilibrium is reached.

Changes of the temperatures of the subsystems lead to stress [138]:

$$\delta\sigma_{\mathrm{tot}} = -\gamma_e C_e \delta T_e - \gamma_l C_l \delta T_l, \tag{37}$$

where γ_e and γ_l are the average Grüneisen parameters and δT_e and δT_l are the temperature changes of the electron and lattice system, respectively. If the material parameters are known, the stress evolution can be calculated from the temperature changes.

Even though the two temperature model is successful in explaining various systems, it has its limitations due to the underlying assumptions, which are not valid generally:

- It assumes an initially thermalized electronic system [26].
- The energy transfer between the subsystems is not regarded as mode specific [135].
- The phonon system is considered as thermalized for all times as well [117].

These limitations have to be kept in mind. For every application, it has to be checked carefully, whether the TTM is applicable. For our case, the TTM seems to describe the physics well and thus it is exploited in the following.

So far, the discussion has only taken into account the transient changes of the electron and lattice temperature. This is only valid for a spatially homogeneously excited specimen. For spatially inhomogeneous excitation energy transport plays a role as will be shown in the following discussion. All in all, a complicated interplay of different microscopic processes like absorption, transport, and subsystem coupling determines the spatiotemporal evolution of stress and the resulting acoustic response of the material.

6.4 Metric for Transient Rocking Curve Comparison

It is necessary to define a scalar metric to compare two-dimensional diffraction patterns. By minimizing such a metric for the measured and simulated patterns, it is possible to develop models describing the underlying physics and to find the optimal parameters of these models. In the following, the mean average percentage error (MAPE) will be used as a metric:

$$\mathrm{MAPE} = \frac{100}{N_\theta N_t} \sum_{\theta,t} \frac{|(I_1(\theta,t) - I_2(\theta,t)|}{I_1(\theta,t)}, \tag{38}$$

where I_i are the angle and time dependent diffraction intensities and N_θ and N_t are the number of angle bins and the number of time steps of the diffraction pattern. This metric normalizes the difference of the two intensities at each point in angle and time to the first intensity and averages the result over all "pixels". This has the advantage, that a change between the two diffraction patterns at a low intensity, e.g. 10^{-3}, has the same influence on the metric as a change at high intensity. This is important, because the intensities of the relevant features in the diffraction patterns vary over orders of magnitude.

Though, this also comes with a disadvantage, one has to be aware of. At low intensities the signal to noise ratio decreases. Especially, when two patterns are in good agreement, the role of noise increases and deviations originating from noise can dominate the MAPE.

Even a good model will rarely reach the theoretical limit of 0 %, but will always exhibit an offset. This originates in the points, where there are still slight differences between the two curves and is even more pronounced, if noise causes additional deviations.

Hence, there is always some kind of offset, especially if two different models are compared to each other. Because of that deviations of only a few percent should be treated with care and do not necessarily mean that one model is superior. However, if the comparison is done within one model with varying parameters, even small differences can be meaningful.

Another issue which can limit the mathematical agreement of two patterns with such point by point comparison is an imperfect determination of the temporal and angular origin. Great care was taken to determine these as good as possible, but nevertheless this is a potential source for inaccuracies.

6.5 Modeling of the Acoustic Response

One way to interpret time-resolved X-ray diffraction results is called the "modeling approach" in the following. One starts from the microscopic processes upon optical excitation like absorption, transport or energy coupling between the subsystems. This is followed by simulating the induced acoustic response and calculation of the resulting diffraction of the incoming X-ray beam. By that, for every point in time it is possible to determine the strain distribution $\eta(z,t)$ and according to section 4.1.3 the transient diffraction patterns $I(\theta,t)$.

A comparison of the calculated X-ray intensities to the measured ones allows to judge, whether the microscopic processes were correctly described for the specific material system. This comparison is done by using the MAPE-metric introduced in the previous paragraph. The complexity is further increased, because energy redistribution, stress generation and acoustic wave emission are not necessarily separated in time, but happen indeed simultaneously. A sketch of this analysis scheme is shown in figure 25.

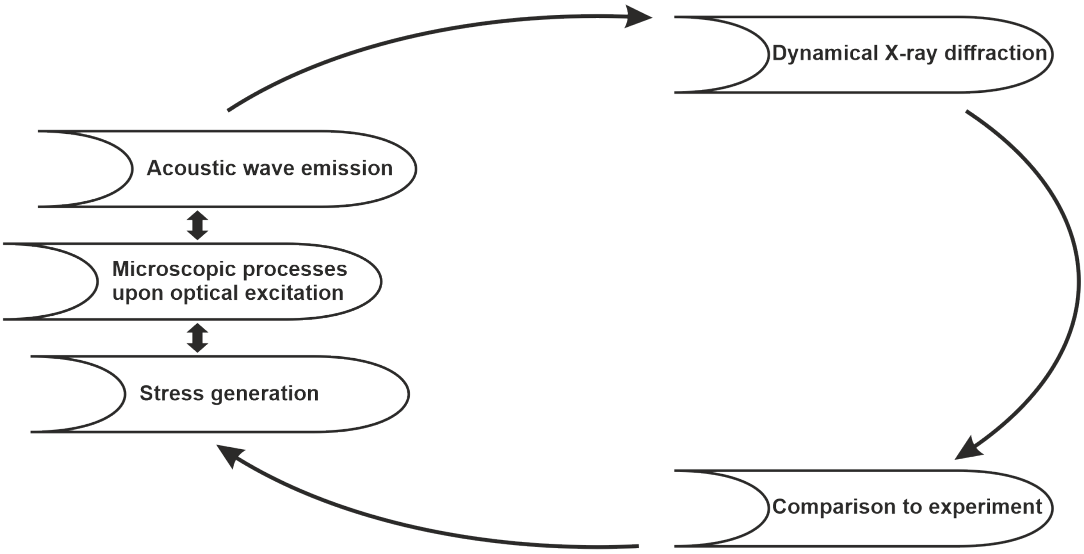

Figure 25: **Workflow of modeling.** Visualization of the iterative modeling workflow used to describe the experimental results.

In the next two sections it will be shown that such a modeling allows in some cases for the quantitative understanding and identification of the relevant microscopic processes and material properties for the acoustic wave emission. This analysis focuses on two examples from the experimental results presented before. Gold and palladium present two limiting cases of "slow" and "fast" electron-phonon coupling and the following analysis reveals how this influences the acoustic response.

For both systems a microscopic model will be presented, discussed and compared to the experimental results. Besides the parameters of the models both systems have two "fit" parameters in common, which originate in the experimental conditions: The maximum strain $\hat{\eta}_{\mathrm{GaAs}}$ in the substrate and the thickness of a single pulse t_{GaAs} (see figure 20).

The pulse thickness in the substrate is connected to the metal film thickness via equation 35. However, the metal sound velocity depends on the structure of the metal film and is therefore not exactly known. To get around this problem, the pulse thickness is taken as a free parameter and from that the metal sound velocity is derived and compared to literature.

6.5.1 Gold

The absorption length for light with a wavelength of 800 nm light in gold is 13 nm [53]. Hence, the laser energy is completely absorbed by the electrons in the metal film and the GaAs is not excited. However, electronic transport in gold is very fast and therefore the energy is efficiently distributed over the whole film thickness within a few hundred femtoseconds [11, 49] leaving the film with an excited electronic distribution. Meanwhile, the lattice is still not excited, because electron-phonon coupling is comparably weak in gold [83, 122]. Therefore, we assume a spatially homogeneous distribution of the energy over the metal film. This leads to stress which is only time dependent.

The strain wave emission is hence determined by the coupling of the energy between the subsystems and the time evolution of the induced stress, which will be analyzed in the following. First, the phenomenological model by Nicoul et al. will be deployed [83] for the experiment at high fluence (see figure 21). Second, a two temperature model simulation is performed. By comparison to the result using the Nicoul model it is shown that the deviations between the two models are negligible and that both are equally well suited for describing the measurement within the sensitivity of the experiment. Because of its simplicity the Nicoul model is used for the following analysis of the low fluence measurement as well as for the discussion of the fluence dependent experiments in part 6.5.3.

Nicoul et al. have studied the acoustic response of an epitaxial gold film on a Mica substrate [83]. They could explain their observations of the transient shifts of the (111) Bragg peak of Au by assuming an exponential transformation of electronic to thermal stress due to energy transfer between the subsystems. This phenomenological approach is an approximation to the two temperature model (see below). Initially, there is nonzero electronic stress and no thermal stress. The transient evolution of the total stress can be described by:

$$\sigma_{\text{tot}}(t) = \sigma_\infty H(t)\left[1 + \left(\frac{\gamma_e}{\gamma_l} - 1\right)\exp\left(-\frac{t}{\tau}\right)\right], \tag{39}$$

where $\sigma_\infty = c_M^2 \rho \eta_\infty$ is the stress after equilibration without any thermal transport losses. It is given by the sound velocity c_{M}, the density ρ and η_∞, the strain after equilibration[5]. $H(t)$ is the Heaviside function, which yields an instantaneous stress generation at $T = 0$. The parameters determining the temporal evolution of the stress are the Grüneisen parameters of the electronic and the lattice system γ_e and γ_l together with the electron-phonon coupling time τ. This description assumes, that electronic excitation and transport happen "fast" compared to the time scale of electron-lattice equilibration and acoustic wave emission.

The absorbed fluence is connected to the strain in the metal after equilibration via:

$$F_{\text{abs}} = \frac{t_{\text{M}} C_V c_{\text{M}}^2 \rho}{3B\beta} \eta_\infty, \tag{40}$$

---

[5] η_∞ is a theoretical value, the system would relax to without any losses. In practice it is not reached, because there are energy losses e.g. heat conduction through the interface.

where t_{M} is the thickness of the metal film, ρ is the density, B is the bulk modulus and β is the linear thermal expansion coefficient.

The model contains two additional parameters to the two fit parameters $\hat{\eta}_{\mathrm{GaAs}}$ and t_{GaAs} discussed in the previous chapter: The first is the ratio of the electronic and lattice Grüneisen parameters, which is $\gamma_e/\gamma_l = 0.5$ for gold [83]. The second parameter is the electron-phonon coupling time τ, which is fluence dependent (see [122] and references therein). The stress after equilibration is proportional to the maximum strain in GaAs.

To find the best approximation to the experimental result, the coupling time was varied in discrete steps of 0.5 ps, while the maximum strain and the pulse thickness were used as free parameters to achieve the optimal agreement between model and experiment. The parameters were varied until the minimal MAPE was reached for every coupling time. The results are depicted in figure 26. All used material parameters are given in table 1.

t_{M}	$120\,\mathrm{nm}$
t_{GaAs}	$170\,\mathrm{nm}$
c_{M}	$3380\,\frac{\mathrm{m}}{\mathrm{s}}$
R	0.44
T_{c}	$35\,\mathrm{ps}$
c_{GaAs}^{100}	$4730\,\frac{\mathrm{m}}{\mathrm{s}}$ [16]
ρ	$19.3\,\frac{\mathrm{g}}{\mathrm{m}^3}$ [37]
B	$1.73 \times 10^{11}\,\mathrm{Pa}$[55]
β	$1.42 \times 10^{-5}\,\frac{1}{\mathrm{K}}$ [68]
C_V	$2.49 \times 10^{6}\,\frac{\mathrm{J}}{\mathrm{m}^3\,\mathrm{K}}$ [68]
A_e	$67.6\,\frac{\mathrm{J}}{\mathrm{m}^3\,\mathrm{K}^2}$ [67]
ξ_{opt}	$13\,\mathrm{nm}$ [53]
γ_e/γ_L	0.5 [83]
G	$1.7 \times 10^{16}\,\frac{\mathrm{W}}{\mathrm{m}^3\,\mathrm{K}}$ [122]

Table 1: **Parameters for the acoustic simulation of the excited gold film.** The metal thickness t_{M} was measured using atomic force microscopy. The thickness inside the GaAs t_{GaAs} is a free parameter. The speed of sound in the metal c_{M}, the interface reflectivity R and the characteristic time T_{c} are calculated from that values using equations 35 and 24. All other parameters are taken from the literature. The respective references are given in the table.

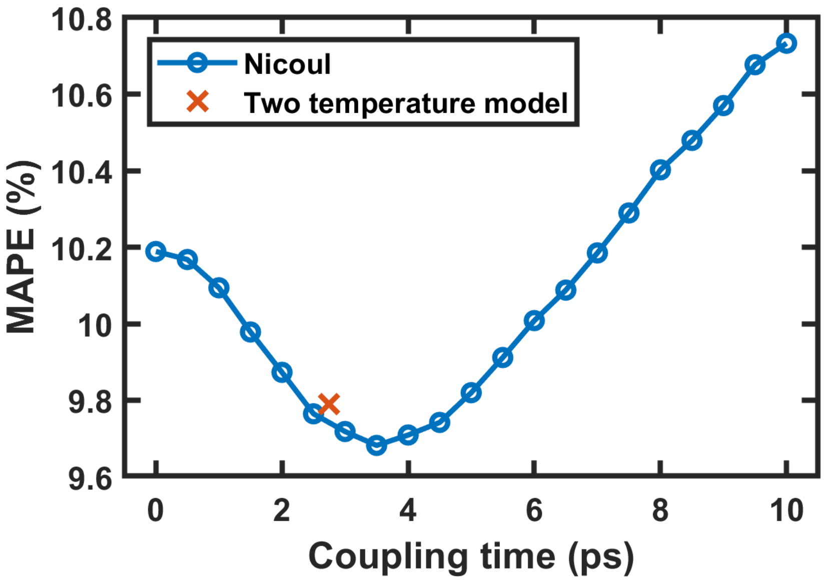

Figure 26: **Mean average percentage error for variation of coupling time in gold.** The blue circles show the best achievable MAPE as a function of the coupling time. The blue line is a guide to the eye. The red cross marks the optimal MAPE obtained from the two temperature model for $T_\infty = 28.4\,\mathrm{K}$.

As can be seen, the optimal result is obtained for a coupling time of $\tau = (3.5 \pm 1.0)$ ps. The corresponding values for t_{GaAs} and $\hat{\eta}_{\mathrm{GaAs}}$ are 170 nm and 4.9×10^{-4}. The resulting pulse train in GaAs for $T = 6T_c$ is shown in the left panel of figure 27. The leading front of the acoustic pulse has traveled 1000 nm into the substrate as expected for the sound velocity of GaAs (100) $c^{100}_{\mathrm{GaAs}} = 4730\,\frac{\mathrm{m}}{\mathrm{s}}$ and the characteristic time of the gold sample $T_c = 35$ ps.

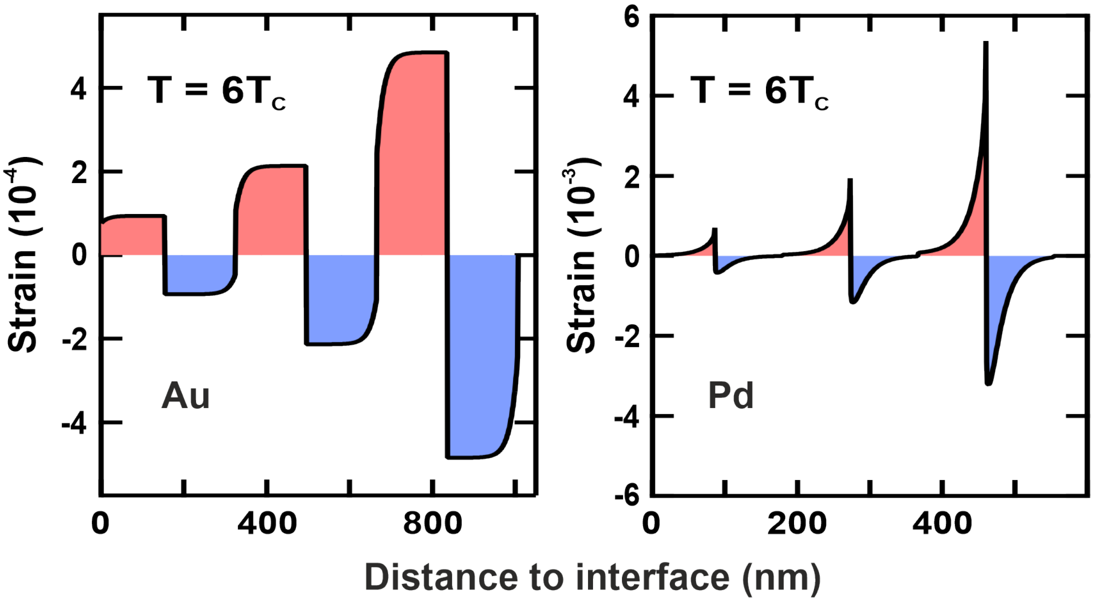

Figure 27: **Strain pulse results modeling.** This figure shows the result of the acoustic modeling. The left panel shows the strain pulse in the GaAs of the gold sample, the right panel on the palladium sample. $z = 0$ corresponds to the interface between the metal and the substrate.

The general shape of the pulse follows the scheme described in the previous section. It consists of a bipolar pulse, which is repeated with decreasing amplitude. The amplitude reduction is determined by the acoustic interface reflectivity.

The shape of the bipolar pulses is nearly rectangular, mirroring the homogeneous spatial excitation of the gold film. Only the edges at the beginning and at the end of the bipolar pulse are smoothed, which is a signature of the time dependent energy exchange between the electronic and lattice subsystem.

It should be noted, that the differences in the diffraction patterns between the optimal results for the different coupling times are rather small stressing the importance of the high dynamic range of the measurement as well as the use of a scalar metric like the MAPE to add up all the small deviations between the measured and calculated patterns. By just looking at the diffracted intensity for single time steps, it would not be possible to differentiate adequately.

From the obtained maximum strain, the stress after equilibration in the gold can be found to be $\sigma_\infty = 0.21$ GPa. This corresponds to an overall temperature rise of $T_\infty = 28.4$ K. According to Sokolowski-Tinten et al. one would expect a coupling time of around 2.75 ps for this temperature rise [122].

Additional two temperature model calculations were performed to compare them to the simple assumption of an exponential time constant. For that, an excited electron distribution with a spatially constant temperature at $T = 0$ was assumed as the initial excitation. Given this, equations 36 were solved numerically. Due to the spatially constant electron temperature, the gradient vanishes and no further transport happens.

The system reaches a final temperature rise of 28.4 K as in the experiment for an initial electron temperature of $T_e(0) = 1485\,\mathrm{K}$. The temperature development of the two subsystems is shown in the left part of figure 28. As can be seen, the electron temperature decreases fast, while the lattice heats moderately. This is a sign of the higher specific heat of the the lattice. After ≈ 10 ps, both systems have reached thermal equilibrium.

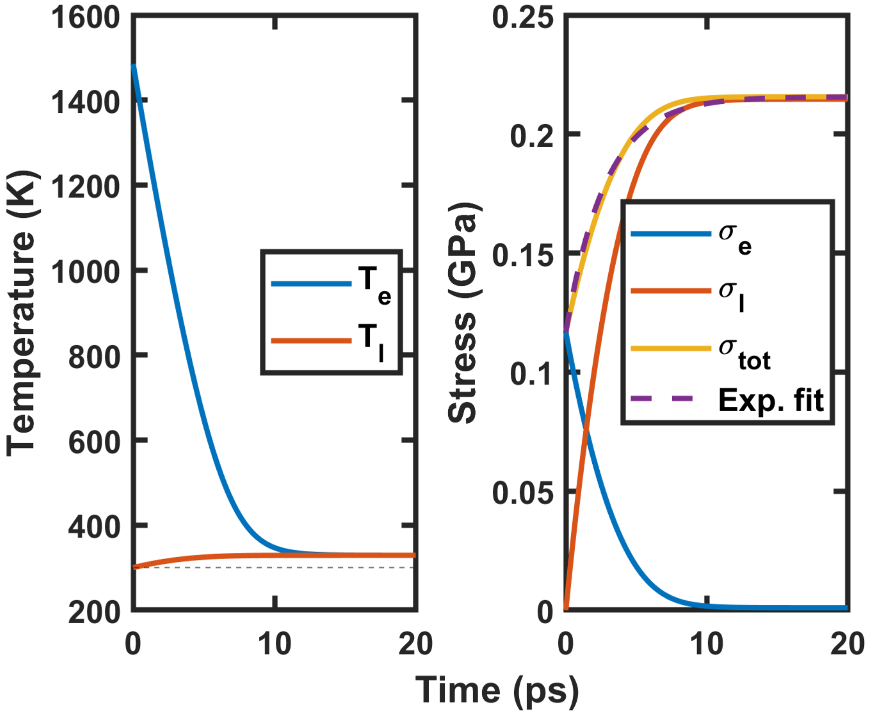

Figure 28: **Two temperature model calculations for the excited gold film.** The left graph shows the evolution of the subsystem temperatures after optical excitation of the electronic system of the gold film. Thermal equilibrium with a temperature rise of 28.4 K is reached after approximately 10 ps. The right graph shows the evolution of the electronic, thermal and total stress calculated from the temperatures. The purple dashed line is an exponential fit to the total stress corresponding to the Nicoul model.

From the temperature evolution, the electronic, thermal and total stress were calculated by integrating equation 37. The result is plotted on the right side of figure 28. Initially, there is only electronic stress, since the lattice is still at room temperature. During the energy transfer the electronic stress decreases and the phononic stress increases. Since the lattice Grüneisen coefficient is twice the electronic one, the overall stress increases up to twice the initial stress at time zero.

The purple dashed line is an exponential fit to the total stress, which corresponds to the model by Nicoul. It yields a coupling time of $\tau = (2.76 \pm 0.03)\,\mathrm{ps}$, which is lower than the optimal result obtained for our experiments but still within the experimental uncertainty. As can bee seen, there are deviations between the TTM result and the exponential fit. However, these deviations are small.

Accordingly, the deviations in the diffraction patterns calculated from this result are also small. The MAPE is shown as a red cross in figure 26 and is close to the MAPE at the respective time constants using the Nicoul model. However, it is slightly larger than the optimal MAPE value at 3.5 ps.

Various reasons are possible for that. Sokolowski-Tinten et al. have observed that the time constants obtained by a fit to the TTM are normally smaller than the experimentally observed results at weak excitations below $T_\infty = 50\,\mathrm{K}$ as in this case [122]. This might hint to a weak temperature dependence of the electron-phonon coupling parameter G.

Chase et al. have used ultrafast electron diffraction to observe the diffuse scattering of a thin gold film after laser excitation [18]. They found, that the phonon system is not in thermal equilibrium in the first picoseconds after excitation. This might also effect the average coupling time determined in this work.

For the low fluence measurement the pump induced intensity changes are comparably small as are the effects of varying the electron-phonon coupling time. Hence, an analysis of the optimal coupling time as for the high fluence was not tried. Therefore, the procedure was altered as follows: An optimization of equation 39 to the experimental data with the maximum strain as the only free parameter was performed. For every value of the strain the temperature rise in the gold film was calculated and the corresponding coupling time was determined by a fit to a TTM calculation. The best result was obtained for $\hat{\eta}_{\mathrm{GaAs}} = 5.3 \times 10^{-5}$, which corresponds to a temperature rise of 3.1 K and a coupling time of 1.5 ps.

Figure 29 shows the comparison of the time dependent rocking curves in a 2D false color representation. The first two columns of the figure show the results for gold. In the upper panel the experimental results, which were already presented in figure 21, are shown. The left image shows the lower fluence, the right one the higher fluence. The lower panel graphs show the best modeling result for both measurements.

Using the best fit value and comparing the result in figure 29 shows that the experimental data are in good agreement with the results of the simulation. This is further demonstrated in the comparison of single rocking curves. Figure 30 shows the rocking curves for different multiples of the characteristic time $T_{\mathrm{c}} = 35\,\mathrm{ps}$ and both fluences in the two left hand side columns. Again, it is visible that the results of the modeling fit the experimental data well. Especially the position and the intensity of the side maxima for different delays are reproduced nicely by the model.

The best approximation to the experimental data is achieved using $t_{\mathrm{GaAs}} = 170\,\mathrm{nm}$. This result cannot be directly compared to the experimental value, because the exact sound velocity of the gold film is unknown. Nevertheless, we can estimate it using equation 35 with the result for t_{GaAs} and the metal film thickness $t_{\mathrm{M}} = 120\,\mathrm{nm}$, measured by atomic force microscopy, to be $c_{\mathrm{M}} = (3380 \pm 80)\,\frac{\mathrm{m}}{\mathrm{s}}$. This is in reasonable agreement with the literature value of $3441\,\frac{\mathrm{m}}{\mathrm{s}}$ for (111) oriented gold (calculated from elastic constants taken from [80]). This finding is supported by static X-ray diffraction measurements yielding that our film is preferably (111) oriented (see appendix A).

The optimal values for the maximum strain are $\hat{\eta}_{\mathrm{GaAs}} = 5.3 \times 10^{-5}$ and $\hat{\eta}_{\mathrm{GaAs}} = 4.9 \times 10^{-4}$ for the low and high fluence experiment. This corresponds to an absorbed fluence of $0.034\,\frac{\mathrm{mJ}}{\mathrm{cm}^2}$ and $0.31\,\frac{\mathrm{mJ}}{\mathrm{cm}^2}$. These values are rather small, because the reflectivity for s-polarized 800 nm light is close to 1 at an angle of incidence of 36° ($R = 0.981$ [53]).

To conclude, our measurements can be well reproduced in the frame of the model developed by Nicoul et al. [83]. The crucial point for the understanding of the picosecond acoustics of the excited gold film is the interplay of electron-phonon coupling and transport: While electron-phonon coupling is comparably slow in gold, efficient transport leads to a homogeneous spatial distribution of the deposited energy. This is essential for the overall shape of the acoustic pulse, which is consequently governed by rectangular bipolar pulses. Due to the high dynamic range, the experiment is even sensitive to the electron-phonon coupling time, which affects the shape of the pulse due to the difference in electron and lattice Grüneisen coefficients.

The material parameters obtained by the optimization are in reasonable agreement to the literature. A direct comparison of the the phenomenological model by Nicoul et al. to two temperature model calculations has shown, that the deviations are small, even though the two temperature model yields a slightly lower coupling time for the given temperature rise.

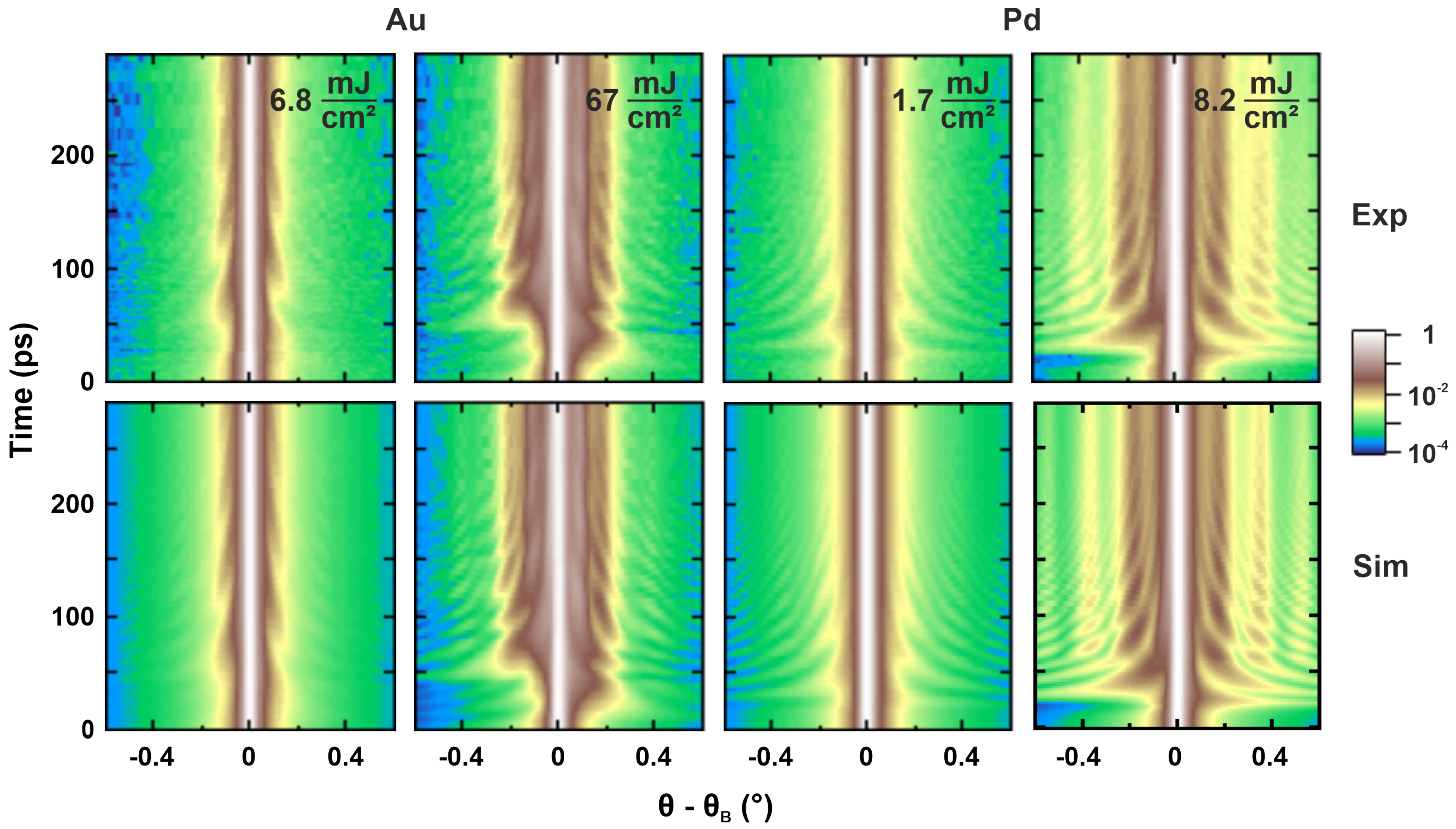

Figure 29: **2D false color plots of the experiment and simulation results for gold and palladium.** The upper panel shows the experimental results for two different fluences and two different metal films (gold and palladium). The two graphs on the left hand side depict gold results, the two ones on the right hand side palladium. The respective fluence is given in the graphs. The lower panel shows the simulation result in best agreement with the experiment.

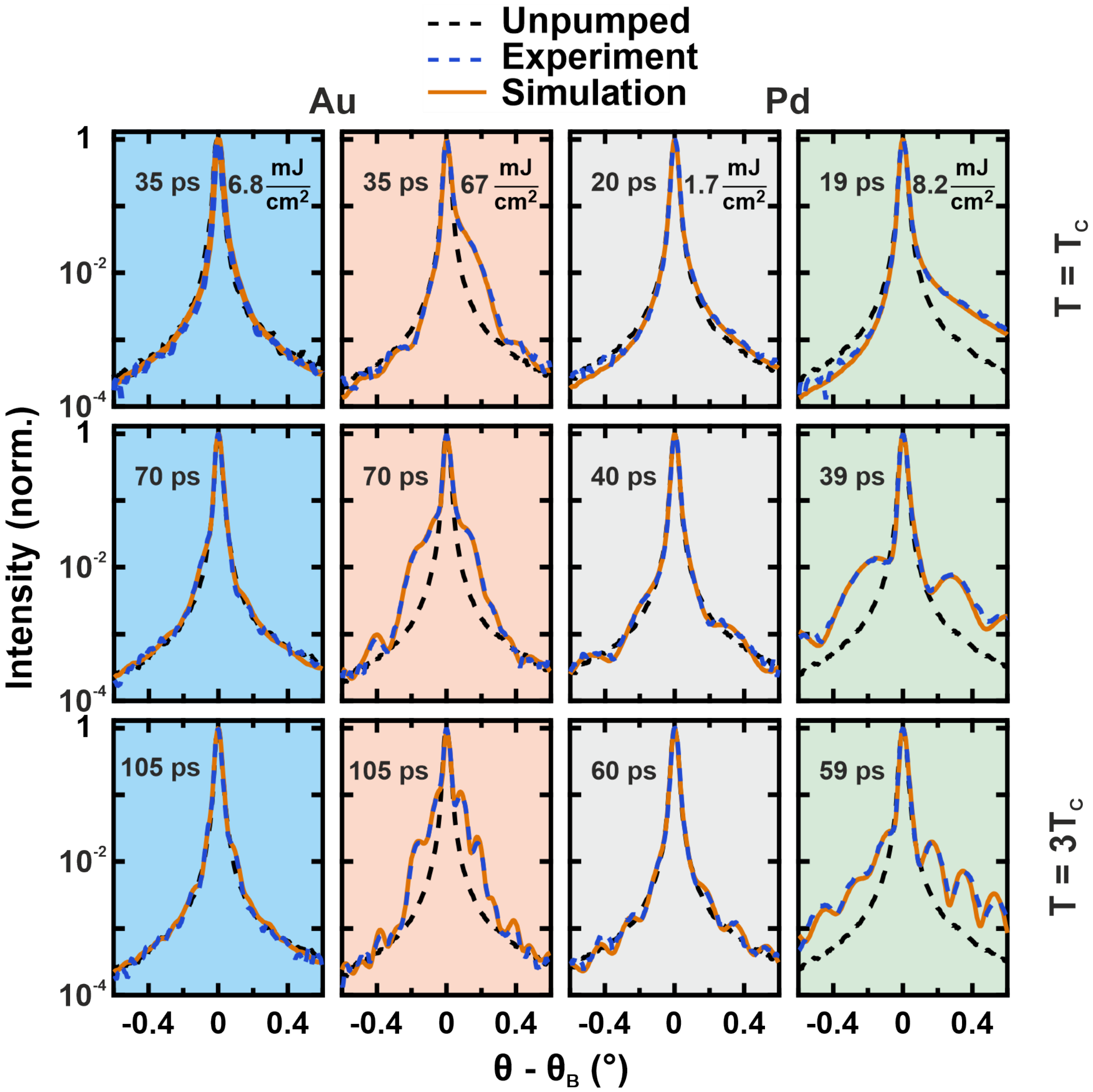

Figure 30: **Single rocking curve comparison.** This figure shows the comparison of the experimental results for gold (column 1 and 2) and palladium (column 3 and 4) for the two different fluences and various time delays to the simulated diffraction patterns using the presented models for the emitted picosecond acoustic waves. The specific times and fluences are given in the graphs. It should be stressed, that the agreement ranges over the high dynamic range of our setup.

6.5.2 Palladium

For modeling the experimental results on the Pd/GaAs sample, TTM calculations were not performed for two reasons. On the one hand, the electronic Grüneisen parameter of palladium is unknown and hence the temporal evolution of the total stress cannot be deduced from the temperatures. On the other hand, Marius Milnikel has performed ultrafast electron diffraction experiments measuring the Debye-Waller effect in an optically excited palladium film (see appendix B) [77]. He found, that the electron-phonon coupling time in palladium is around half a picosecond, much faster than the characteristic acoustic time scale T_c. Hence, hot electrons start to exchange energy with the lattice very fast and thermal equilibrium is rapidly reached (quasi-instantaneously). On the relevant acoustic timescales, the two systems can therefore be assumed to be in thermal equilibrium. Hence, it is not necessary to model the temporal evolution of the temperatures in the palladium film to describe the acoustics.

Thomsen et al. have introduced a model to calculate the acoustics for an optically excited sample in the limit that only one contribution to the stress, namely the thermoelastic exists, which means that the system can be described by a single temperature [129]. This model is also applicable, if the equilibration of the electronic and lattice subsystem is fast and, accordingly, both can be assumed to have the same temperature.

In the model, heat diffusion described by the thermal diffusivity D is the only transport mechanism taken into account. To begin with, an initially exponential excitation profile with the absorption length of the respective material as the decay constant is assumed. Transport by hot electrons faster than the acoustic timescales could alter this profile and lead to an effectively larger deposition depth and also deviations from the exponential profile, which is not included in the model.

The transient strain wave shape in such a system is given by

$$\eta(z,t) = \frac{3F_\mathrm{abs}\beta B}{\xi c^2 \rho C_V} F(z-ct) \tag{41}$$

with the absorbed fluence F_abs, the linear thermal expansion coefficient β, the bulk modulus B, the absorption length ξ, the sound velocity c, the density ρ and the specific heat per unit volume C_V. The function $F(z-ct)$ describes the shape of the bipolar pulse. It can be calculated using

$$F(z-ct) = \begin{cases} -\frac{1}{2}e^{-(z-ct)/\xi} - \frac{1}{2}\int_{0+}^{\infty} dt' \int_0^{\infty} dz' \frac{\partial\Theta(z',t')}{\partial t'} \delta(z'-z+c(t-t')) \\ \frac{1}{2}e^{-(z-ct)/\xi} - \frac{1}{2}\int_{0+}^{\infty} dt' \int_0^{\infty} dz' \frac{\partial\Theta(z',t')}{\partial t'} \\ \qquad\qquad \times[\delta(z'-z+c(t-t')) - \delta(z'+z-c(t-t'))], \end{cases} \tag{42}$$

where the first equation holds for $z > ct$ and the second one for $z < ct$. The function $\Theta(z,t)$ describes the energy transport due to diffusion during the emission of the strain wave:

$$\Theta(z,t) = \int_{-\infty}^{\infty} dz' (4\pi D t)^{-1/2} e^{(-z-z')^2/4Dt} e^{-|z'|/\xi}. \tag{43}$$

The shape of the pulse is determined by the ratio $D/c\xi$. Figure 31 shows the bipolar pulse with and without diffusion. As can be seen, the pulse consists of two exponential decay profiles mirroring the absorption of the light, if diffusion is not taken into account. Transport during the acoustic emission process leads to an asymmetry between compression and expansion. This broadens the compression part of the pulse while reducing its maximum.

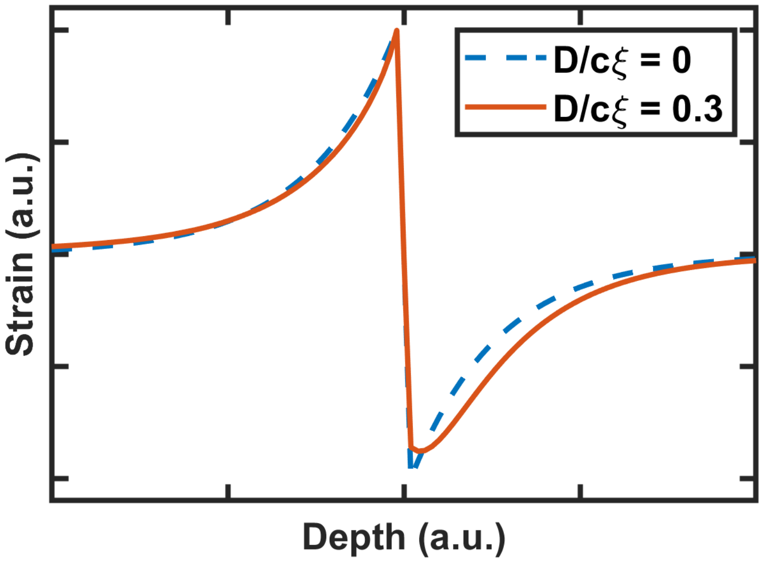

Figure 31: **Comparison of a strain pulse with and without diffusion.** This figure shows the result of the Thomsen model [129] with and without diffusion. The diffraction results of the palladium experiment can be explained better, if thermal diffusion is taken into account.

Even though electron-phonon coupling is fast compared to the acoustic timescales, it cannot be excluded that transport of hot electrons leads to changes of the deposition profile before the subsystems have reached thermal equilibrium. To account for that ξ is interpreted as an effective deposition depth and treated as a free parameter in the following. The optical absorption depth is $\xi_{\text{opt}} = 12.5\,\text{nm}$ [53], but for the modeling ξ is varied in discrete steps of 2.5 nm from 7.5 – 30 nm.

This model is now applied to the palladium heterostructure under examination. The relevant material parameters are given in table 2. The diffusion constant is related to the thermal conductivity κ via $D = \frac{\kappa}{C_V}$:

Table 2: **Parameters for the acoustic simulation of the excited palladium film.** The metal thickness t_{M} was measured using atomic force microscopy. The thickness inside the GaAs t_{GaAs} is a free parameter. The speed of sound in the metal c_{M}, the interface reflectivity R and the characteristic time T_{c} are calculated from that values using equations 35 and 24. All other parameters are taken from the literature. The respective references are given in the table.

t_{M}	88 nm
t_{GaAs}	93 nm
c_{M}	$4500\,\frac{\text{m}}{\text{s}}$
R	0.36
T_{c}	20 ps
c^{100}_{GaAs}	$4730\,\frac{\text{m}}{\text{s}}$ [16]
ρ	$12.02\,\frac{\text{g}}{\text{m}^3}$ [76]
B	$1.81 \times 10^{11}\,\text{Pa}$ [55]
β	$1.18 \times 10^{-5}\,\frac{1}{\text{K}}$ [68]
C_V	$2.95 \times 10^{6}\,\frac{\text{J}}{\text{m}^3\,\text{K}}$ [68]
ξ_{opt}	12.5 nm [53]
κ	$73\,\frac{\text{W}}{\text{m}\,\text{K}}$ [48]
G	$1.4 \times 10^{18}\,\frac{\text{W}}{\text{m}^3\,\text{K}}$ [77]

Given these parameters, equations 41 – 43 can be solved numerically. Again, the free parameters in this model are the thickness of a single pulse in the substrate t_{GaAs} and the maximum strain in the GaAs $\hat{\eta}_{\text{GaAs}}$. These parameters are optimized until the minimum MAPE is reached. The result is shown in figure 32. The MAPE is normalized in this case to allow for the plotting of the results for the low and high fluence case in one graph.

It is clearly visible that the optimal effective deposition depth $\xi = 17.5^{+7.5}_{-2.5}$ nm for the high fluence experiment is larger than the optical absorption depth, while the low fluence measurement can be described best using $\xi_{\mathrm{opt}} \approx \xi = 12.5^{+5}_{-2.5}$ nm. This indicates that for the high fluence some transport of excited electrons leads to a broadening of the energy deposition profile in comparison to the absorption profile of the laser pulse.

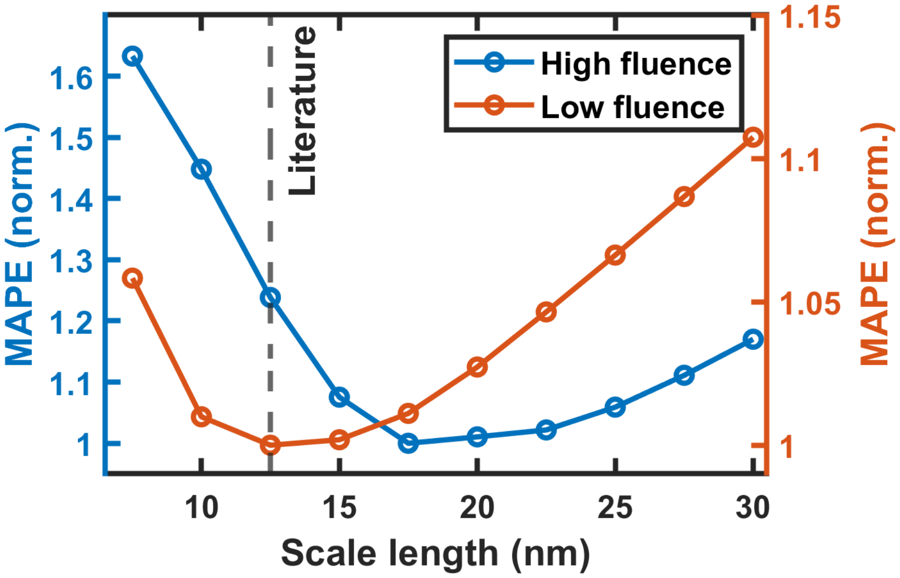

Figure 32: **Mean average percentage error for variation of scale length in palladium.** The two curves show the best achievable MAPE between measured and calculated diffraction patterns for the high (blue) and low fluence (orange) results. The solid lines are guides to the eye. The dashed line shows the literature value for the absorption length of the light in palladium (see table 2).

The resulting strain in the substrate $\eta(z,t)$ for the high fluence measurement for $T = 6T_{\mathrm{c}}$ is depicted in the right part of figure 27. The leading front has only reached a depth of 570 nm, because the characteristic time of $T_{\mathrm{c}} = 20$ ps is shorter than for the gold sample. As can be seen, the acoustic pulse shape is determined by the shallower energy distribution profile in contrast to gold. Additionally, diffusion effects the biexponential shape originating in the ratio $D/c\xi = 0.32$ for the given parameters.

From the result of the acoustic modeling the diffracted X-ray intensity is calculated. The comparison of the 2D false color plots to the experimental data is shown in the two right hand side columns of figure 29. A direct comparison of the rocking curves for different multiples of the characteristic time $T_{\mathrm{c}} = 20$ ps is shown in figure 30. Best agreement to the experimental data is given for $t_{\mathrm{GaAs}} = 93$ nm and a maximum strain of $\hat{\eta}_{\mathrm{GaAs}} = 1.1 \times 10^{-3}$ and $\hat{\eta}_{\mathrm{GaAs}} = 5.4 \times 10^{-3}$ for the low and high fluence experiment, respectively. This corresponds to a maximum temperature rise of $T_\infty = 315$ K and $T_\infty = 64$ K and an absorbed fluence of $F_{\mathrm{abs}} = 0.29\,\frac{\mathrm{mJ}}{\mathrm{cm}^2}$ and $F_{\mathrm{abs}} = 2.0\,\frac{\mathrm{mJ}}{\mathrm{cm}^2}$, which suits the theoretical surface reflectivity of $R = 0.81$ for 800 nm at an angle of incidence of 36° within the experimental uncertainties.

As for gold we cannot directly compare the result for the thickness with experimental parameters, because the exact sound velocity of the palladium film is unknown due to the unknown structure. Nevertheless, we can use the obtained value and the measured palladium film thickness of t_{M} to determine the sound velocity to be $c_{\mathrm{M}} = (4500 \pm 100)\,\frac{\mathrm{m}}{\mathrm{s}}$. This is in good agreement with the range of sound velocities for the different palladium crystal directions calculated by the elastic constants given in the literature $c = [4350, 4905]\,\frac{\mathrm{m}}{\mathrm{s}}$ [93].

Using this results one can compare the experimental data to the calculated rocking curves in figures 29 and 30. Again, the agreement between both is very good, supporting the given model for the acoustic dynamics.

To check for the relevance of including diffusion effects, we also tried to reproduce the experimental data while setting the thermal conductivity of palladium to 0. It turned out that by omitting diffusion, the agreement between theory and experiment worsens. This is shown in figure 33 for an exemplary time delay. The position and intensity of the side maxima is clearly reproduced worse, if diffusion is not taken into account.

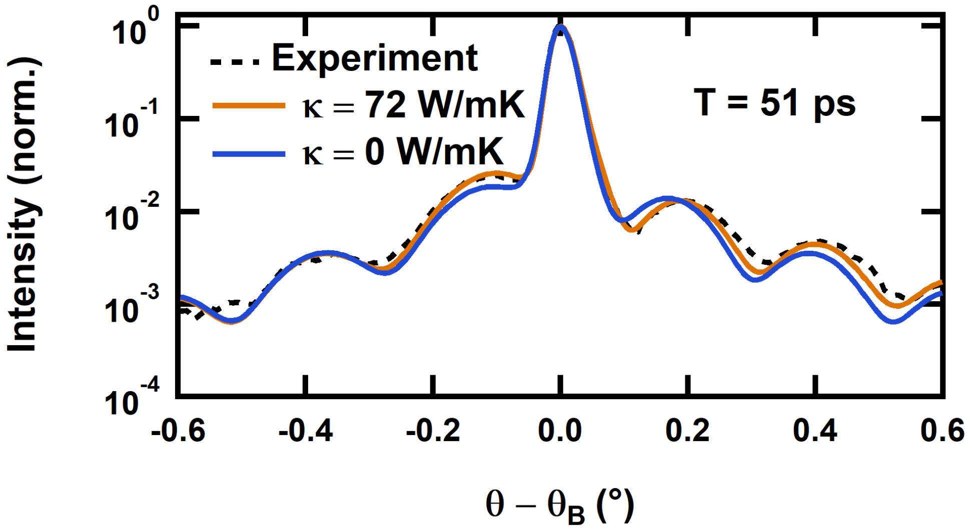

Figure 33: **Effect of including diffusion for the simulation of the palladium response.** This figure shows the best fit to the experimental data for the previously discussed model and compares it to the simulation, where the effect of thermal diffusion is not taken into account. This is done by setting the thermal conductivity $\kappa = 0$.

All in all, it can be said that the strong electron-phonon coupling in palladium is mostly responsible for the shape of the induced acoustic pulse. However, for high excitation fluences hot electron transport affects the excitation profile faster than acoustic wave emission and hence also the shape of the pulse. Subsequently, transport via thermal diffusion alters the profile and leads to an asymmetry between the compressive and expansive part of the bipolar pulse.

6.5.3 Fluence Dependence

As shown in the previous paragraphs, our models allow for the quantitative description of the acoustic response of both material systems. Additionally, we performed fluence dependent measurements to investigate, whether the purely linear models are able to describe the dynamics over the relevant range of fluences. Two kinds of linearities have to be considered: Acoustic and optical linearities.

Figure 34 shows the comparison of unpumped, experimental and simulated rocking curves for both materials and five different fluences. The experiments were done at fixed delay times. The fluence was varied from 3.8 $\frac{\mathrm{mJ}}{\mathrm{cm}^2}$ to 67 $\frac{\mathrm{mJ}}{\mathrm{cm}^2}$ for gold and from 1.7 $\frac{\mathrm{mJ}}{\mathrm{cm}^2}$ to 8.6 $\frac{\mathrm{mJ}}{\mathrm{cm}^2}$ for palladium.

For every fluence, the optimal value of the maximum strain in GaAs was searched to find the best agreement to the experimental data. As has been discussed, the electron-phonon coupling time for gold and the scale length for palladium are fluence dependent. For gold, this was taken into account by determining the coupling time based on a TTM calculation for every single peak strain in the optimization process. For palladium, the scale length was varied linearly between the value for the low fluence experiment (12.5 nm) and for the high fluence experiment (17.5 nm).

For both materials, the agreement between experimental and simulated curves is good over the whole fluence range. By only optimizing the peak strain, we are thus able to reproduce the measurements. This shows, that a purely linear acoustic model is capable of describing the experimental data in the given fluence range and hence, nonlinear acoustic effects do not have to be taken into account.

To also look for optical non-linearities, the peak strain as a function of the experimental fluence for gold is shown in figure 35. The dashed line is a linear fit through the origin to the data. Within the experimental error, all data points are in agreement with the linear fit and hence we see no nonlinear behavior. The orange crosses show the results of the transient experiments for comparison.

For palladium, the peak strain is not a good measure for optical linearity. As has been shown, fluence dependent electronic transport has to be taken into account to explain the experimental results and hence the scale length changes as a function of fluence. If the fluence is for example doubled and also twice the energy is deposited, this will not lead to a doubling of the peak strain. Due to the larger scale length the energy is distributed over a wider range and the peak strain is thus smaller. Therefore, the average strain of a bipolar pulse, which is defined as:

$$\bar{\eta} = \frac{1}{d} \int_0^d |\eta(z)| dz, \tag{44}$$

with the thickness of the bipolar pulse d is shown for palladium in figure 35. The dashed line is a linear fit to the data through the origin. Within the experimental uncertainty the data points follow a linear dependence.

Thus, we can conclude that both material systems show a purely linear behavior in terms of acoustic and optical linearity over the investigated fluence range.

6.6 Comparison and Conclusion

The analysis of the acoustic response of the two samples has shown some distinct differences, explaining the deviations of the time resolved X-ray diffraction data for gold and palladium. In both cases, the interplay of electron-phonon coupling and transport determines the picosecond acoustic response upon optical excitation. While electron-phonon coupling is relatively slow and electronic transport is very effective in gold, it is quite the opposite for palladium. This results in very different shapes of the acoustic pulses.

As figure 27 shows, the dominant form of the strain pulse is close to a rectangle for gold and an exponential profile for palladium, each reflecting the spatiotemporal dependence of energy deposition upon optical excitation. Connected to the form of the pulse, the peak strain also differs by a factor of two for a comparable amount of deposited energy. This originates in the confinement of the energy in a much smaller volume for palladium. These differences manifest in the transient diffraction signals.

A linear acoustic model of the strain wave emission and propagation is able to reproduce the measured transient changes of the diffracted X-ray intensity over four orders of magnitude exploiting the high dynamic range of our setup. With just two free parameters, the experimental data can be described quantitatively over an extended range of fluences.

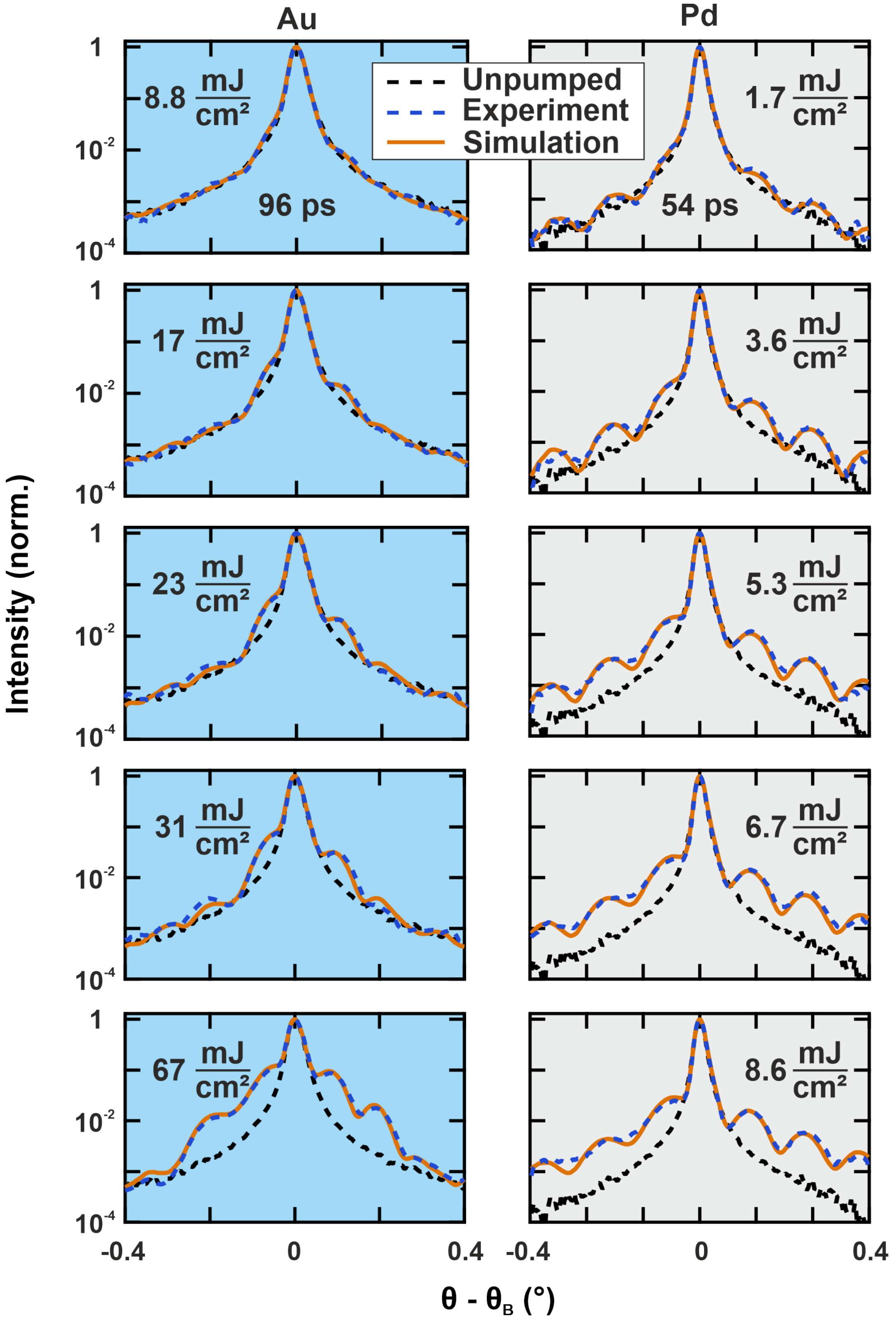

Figure 34: **Fluence dependent experiments and modeling.** This figure shows the comparison of the fluence dependent experimental diffraction patterns to the best simulation fit, based on the presented models for gold (left column) and palladium (right column) for a fixed time delay of 96 ps and 54 ps, respectively.

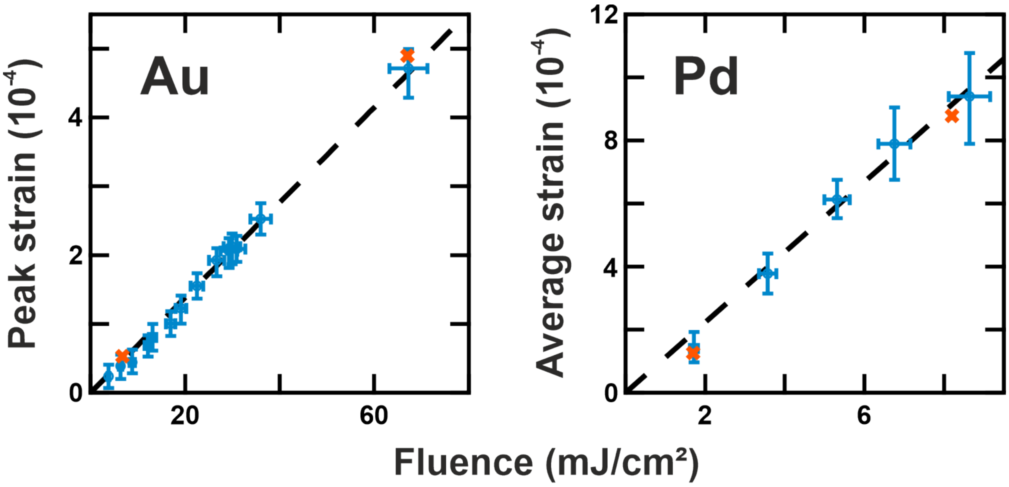

Figure 35: **Modeling strain versus experimental fluence.** This figure shows the strain which yields the best fit to the experimental data using the previously discussed models as a function of the experimental fluence. The dashed lines are linear fits through the origin. The orange crosses show the data of the time resolved experiments.

7 Strain Retrieval

As described in chapter 6, the modeling approach serves well in understanding the acoustics upon ultrafast optical excitation for some systems. Even though it turned out to be very effective in this case as in various examples in the literature, it suffers from a number of issues.

- Modeling of the microscopic processes can become very complex. In general, the problem can get more complicated than it was for the two metals. For example, in our cases a perfect interface was assumed, which is not necessarily true.

- Simple phenomenological models based on the two temperature model could be exploited in this case. However, the TTM is not always applicable. In fact, it might even fail for simple metals [135] and the situation could become worse for more complex materials.

- The geometrical structure of the system could also be much more complex for example with multiple layers of different materials including nanoparticles or 2D materials. Moreover, if the penetration depth of the pump light is larger than the layer thickness, excitation takes place in multiple layers and interlayer energy transport becomes important.

- The relevant parameters could be found in the literature for both materials. This is not always a case. E.g. for palladium a full TTM modeling was not possible due to the missing electronic Grüneisen coefficient.

- Such an approach can be very time consuming, because assumptions on the microscopic processes have to be made, the corresponding diffraction has to be calculated and the assumptions have to be judged on the basis of the agreement between experiment and simulation. This is an iterative process, until a reasonable model is found.

For all these reasons, a more direct derivation of the acoustic pulse from the experimental data would be desirable. To further improve the analysis of picosecond acoustic experiments and extend the method to more complex and non-ideal situations, we aim to develop a new method to directly extract the acoustic response from the transient diffraction data, which will be called "direct strain retrieval".

Our method does not require any physical assumptions. Only some very fundamental boundary conditions originating in the sample geometry are taken into account to reduce the solution space of the problem.

This section is structured as follows. Firstly, the general problem is discussed and the idea for the solution is presented. Secondly, the retrieval algorithm is described in detail. Thirdly, the optimal hyperparameters for the retrieval are investigated and fourthly, the algorithm is applied to the gold and palladium measurements already discussed in the previous chapter and the results are compared to the modeled acoustics. In the end, the performance, its potentials and limitations and ways for possible improvements are discussed.

7.1 Phase Problem and General Idea

The underlying problem is a very general issue in diffraction experiments: The phase problem. A diffracted wave's field strength at a position $\vec{r}$ can be described by its amplitude $\hat{E}$ and phase ϕ:

$$E(\vec{r}) = \hat{E}(\vec{r}) \exp(i\phi(\vec{r})). \tag{45}$$

However, these quantities are seldom measured directly. Most commonly, the diffracted intensity is measured. Since the intensity is proportional to the absolute square of the field strength,

$$I(\vec{r}) = |E(\vec{r})|^2 = \hat{E}(\vec{r})^2, \tag{46}$$

it is no function of the phase anymore and hence the phase information of the wave is lost during the measurement process. Accordingly, it is difficult to retrieve the full wave and with that the information about the specimen. Translated to the field of ultrafast acoustics, this means that it is straight forward to calculate the angle and time resolved X-ray intensity for a given strain distribution $\eta(z, t)$ using dynamical X-ray diffraction theory (see chapter 4.1.3), but it is challenging to solve the inverse problem (see figure 36).

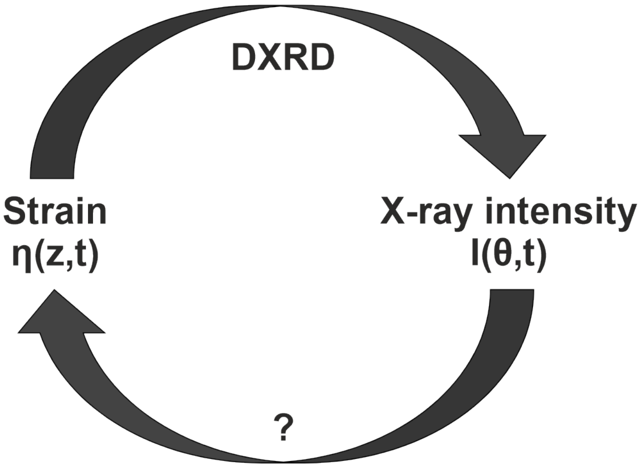

Figure 36: **Phase problem in ultrafast acoustics.** The phase problem translated to ultrafast acoustics is that the calculation of the X-ray intensity is easy, if the space- and time-dependent strain distribution is known. However, the calculation of the strain distribution from the time-resolved diffraction data is difficult.

Different methods have been developed to solve the phase problem. In coherent diffractive imaging phase retrieval algorithms like the Gerchberg-Saxon algorithm are very successful in reconstructing nanostructures from diffraction patterns [35, 90]. They require the probed object to be confined to a small region. Initially, random phases are guessed and by iterative application of the Fourier transform and its inverse and exploiting the fact, that the exact amplitudes are known, the phases can be retrieved. This has already been successfully applied for retrieving the static strain in a thin film [131]. However, the constraints mentioned above are not fulfilled in our case. The strain wave travels into the substrate and hence is not confined. Additionally, the method exploits the invertibility of the Fourier transform, but the diffraction pattern is only given by the Fourier transform in the kinematical limit. Dynamical diffraction theory is not invertible and, therefore, these algorithms are typically not applicable.

Another important method is Rietveld refinement, which was introduced to reconstruct the structure of polycrystalline samples from a diffractogram [98]. It uses a least-square minimization of the deviation from a calculated to a measured pattern and optimizes parameters like peak position and peak intensity. Our problem differs from these in some points. First, Rietveld methods are normally applied to one dimensional data. Second, changes of the parameters alter the pattern in specific regions, namely around the attributed Bragg peak. In contrast, we are only looking at one Bragg peak in our experiment and changes to the parameters of the pulse do not only effect a confined region, but alter large parts of the 2D pattern. We therefore aim for a method, which takes this special prerequisites into account.

There are also methods for direct strain retrieval similar to our case discussed in the literature [32, 61]. However, these assume physical models for their retrieval, e.g. about the indirect scattering with phonons or the dielectric function of the material. Moreover, they even require special sample features such as a reflection inside the specimen. Ideally, the solution should not require any prerequisite assumptions.

In this chapter, a new method based on machine learning techniques is described. The basic idea is, that transient diffraction patterns are in fact images. Since deep neural networks have been proven superior to other methods in image analysis, it is convenient to try to use them for the analysis of time resolved diffraction from acoustic waves. Such a method would perfectly complement the modeling approach and would thus allow for a better analysis and understanding of picosecond acoustic experiments.

The crucial point for using deep neural networks to solve a problem is the availability of a sufficient amount of training data. The calculation of diffraction patterns from known strain distributions is easy. Thus, any desired number of training pairs can be created by randomly generating strain pulses and calculating corresponding diffraction patterns.

7.2 Pulse Parametrization and Sensitivity

A prerequisite for strain retrieval with deep neural networks is the parametrization of the acoustic pulse. A straightforward way to do so, would be to just take the strain amplitude $\eta_T(z)$ at a depth z for a fixed time delay T. Depending on the chosen spatial grid size, this leads to a few hundred parameters, if a time interval of $T = 100\,\mathrm{ps}$ is supposed to be covered. Additionally, it does not reflect the periodicity of the pulse train. Therefore, a parametrization using the Fourier expansion of the bipolar pulse, which deploys this periodicity is chosen in this work.

Imagine the strain distribution being a periodic repetition of the bipolar pulse. According to the theory of Fourier expansion a periodic function like this can be approximated by:

$$\eta(z) = \frac{C_0}{2} + \sum_{n=1}^{N} (C_n \cos(nk_1 z) + S_n \sin(nk_1 z)), \tag{47}$$

where n is an integer, N is the order of the expansion and C_n and S_n are the sine and cosine amplitudes, respectively. k_1 is the wave number of the fundamental component which is chosen to be:

$$k_1 = \frac{2\pi}{d}, \tag{48}$$

reflecting the periodicity of the pulse train. The amplitudes of the Fourier expansion which are also known as the Fourier coefficients can be calculated via:

$$\begin{aligned} C_n &= \frac{2}{d}\int_{-d/2}^{d/2} \eta(z)\cos(ik_1 z)dz, \\ S_n &= \frac{2}{d}\int_{-d/2}^{d/2} \eta(z)\sin(ik_1 z)dz. \end{aligned} \tag{49}$$

One obtains the full pulse train by multiplication with a suitable gating function G:

$$\eta_{\text{Train}}(z) = \eta(z)G(d,R). \tag{50}$$

This gating function is determined by the pulse thickness d and the interface reflectivity R and has the value R^{j-1} for the j^{th} bipolar pulse of the pulse train and 0 everywhere else. It reflects the creation mechanism of the back and forth reflection in the metal film.

Figure 37 shows the acoustic pulse train and the gating function G. Given that, the pulse train can be fully described by the set $\{d, R, S_i, C_i\}$. The quality of the reconstruction is determined by the number of Fourier coefficients taken into account. Therefore, it is desirable to retrieve as much coefficients as possible.

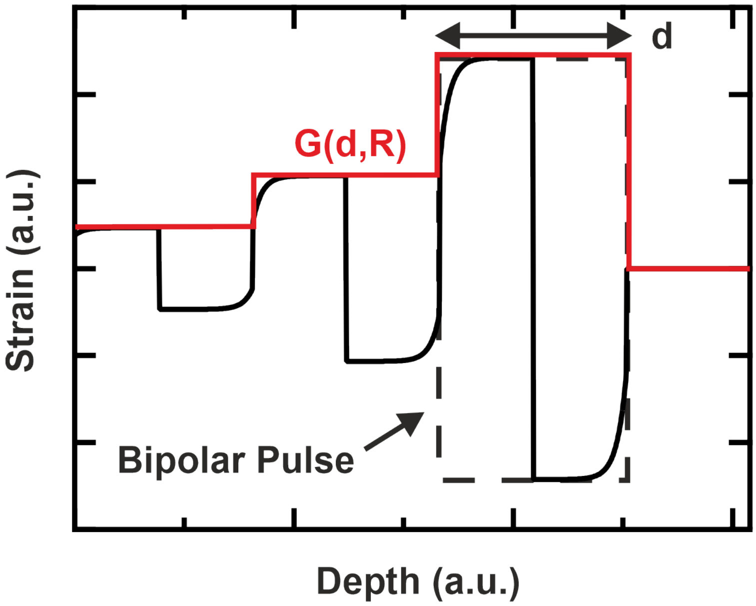

Figure 37: **Pulse train and gating function.** A pulse train emitted in our sample geometry can be parametrized by the Fourier expansion of a periodic repetition of the bipolar pulse and a suitable gating function shown in red.

The coefficients might vary over several orders of magnitude making it difficult to retrieve them. Therefore, the average strain of a bipolar pulse, which is defined by equation 44, is used to normalize the Fourier coefficients.

Altogether, the pulse is parametrized by the set $\{\bar{\eta}, d, R, S_i, C_i\}$. It should be stressed, that this approach does not make any assumptions about the physical processes of strain generation. It just reflects the spatial restrictions due to sample geometry.

To get a better understanding of the dependence of the Fourier coefficients on the pulse shape, we take a look at different typical examples. For this, four different pulse shapes closely connected to the two material systems under investigation are taken into account. These shapes are in a sense limiting cases for different temporal and spatial variations of stress:

I Rectangle - Result of a spatially homogeneous and timely constant stress, II Gold - Result of a spatially homogeneous and time dependent stress,

III Exponential - Result of spatially inhomogeneous and temporally constant stress (no transport after light absorption),

IV Palladium - Result of a spatially inhomogeneous and time dependent stress.

The four different shapes can be seen in the upper panel of figure 38. Moreover, the Fourier expansions of these bipolar pulses are shown for 5 and 20 sine coefficients together with 0 and 20 cosine coefficients. The values of the coefficients are plotted on the left hand side of the lower panel for the sine and on the right hand side for the cosine coefficients. The coefficients for every pulse are normalized to the lowest coefficient having the value -1 for comparison reasons.

As can be directly seen, the sine coefficients are dominant and have negative values. This reflects the general bipolar and thus point symmetric pulse shape and the fact that the first part is always positive followed by the negative strain part. Cosine coefficients are only necessary to describe the palladium pulse, because this is the only one with an asymmetry between expansion and compression. This is due to the fact, that the original stress is space and time dependent. Opposite to the sine coefficients, the cosines do not have a fixed sign. There are positive as well as negative values.

It can also be seen that the overall strength of the sine coefficients declines with the coefficient number. For the pulses III and IV the strongest coefficient is #2 and the decline is smooth.

Contrary, pulses I and II have their strongest coefficient at #1, but the decline is alternating. This means on the one hand, the even coefficients are equal to 0 for the perfect rectangular pulse and close to 0 for the gold pulse. The odd coefficients on the other hand are decaying smoothly. This can easily be understood taking the special form of the pulse into account: For getting a rectangular bipolar pulse, the respective Fourier coefficients have to be symmetric with respect to the axis at 1/4 and 3/4 of the thickness. This requires a maximum or a minimum at this positions, which is only fulfilled for the odd Fourier components.

As has been said before, only the asymmetric pulse contains cosine components. The values of these components differ from the sine ones in two aspects: First, they are about an order of magnitude smaller than the sine coefficients. This is immediately clear, since the asymmetry of the pulse is weak. Second, the cosine coefficients may also take positive values.

As one expects, pulse shapes can be reconstructed the better the more Fourier coefficients are taken into account. This is especially visible at sharp boundaries, since high frequency components are required to create such features in real space. Accordingly, the pulse generated by 20 sine coefficients is already much closer to the original pulse than the one constructed by 5 components. However, even with such a low number of coefficients as 5, the general shape of the bipolar pulse (rectangular or exponential) can be distinguished.

Taking a closer look at the yellow and purple curve in graph IV of figure 38 one can see that the differences of the real space strain shape are small, even if a high number of cosine coefficients is taken into account. This is a consequence of their comparable small amplitude. However, as has been shown in chapter 6, we are sensitive to the asymmetry of the pulse, because thermal diffusion has to be taken into account to give the best description of the experimental results on the palladium sample.

All these observations regarding the Fourier components of the bipolar pulse lead to the question, how much information about the Fourier coefficients is included in our time-resolved X-ray diffraction data. A first rough estimation can be done by taking a look at

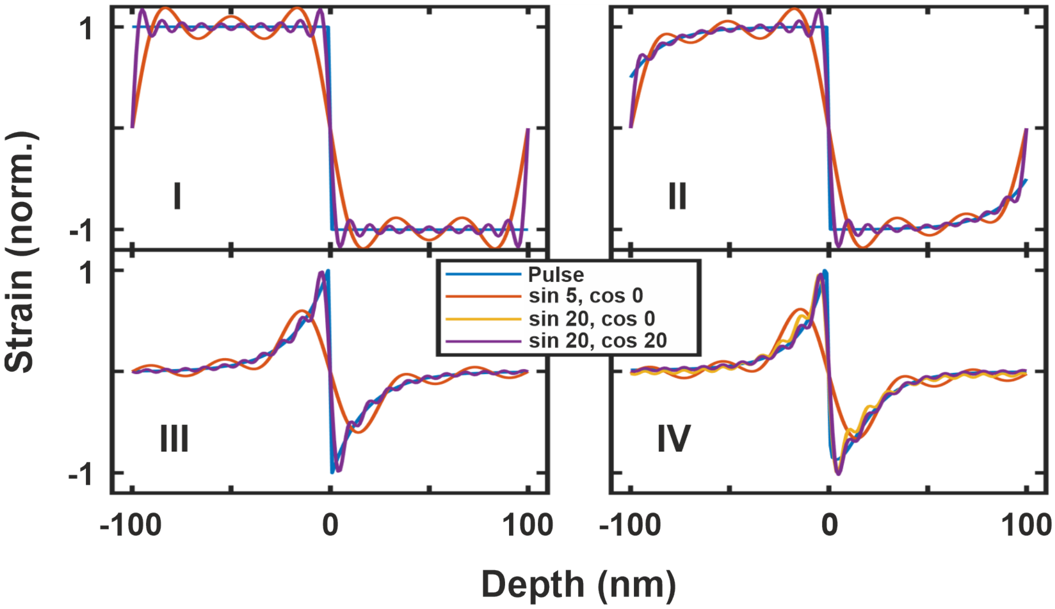

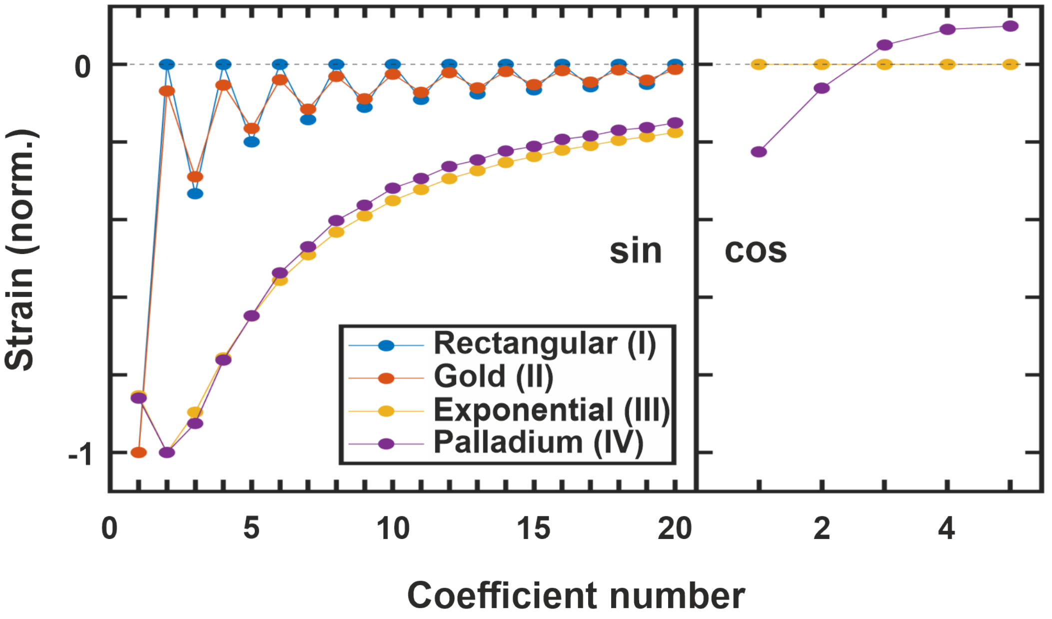

Figure 38: **Fourier series and coefficients of the different bipolar pulses.** This figure compares the Fourier series expansion and the amplitude of the coefficients for different bipolar pulse shapes. The upper figures show 4 different bipolar pulses - I: Rectangular, II: Gold, III: Exponential and IV: Palladium - together with their Fourier expansions including 5 sine and 0 cosine, 20 sine and 0 cosine and 20 sine and cosine coefficients (the yellow curves are hidden behind the purple curves for the symmetric pulses). The lower figure shows the amplitudes of the Fourier coefficients for the pulse shapes mentioned above. On the left hand side for the sine and on the right hand side for the cosine coefficients. The coefficients are normalized such that the dominant coefficient has an amplitude of -1.

the relation between the angle and the phonon wave vector derived from equation 28. A phonon mode with wavelength λ leads to a diffraction signal at an angular deviation of

$$\Delta\theta = \frac{\lambda_X}{2\cos(\theta_B)}\frac{1}{\lambda} \tag{51}$$

apart from the main peak. To get a first estimate for the sensitivity to Fourier coefficients, one can insert the pulse thickness d instead of a phonon wavelength and divide this through the experimental accessible angular range ($\Delta\theta_{\text{exp}} \approx 0.6°$). Using the material specific values and the experimental parameters of the two material systems under investigation yields:

$$N = \frac{\Delta\theta}{\Delta\theta_{\text{exp}}} \approx \begin{cases} 6 & \text{(Au)}, \\ 3 & \text{(Pd)}. \end{cases} \tag{52}$$

Moreover, the intensity of the diffraction signal reduces with increasing angular distance to the Bragg peak. This stresses the importance of the high dynamic range of our experiments for the retrieval of as much coefficients as possible. Furthermore, equation 51 suggests, that the number can be increased by either decreasing the Bragg angle of the observed peak or by increasing the pulse thickness.

As mentioned, this is only an estimate for the number of coefficients. Therefore, an empirical investigation is done to decide which number of coefficients is taken into account for the following retrieval.

Figure 39 shows the MAPE (see section 6.4) of the experimental result for the higher intensity gold and palladium samples to the respective simulations taking different numbers of Fourier coefficients into account. The left graph shows the dependency of the MAPE on the number of sine coefficients for the bipolar gold pulse. Since this pulse is fully symmetric, cosine coefficients were omitted.

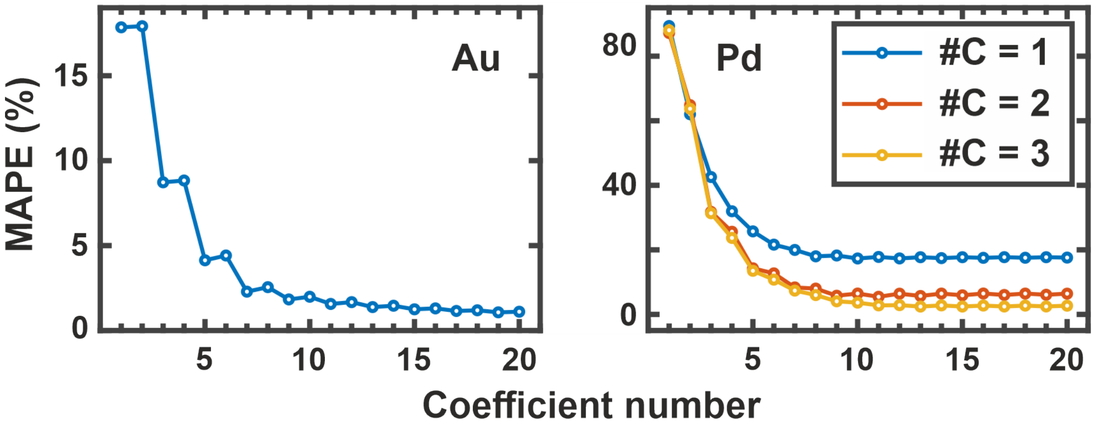

Figure 39: **Mean average percentage error between the calculated diffraction patterns of a pulse and its Fourier expansion.** The graphs show the MAPE between the calculated diffraction patterns for gold and palladium as a function of the number of sine coefficients taken into account. For palladium, the pulse is asymmetric and hence cosine coefficients have to be considered. Therefore, the curves in the right graph show the comparison for one to three cosine coefficients. For more than three cosines there is no difference visible.

After every even coefficient, there is a significant drop in the MAPE up to a number of approximately 10. For even higher numbers of coefficients only minor changes occur. The drop after the even coefficients is in line with the observation that the even sine coefficients are close to 0 for the gold pulse (see figure 38).

Taken into account, that this comparison is done on simulation data, it is reasonable to assume that it will be difficult to retrieve more than 10 Fourier coefficients from our experimental data. Hence, we will take 10 components for the further examination.

For palladium, asymmetry plays a role. Therefore, cosine coefficients have to be taken into account. The right graph of figure 39 shows the MAPE as a function of the number of sine coefficients for a different number of cosine coefficients. Again, there is a significant drop for the first approximately 6 sine coefficients for all curves followed by minor changes. An effect of the number of cosine coefficients is clearly visible. However, the differences between 2 and 3 cosines are already small for lower number of sines. A clear deviation is only visible for 10 and more coefficients. For the following discussion 6 sine and 3 cosine coefficients are regarded.

We also performed the same investigation with normalizing the pulses to the average strain to exclude, that changes of the average strain due to omitting higher order coefficients is accountable for the evolution of the MAPE. This is not the case but for the reason of clarity, the respective curves are not shown.

The previously developed parametrization of acoustic pulses together with the considerations about the retrievable number of Fourier coefficients will now be used to develop a new kind of retrieval algorithm based on deep neural networks. This will be presented in the following sections.

7.3 Deep Learning Algorithm

In this section, the utilized algorithm will be described in detail.

Generation of Training Data For the generation of training data, it is exploited that the calculation of the diffraction pattern for a known strain distribution is straight forward using dynamical X-ray diffraction theory. As a first step, the parameters $\{\bar{\eta}, d, R, S_i, C_i\}$ for the artificial creation of a strain pulse are chosen randomly within a predefined range, in which the real parameters are expected to be located. Additionally, the values of the Fourier coefficients are restricted according to the results of the last chapter: In general, the amplitude of the Fourier components decreases with increasing coefficient number. For a successful optimization, it is helpful to decrease the size of the solution space with the knowledge about the expected values.

In practice, this is accounted for by defining an envelope function, which limits the range of values. The exact shape of that function is of minor interest. In practice, the function

$$f(x) = \arctan\left(0.5x - 3\right) - \pi/2, \tag{53}$$

where x is the Fourier coefficient number, has proven to fulfill the requirements. It is shown in figure 40.

The cosine coefficients differ in two aspects. At first, they are generally one order of magnitude smaller than the sine components. Therefore, the envelope function is adjusted by a factor of 1/10. Secondly, they can have both signs. Hence, for every generated cosine coefficient, the sign is chosen randomly.

For these artificial strain pulses, the according transient diffraction patterns are calculated. We use an angular range of (-0.6°, 0.6°) around the Bragg peak and a time interval of (0 ps, 100 ps). The angular interval is dictated by the convergence angle of our X-ray beam, which defines the measurement range. The temporal interval is a compromise: On the one hand, it is supposed to be short, because we want to minimize the influence of possible acoustic non-linearities and want to be able to retrieve the strain with as little time steps as possible. On the other hand, we want to determine the interface reflectivity

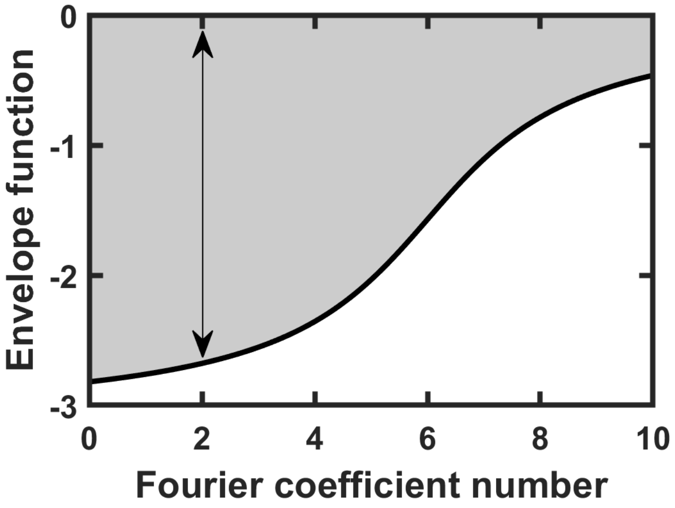

Figure 40: **Envelope function for the random choice of Fourier coefficients.** This graph shows the envelope function, which restricts the range of the amplitude of the Fourier coefficients. E.g. the arrow marks the range in which the value of the second Fourier coefficient can be chosen.

R. This is only possible, if at least the second bipolar pulse has already entered the GaAs. The resulting pairs $\{\eta(z,t),\, I(\theta,t)\}$ are used as training data for the deep neural network.

A problem of this approach is that the training data and the experimental data come from different sources. That means, there may be fundamental differences between the training data and the data to analyze. An obvious example for that is noise, which is present in our experimental data, but not in the simulated one. Such issues could complicate the analysis, reduce the achievable quality of the results, or even make the retrieval impossible.

Network Architecture For our strain retrieval, we use an established and very successful network architecture from the field of image classification: ResNet18 [43]. ResNet18 is an 18 layer deep residual convolutional neural network from the family of the ResNet networks, which have won some important image classification challenges like the ILSVRC 2015 [106].

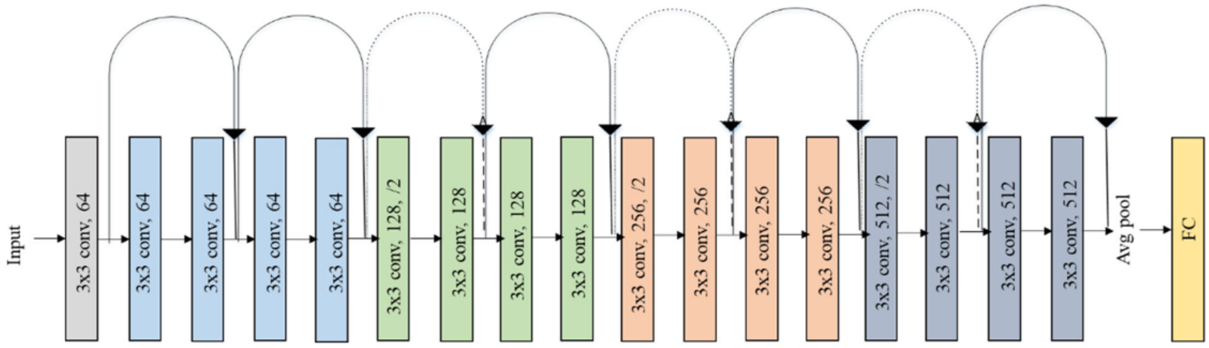

Figure 41: **ResNet18 structure.** This graph shows the general structure of the ResNet18 network architecture used in this work (taken and adapted from [92]).

The structure of ResNet18 is shown in figure 41. It consists of 18 layers of which 17 are convolutional block layers and the last one is a fully connected layer. The number of neurons in the fully connected layer is equal to the output parameters of the strain retrieval and depends on the number of Fourier coefficients taken into account.

The convolutional blocks are built of convolutional, ReLu, pooling and batch normalization layers, which were explained in section 4.4.3. Starting from block number 2, an additional connection shortcuts the path over two blocks of layers. The detailed layer sequence can be found in the literature of this section. For the work here, ResNet18 was chosen, because it is a comparably deep neural network, promising good retrieval results, but its size and parameter numbers (2.37 million) are low enough, that it can still be trained on a desktop computer with a suitable graphics processing unit in reasonable times.

Training Process Before the actual network training, the training data is preprocessed to improve the final network performance. At first, the diffraction patterns are resized to [224, 224] pixels by interpolation, which is the input size of ResNet18. At second, white Gaussian noise is added to the images to mimic real world data. The strength of this noise is a hyperparameter of the network and will be discussed in the hyperparameter section.

The strain induced intensity changes of the diffraction pattern extend over four orders of magnitude. As a third step the logarithm of the images is taken prior to the training process to account for that. Due to the properties of the logarithm, values close to 0 could dominate the whole signal afterwards. A constant value A is added to every pixel of the input image to circumvent this problem. The constant A is a second hyperparameter of the network.

The input matrix to the network is therefore calculated as:

$$I_{\mathrm{Inp}} = \log\Big(R(N(I,\, \mathrm{SNR}),\, [224, 224]) + A)\Big), \tag{54}$$

where I is the diffraction pattern, $N(M, \mathrm{SNR})$ is a function adding white Gaussian noise with a signal to noise ratio of SNR, which is a hyperparameter of the training, to a matrix M and $R(M, s)$ is a function resizing a matrix M to a size of s via interpolation.

Preprocessing is also required for the output parameters of the training data. It must be taken into account that the values of the average strain and the Fourier coefficients of the output parameter set may vary over orders of magnitude. Thus, the Fourier coefficients are normalized to the value of the average strain. The average strain itself is transformed by taking the logarithm afterwards.

The transformation of the vector of output parameters is therefore given by:

$$p = (\log(\bar{\eta}),\, S_i/\bar{\eta},\, C_i/\bar{\eta},\, d,\, R). \tag{55}$$

In general, training a deep neural network for different output parameters improves, if all the output parameters have a comparable distribution. Otherwise, a parameter with a much higher mean might dominate the updating of the network parameters. Hence, it is convenient to normalize every parameter set to have the same mean and variance, in our case a mean of 0 and a variance of 1. An often used statistical method for this is the normalized z-score. Let p_j be the set of an output parameter of the network, e.g. the average strain, with the mean μ_j and the standard deviation σ_j. The normalized z-score is then defined by:

$$\tilde{p_j} = \frac{p_j - \mu_j}{\sigma_i}. \tag{56}$$

After preprocessing, one receives a set of pairs of input matrices and output parameter vectors $\{I^i_{\mathrm{Inp}},\, \widetilde{p^i}\}$ as a foundation to train the neural network. This set is divided into two parts: 90 % of the data are used as training data. The remaining 10 % are utilized as validation data as described in section 4.4.2.

The training data is employed to train ResNet18 with an adam optimizer. After each 30 epochs of training the network performance is validated on the validation set until the validation error defined in equation 29 does not decrease for a number of validation processes. This number is called the validation patience n and is another hyperparameter of the network. If the training is stopped too early, the performance might not have reached the best possible value. If the training is stopped too late, this might lead to overfitting. A typical network training progress can be seen in figure 42.

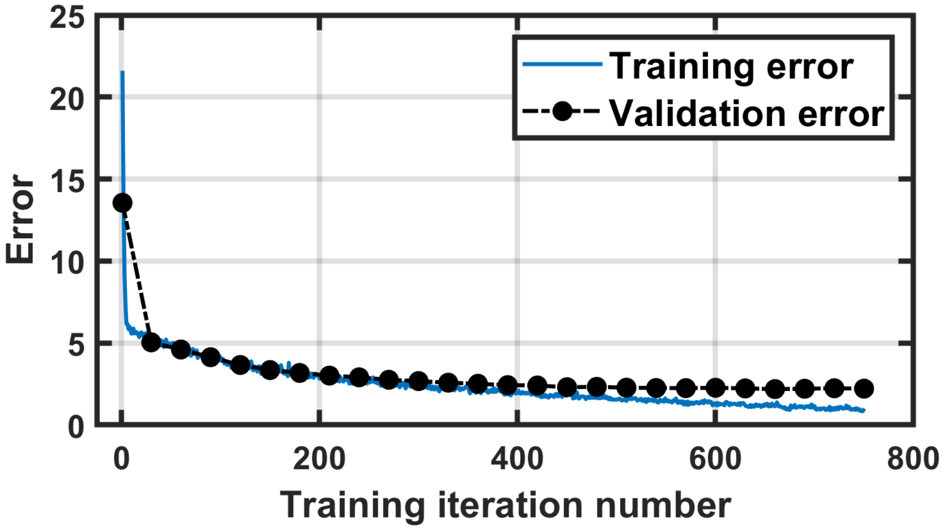

Figure 42: **Network training.** Training and validation error decrease with the iteration number. The initial drop is fast and slows down rapidly. At some point, a plateau is reached and further training could only lead to overfitting, but does not improve the performance.

Proof of Principle In the end, we want to use the trained network to analyze experimental data. As mentioned, this is complicated by the fact that training and experimental data come from different sources. Beforehand, a first test of the working principle is run to proof that a deep neural network can restore the parameters of the strain pulse from a diffraction pattern. For that, we train a network with a suitable configuration for the experimental gold data, but test it on artificial test data.

We choose 10 sine and no cosine coefficients and the respective parameter ranges are: $\bar{\eta} = (10^{-4}, 10^{-2})$, $d = (320\,\mathrm{nm}, 360\,\mathrm{nm})$, $R = (0.25, 0.6)$. For the performance test, a test data set with 100 pairs of diffraction patterns and corresponding strain pulses is created. From that set, three pairs with different orders of magnitude of the average strain are chosen randomly.

The thus received diffraction patterns are analyzed by the trained network. To get the real parameters, the transformations to the output according to equations 55 and 56 have to be undone, after receiving the output of the network. The comparison between the true parameters and the true strain pulses calculated from that parameters compared to the ones reconstructed by the network are shown in figure 43.

As can be seen, the agreement between true and reconstructed parameters and strain pulses is very good. Even for the lowest average strain, which produces a weak diffraction signal, the network is capable of retrieving the parameters well.

However, this does not necessarily say something about the performance on the experimental data. As has been already discussed, the measured patterns come from a different source and the performance may suffer.

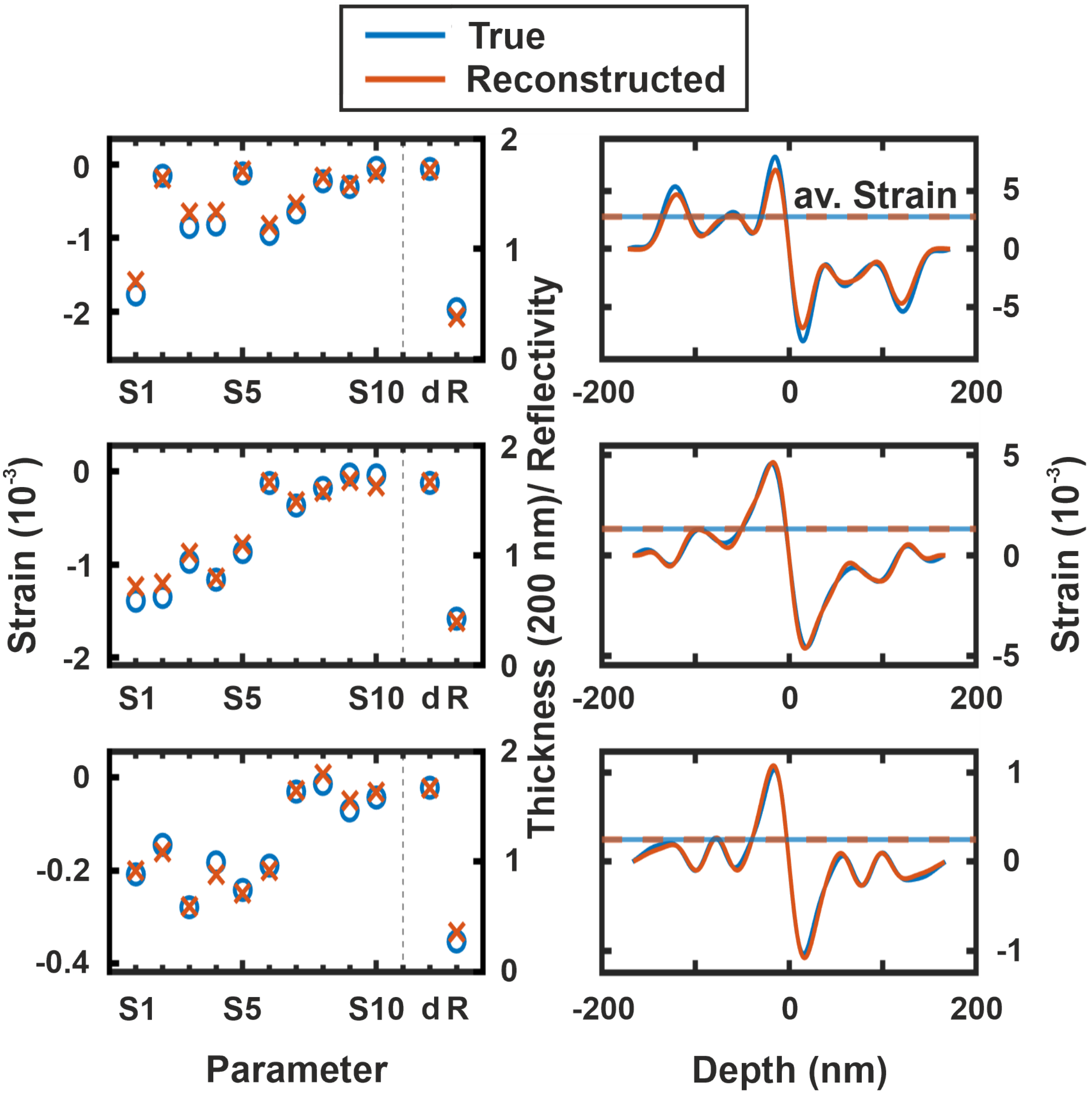

Figure 43: **Network performance on test data.** Performance of the network on three test data sets. The pairs were chosen randomly from a set of 100 test data pairs, which have not been used to train the network. The graphs on the left hand side show the true parameters (10 sine coefficients, thickness and reflectivity) and the ones retrieved by the deep neural network. The graphs on the right hand side depict the bipolar pulses built from the corresponding parameters on the left.

7.4 Strain Retrieval on Gold

In the previous section, it has been shown, that strain retrieval with deep neural networks works in principle. As a next step, we switch to the gold measurement and investigate, under which conditions strain retrieval works best. There are some differences in the preprocessing and analysis of the experimental data related to equation 54 compared to the training data.

First, there is no addition of Gaussian noise to the data. This is done for the artificial data as an attempt to approximate real world data. Noise is already inherent to the measured diffraction patterns and therefore not added again.

Second, to improve the predictability of the model, a variant of cross-validation is employed [4]. For that, the network is trained multiple times and for every training iteration the partition of training and validation data is chosen differently. On the one hand, this tends to increase the generalization capability of a deep neural network model. On the other hand, this gives multiple results for the same experimental data set, which allows to define a confidence interval for each output parameter.

Third, a weighting mechanism is introduced. After each training iteration, the diffraction pattern is calculated for the strain pulse built of the network's output parameters. The deviation of this pattern to the experimental data according to equation 38 is used as a weight. The final value of the parameters of interest is a weighted mean of the single results.

To have a measure for the quality of the result we use the MAPE of the resulting diffraction pattern to the experimental one, which was already introduced in the previous chapter.

Hyperparameter Optimization The quality of the retrieval also depends on the choice of the training's hyperparameters. In the following, the influence of different hyperparameters will be discussed. The goal is, to find an optimal set for the best retrieval possible. The dependence of the MAPE on the respective hyperparameters is shown in figure 44. For the variation of the hyperparameters shown here, all the other hyperparameters were kept constant at the optimum values (dashed lines), which were determined in an iterative process before. It should be noted, that the optimum value for one hyperparameter is stable against a variation of the others, even if they are not chosen as their respective optimum values.

Together with that, the final validation error of the training and the training time is plotted. The final validation error is the value of the error metric of the network on the validation data after the termination of the training. It allows to evaluate the influence of a hyperparameter on the network's performance on artificial data. By that, one can judge, whether an improvement is based on a general gain of the network or by a better fit to the real world data. For example, the introduction of every kind of noise will always reduce the general performance of the network on artificial data, because the training and validation data becomes noisy. Hence, the final validation error will increase. But it might improve the performance on measured data, because the noisy training data mimics the measured data better.

We are mainly interested in the trend and not in the absolute value of the final validation error. For that purpose, it is rescaled to the same range as the MAPE values, to allow for plotting it on the same axis.

The evolution of the training time on the right axis shows, if the change in performance is achieved on the back of a more costly computation. However, it should be stated that the absolute training time strongly depends on the respective computer system used for the training as well as the usage of the resources of that system. Hence, the total

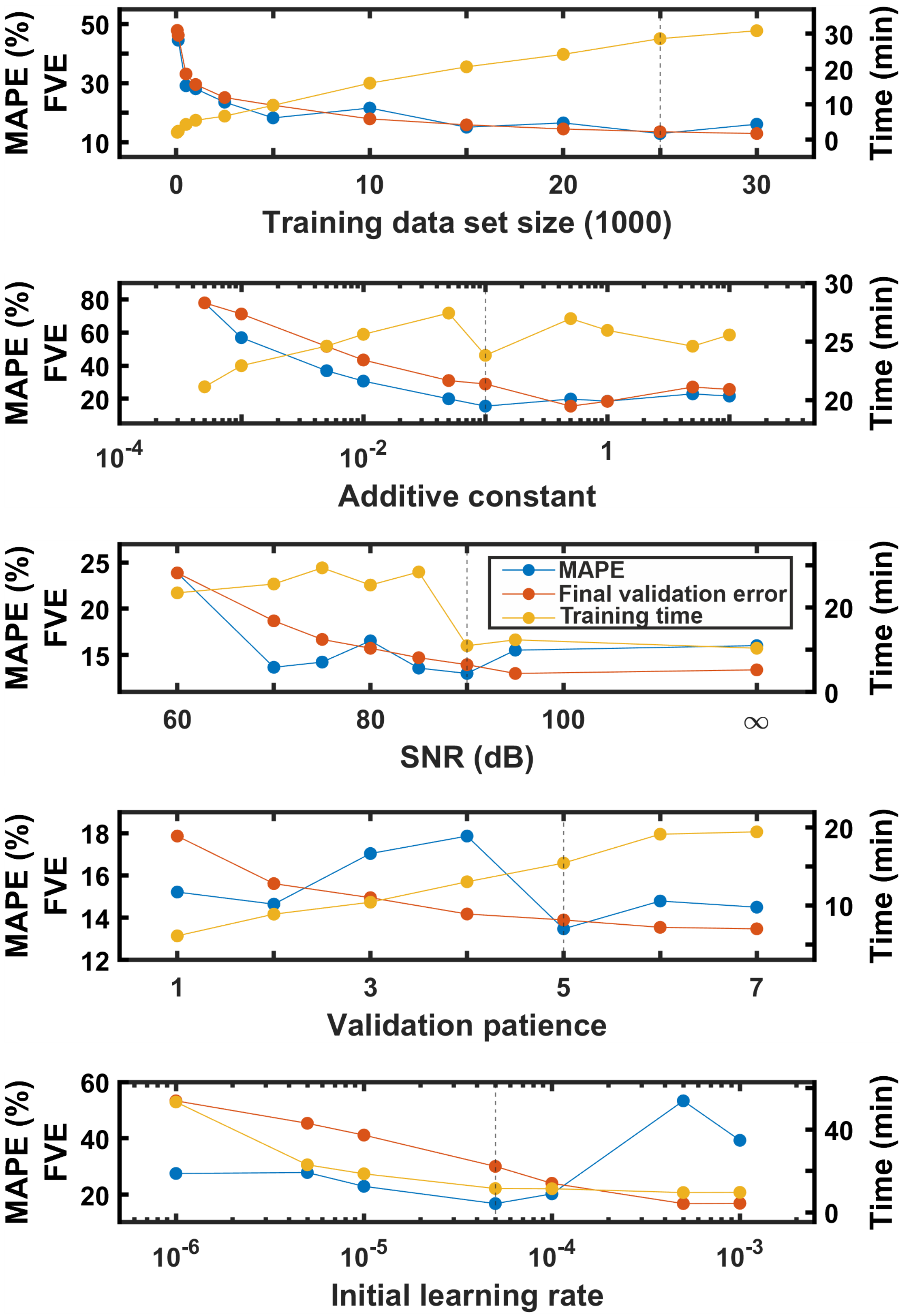

Figure 44: **Hyperparameter optimization for gold.** This figure shows the dependency of the network performance on experimental data (blue), the final validation error (red) and the training time (yellow) as a function of different hyperparameters of the network.

computation time will not be discussed in detail, but relative changes will be discussed if relevant. Since we are interested in the optimal retrieval and all trainings can be done in reasonable times, the training time only becomes important, if the achievable performance is considered similar. All simulations were either done on an Intel(R) Core i7-9700 CPU with 32 GB RAM and an NVIDIA GeForce RTX 2080 (S1) or on an AMD EPYC 7742 with 1 TB RAM and a Tesla V100S (S2).

The first question arising is the size of the training data set necessary to achieve good retrieval results. The upper row of figure 44 shows the performance enhancement with increasing data set size. As expected, the performance is bad for very low set size numbers. It increases drastically up to a number of 2500. This fast increase is followed by a slow gain with further increment of the size. The final validation error follows a similar trend. This shows, that by increasing the set size, the performance of the overall network is enhanced and the retrieval benefits on experimental data.

At the same time, the training time for a single trial also increases. As we are mainly interested in a good result and since the training time is still in a reasonable range, a size of 25,000 is chosen for the further evaluation.

The next hyperparameter under investigation is the constant A added to the input data prior to taking the logarithm. This parameter was introduced, to avoid very small values from dominating the data. It is therefore reasonable to assume that a value in the range of the normalized diffraction intensities delivers good results. To analyze this, the additive constant was varied over a range of several orders of magnitude from 5×10^{-4} up to 10. As the figure shows, the retrieval is bad for very small values, where the constant is in the typical range of the noise and increases for higher values, while the training time increases simultaneously. An optimal value is reached for 10^{-1}, which will be used for the following discussion. A further increment does not lead to a significant change of the performance or the training time.

As has been discussed, we introduced a simple model of noise to encounter for the most obvious difference between the distributions of the training data and the measured data. The free parameter of this model is the signal to noise ratio SNR. In the training, the SNR is sweeped between a very noisy signal of SNR $= 60\,\mathrm{dB}$ and a noise free input at an infinite SNR based on a power level of 1. Note, that adding noise with a SNR $\approx 80-90\,\mathrm{dB}$ to the simulated curves delivers results, which are comparably noisy to the measurements.

The network performance is very bad for really noisy signals and slightly increased for a mediocre noise level between $70-90\,\mathrm{dB}$, which is the range of noise of the experimental data. For values of $95\,\mathrm{dB}$ and upwards, there is no difference between the noisy and noise-free input. To increase the retrieval quality, we assume a mediocre noise level of SNR $=$ $90\,\mathrm{dB}$. As expected, the general network performance on artificial data generally suffers from any kind of noise, which is recognizable by the final validation error. It should be noted, that the noise level has no influence on the training time. The drop at SNR $=$ $90\,\mathrm{dB}$ is not caused by noise, but by a change of the computer system used for training.

The validation patience describes a stopping mechanism for the network training. If it is set to $n \in \mathbb{N}$, the training finishes, when the validation error has not decreased for n validation iterations. The idea is, to prevent the network from overfitting, in case the performance is only increasing on the training data, but not on the validation data anymore. The fourth row of figure 44 shows, that the validation patience has no strong influence on the retrieval of experimental data. An increase of this parameter only increases the training time and the performance on the validation data. Even though, overfitting does not seem to be an issue here, we choose a value of $n = 5$, which gave the best result in this test.

The last parameter is the initial learning rate. It is a crucial parameter in all deep network trainings. If chosen too low, the training time increases drastically, because the model needs a lot of steps, before reaching a minimum in the optimization landscape. In contrast, if the initial learning rate is chosen too high, the optimization might overshoot the valleys in the landscape and hence does not reach the optimal points. For our system, it is obvious, that the retrieval result does not change for an initial learning rate up to 10^{-4} but gets significantly worse for a further increment. Simultaneously, the training time decreases drastically with an increased initial learning rate. We therefore choose it to be 5×10^{-5}.

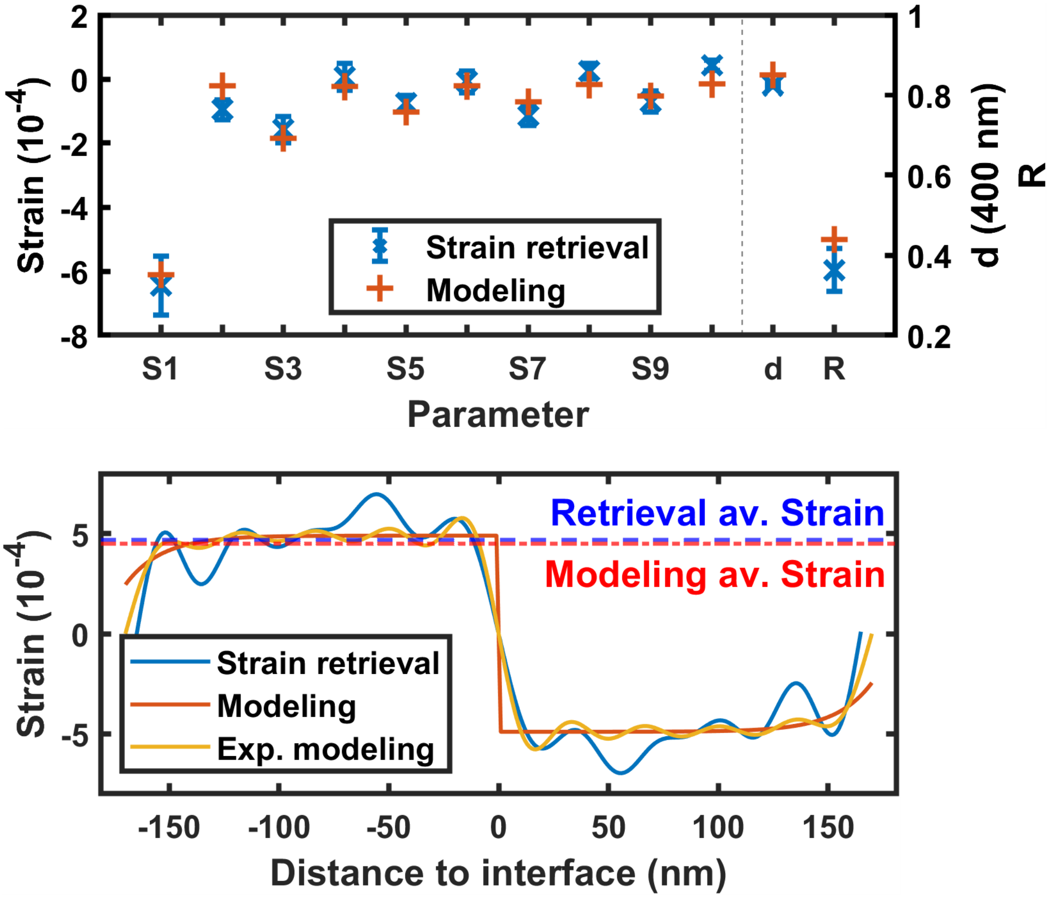

Figure 45: **Strain retrieval on gold - parameters.** This figure shows the result of the strain retrieval for the gold measurements. The upper graph compares the values of the Fourier coefficients and the material parameters d and R of the retrieved (blue) parameters and the modeling ones (red). The lower graph depicts the bipolar pulses calculated from these parameters and shows them together with the full modeling pulse including all Fourier components. The dashed dotted lines show the average strain for retrieval and modeling.

Results The optimal hyperparameters are marked by the dashed lines in figure 44 and are now used to train the network for strain retrieval on the experimental gold data. As described, the network is trained 10 times with differently partitioned training and validation data sets. The final values of the retrieval parameters are given by the weighted mean of the single trials and are plotted in the upper part of figure 45. The error bars show the weighted standard deviation of the single trial values. On the left hand side of the dashed line, the 10 sine coefficients are plotted (left axis). On the right hand side of the line, the thickness and interface reflectivity are shown (right axis). The material parameters are compared to the parameters of the modeling result described in chapter 6.

As can be seen, the retrieved parameters are all close to the modeling result. Especially, the trend of the coefficients with the alternating amplitude between even and uneven components is clearly reproduced. The highest deviation is observed for the second sine coefficient. The material parameters of the system d and R are retrieved close to the values of the modeling, too. The deviation is slightly larger for R.

The shape of the bipolar pulse shape is calculated from the parameters in the upper panel and plotted in blue in the lower panel of figure 45. For comparison, the modeling pulse is also shown together with its Fourier expansion up to an order of 10. We cannot expect the retrieval results to be closer to the modeling than this expanded curve, since this is the number of coefficients taken into account for the retrieval.

It can be seen, that the pulse shape of the modeling is reproduced well by the strain retrieval. In both curves, some unphysical oscillations occur, which originate in the Fourier nature of the pulse parametrization and the limited number of coefficients taken into account.

Especially, the overall shape of the modeling pulse of a distorted rectangle is clearly reproduced. In addition, this is also true for the strength of the strain pulse. This is represented by the average strain, which is shown in the graph as a dashed dotted line. To conclude, shape and amplitude of the pulse can be retrieved quite good.

Ultimately, the comparison to the modeling result is not the benchmark to evaluate the performance of the strain retrieval, because there might be deficiencies in the model. To judge the achievements of the strain retrieval algorithm, we therefore have to compare the resulting diffraction patterns to the experimental data.

Figure 46 shows the intensity distributions for the strain retrieval, the experimental data and the modeling approach: On the left side in 2D false color representation and on the right hand side single diffraction patterns for three selected delay times.

Comparing the false color plots, there is no clear difference visible. Strain retrieval and modeling lead to a comparable good agreement to the experimental data. Some small deviations appear, when taking a closer look at the at the diffraction patterns at particular time steps. However, there is no clear supremacy of one of the two methods.

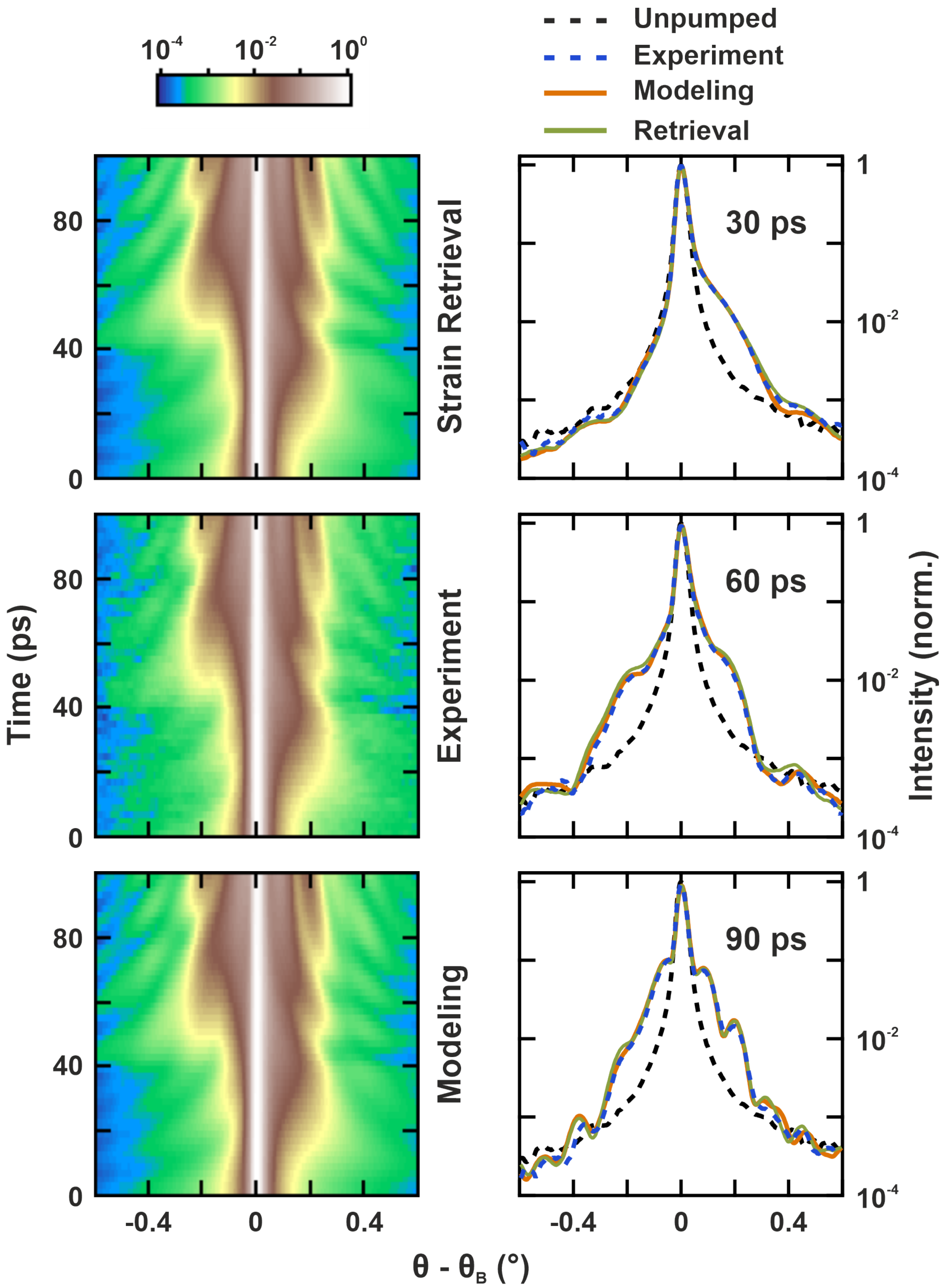

Figure 46: **Strain retrieval on gold - diffraction patterns.** This figure shows the comparison of the diffraction patterns from the experiment to the calculated ones for the strain retrieval pulse and the modeling pulse. On the left hand side, 2D false color representations for a range of 100 ps are given. On the right hand side, single rocking curves are compared for three different points in time.

7.5 Strain Retrieval on Palladium

The procedure for strain retrieval on palladium is equal to the one on gold described in the previous section. The main difference is, that 6 sine and 3 cosine coefficients are taken into account (see the previous discussion). Furthermore, the intervals of the training parameters are given by $\bar{\eta} = (10^{-4}, 10^{-2})$, $d = (160\,\mathrm{nm},\ 200\,\mathrm{nm})$, $R = (0.1,\ 0.6)$. First, we will look for an optimal set of hyperparameters, which will subsequently be used to retrieve the transient strain distribution in the palladium sample.

Hyperparameters Optimization Figure 47 shows the change of the relative mean average percentage error of the palladium strain retrieval for different values of the hyperparameters already discussed for gold. All in all, the observations are quite similar: The data set size needs to have a minimal size to ensure good network performance. In contrast to gold, a much lower number of 2500 pairs already yields the optimal result, even though the performance on validation data still increases.

A mediocre additive constant, signal to noise ratio and initial learning rate deliver an optimal performance, while keeping the training time in a reasonable range (all trainings were done on S2 in this case). The validation patience has no influence on the final result and hence, overfitting does not seem to be a decisive problem again.

The hyperparameters used in the following are marked by dashed lines.

Results Figure 48 shows the retrieved parameters and the assembled strain pulse in comparison to the results of the modeling approach. Opposing the the gold case, the retrieved parameters now include 6 sine and 3 cosine coefficients plotted on the left hand side of the dashed line.

The deviations of the Fourier components from the two sources are slightly larger than they have been for the retrieval of the gold parameters. Particularly, the 4th and 6th sine as well as the 1st and 3rd cosine component differ significantly from the modeling ones, i.e. they are clearly outside the error range of the retrieved ones. Other than that, the retrieved values for the material parameters are comparable.

However, taking a look at the bipolar pulse the differences between the two results (blue and yellow) are small. As in the gold case, the general shape of the pulse as well as the average strain are retrieved to a good extent. Obviously, the deviations of the coefficients do not result in large differences of the pulses. However, both Fourier expanded pulses differ strongly from the modeling pulse including all Fourier coefficients (red). This is why a comparison of the resulting diffraction patterns is crucial again.

Figure 49 shows the comparison of the rocking curves for both results to the experimental data. Both models reproduce the experimental rocking curves similarly well. At some points, strain retrieval is more successful (e.g. 31 ps and 0.3°), while at others the modeling gives better results (e.g. 91 ps 0.05 - 0.4°). It should be stressed, that for calculating the diffraction patterns the complete modeling pulse including all Fourier coefficients has been used.

We thus conclude, that the large real space differences between the retrieved pulse and the complete modeling pulse do not manifest in significant differences of the corresponding diffraction patterns. Hence, it is not a deficiency of the retrieval algorithm, which leads to the differences in real space, but these are mainly caused by the limited amount of information included in the diffraction pattern. This is a consequence of the high Bragg angle of the observed Bragg peak as well as the comparably small thickness of the bipolar pulse originating in the specific sample geometry and the speed of sound of the respective materials, and hence the low phonon wave vector range covered in this measurement.

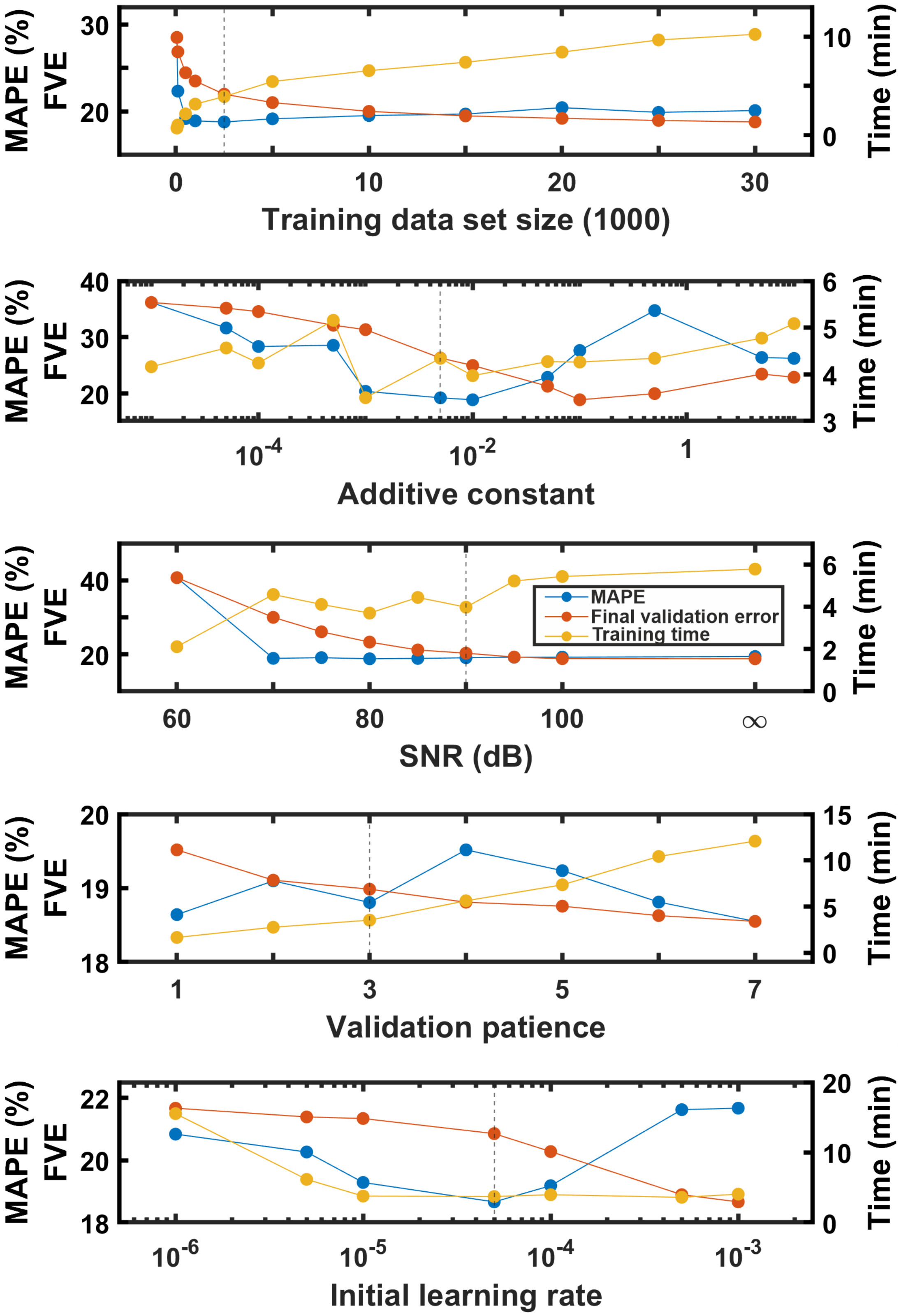

Figure 47: **Hyperparameter optimization for palladium.** This figure shows the dependency of the network performance on experimental data (blue), the final validation error (red) and the training time (yellow) as a function of different hyperparameters of the network.

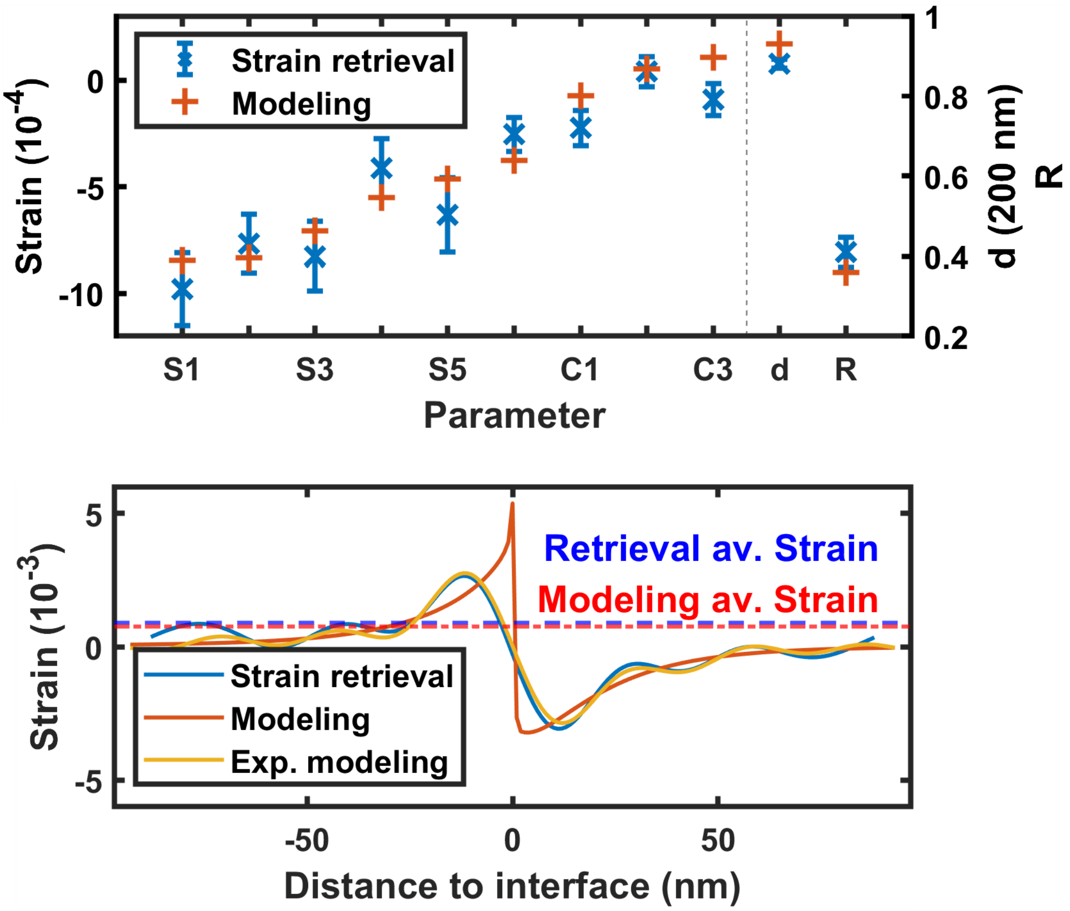

Figure 48: **Strain retrieval on palladium - parameters.**This figure shows the result of the strain retrieval by the deep learning approach for the palladium measurements. The upper graph compares the values of the Fourier coefficients and the material parameters d and R of the retrieved (blue) parameters and the modeling ones (red). The lower graph depicts the bipolar pulses calculated from these parameters and shows them together with the full modeling pulse including all Fourier components. The dashed dotted lines show the average strain for retrieval and modeling.

By construction, the strain retrieval algorithm does not include any physical model and can only reproduce the experimental data as good as possible. This is fulfilled comparably for the modeling and the strain retrieval result.

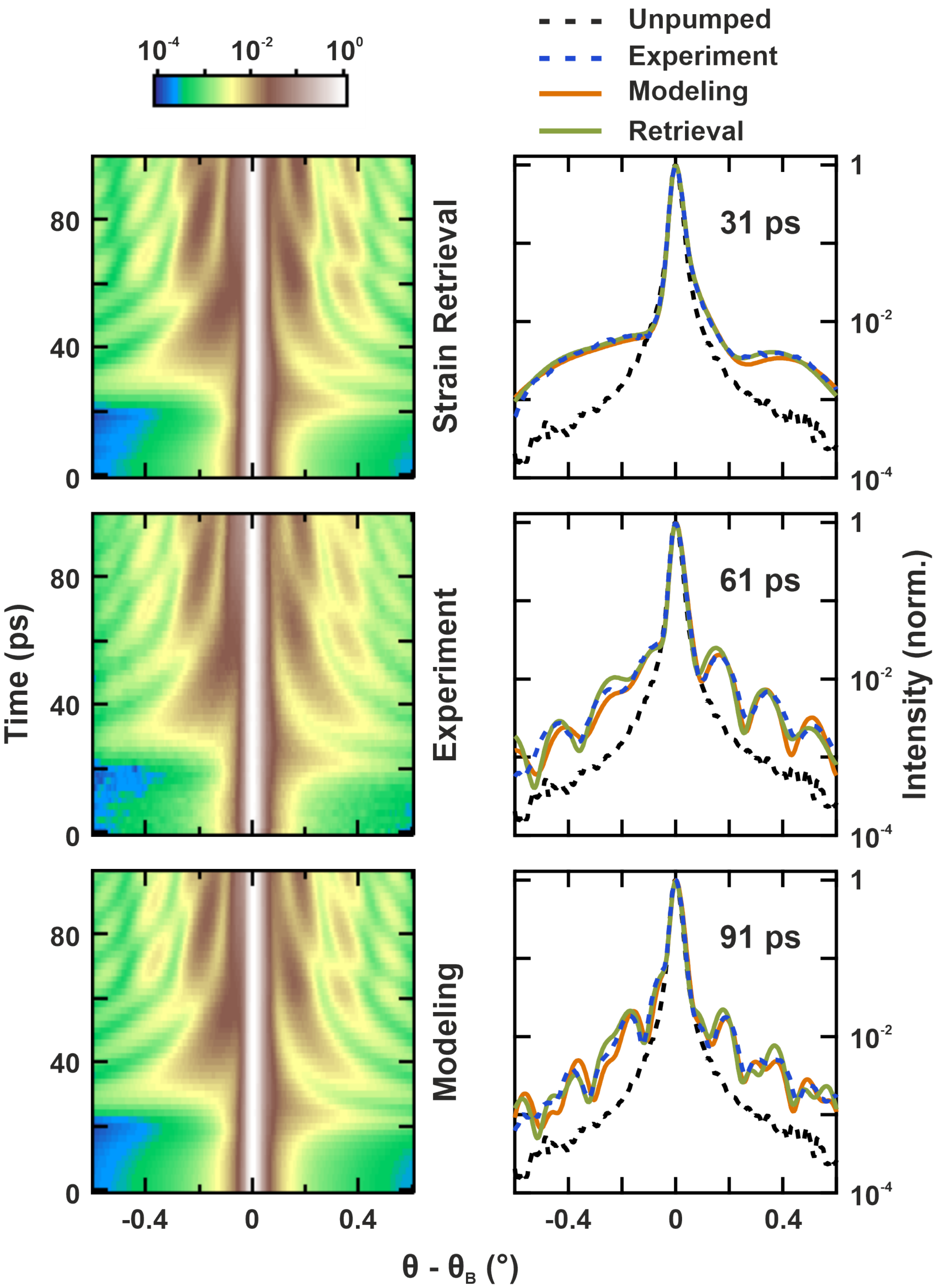

Figure 49: **Strain retrieval on palladium - diffraction patterns.** This figure shows the comparison of the diffraction patterns from the experiment to the calculated ones for the strain retrieval pulse and the modeling pulse. On the left hand side, 2D false color representations for a range of 100 ps are given. On the right hand side, single rocking curves are compared for three different points in time.

7.6 Summary

To conclude, we have shown, that a suitably constructed and trained deep neural network is capable of retrieving the strain pulse emitted in a heterostructure upon ultrafast optical excitation from time-resolved X-ray diffraction data.

To do so, the strain pulse has to be parametrized in a proper fashion. A possible choice is to use the Fourier expansion of a periodic repetition of the bipolar pulse together with a suitable gating function, which includes the pulse thickness and the interface reflectivity. This reflects the geometric form of the pulse train originating from the sample geometry.

Already well established deep neural network architectures, especially from the field of image analysis, deliver good results. This makes it possible to profit from decades of research as well as current developments in this very fast evolving field. Moreover, the influence of the network architecture has not even been investigated, yet, and might still leave room for improvement.

Careful adjustment of the hyperparameters of the training is key to success. For an optimal set, it is possible to retrieve the strain pulse to a quality comparable to the results of the modeling described in chapter 6. But if the hyperparameters are chosen suboptimal, the achievable results become worse.

We have shown, that for both material systems under more detailed investigation the experimental diffraction patterns can be reconstructed by the strain pulses retrieved by the deep neural network. In particular, the general shape of the pulse as well as the average strain level is retrieved very precisely. In this specific case it directly indicates that the energy is distributed differently inside the two metal films upon optical excitation.

This clearly shows how the two approaches can benefit from each other: By retrieving the strain from the two material systems, it becomes immediately clear that energy transport over the whole film plays an important role for the gold sample. Meanwhile, the energy stays confined to the surface region for the palladium sample. This is already a good starting point for the model generation.

At the same time, the best achievable performance is limited by the information about the strain contained in the diffraction patterns. The patterns are only influenced by certain features of the acoustic pulses and hence only these can be retrieved.

The detected wave vector range is determined by the diffraction angle and the geometry of the emitted strain pulse. This limits the achievable results in the chosen model systems, because the (400) Bragg peak of GaAs with a Bragg angle of 76.5° at 4.5 keV limits the accessible range of q-vectors. The easiest way to overcome this issue is the use of a different, lower order Bragg peak. For that purpose, we have already performed experiments on equivalent samples with (111) surface orientation in order to investigate the (111) Bragg peak at 24.9°. The experimental data is shown in figure 50 and will be analyzed in the future. With a simple estimation according to equation 51 one would expect to be sensitive to $N \approx 9$ coefficients.

Of course, two other ways to solve this problem are the use of thicker films, which admittedly can also affect the pulse shapes, or to use a different X-ray wavelength. The latter requires changes to the source.

There is also room for improvement of the algorithm, which can be exploited in the future. The next steps to go are:

1. As already discussed, the first and most important step will be to look at different material systems with more favorable properties, e.g. the new measurements on (111)-oriented GaAs, where a higher number of Fourier components should be directly accessible due to the smaller Bragg angle. This can open the way to further improvements of the presented algorithm, which were not necessary for the given systems, since the current version already yields results as good as possible.

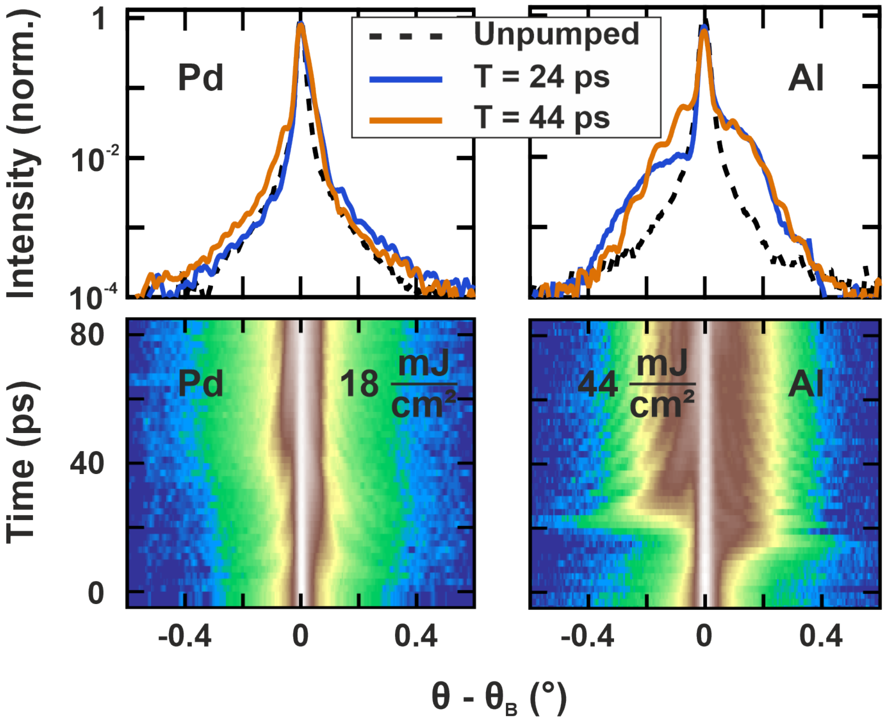

Figure 50: **First experimental results on (111)-oriented GaAs.** Single diffraction patterns and 2D false color representations of first experiments on new samples of palladium and aluminum films on top of (111)-oriented GaAs substrates.

2. The network architecture can be adapted and optimized. Up to now, a standard network was employed. A comparison of different network architectures will reveal, whether different networks show different properties and which ones are more suitable for direct strain retrieval.

3. Up to now, a very simple noise model was employed. A more sophisticated noise model which is closer to reality could deliver better results. For example, at the lowest measured intensities of 10^{-4} shot noise is expected to be the dominant noise.

4. It is not clear whether the chosen pulse parametrization is best suited for strain retrieval of acoustic pulses. Therefore, different parametrizations e.g. wavelet transformations should be tested and compared.

5. It is also possible to think of different inputs to the network. For example, instead of taking the bare experimental data as an input, one can use the Fourier transform of the experimental data in time such as shown in figure 22 in chapter 6 as the network input. This might better reflect the reciprocal space character of the experiment.

6. After improving the performance of the method, it will be interesting to investigate which areas of the 2D input are most important for the network to examine the value of a specific parameter. Up to now, the DNN is a black box and it is not clear where the information is extracted. This is a long lasting discussion in deep learning, but in recent years solution approaches such as simple occlusion [140], LIME [97] or Grad-CAM [118] were proposed. These techniques will be employed on the algorithm presented here.

Using deep neural networks for direct strain retrieval in the future is a good approach for a number of reasons. The retrieval already works well for the presented (400) experiments. In our research, we have also tried other methods like genetic algorithms and multi parameter optimization [60], which were outperformed by deep neural networks. A big advantage is, that the approach makes use of the achievements of an active research community. Therefore, new developments can be adapted and improve the strain retrieval.

A clear advantage of the model to other algorithms presented in the literature [32, 61] is that it does not require any physical assumptions prior to the retrieval. Hence, it approaches the problem from the opposite direction compared to the established modeling and both methods complement each other.

8 Conclusion and Outlook

In this work, we have presented optical pump - X-ray probe experiments of laser induced picosecond acoustic waves in heterostructures of metal films on GaAs substrates at the laboratory laser-plasma X-ray source at the University of Duisburg-Essen. By following the transient changes in the vicinity of the (400) GaAs Bragg peak upon ultrafast infrared excitation of the electronic system of the metal film, we were able to investigate the acoustic response of different material systems. The goal was, to develop a quantitative and material-specific understanding of the relevant microscopic processes, their interplay and their competition in the emission of coherent acoustic phonons.

We have presented experimental results for various metals (Pd, Au, Al, Pt, Ti) and excitation conditions. Two material systems were analyzed in detail, which are characterized by a very different strength of electron-phonon coupling: Gold with a comparably slow and palladium with a comparably fast coupling between the two subsystems, which leads to a different effect of transport mechanisms in these systems. We were able to develop a model for both by simulating the microscopic processes upon optical excitation and the induced acoustics. The simulation of the time and angle resolved X-ray diffraction intensity using dynamical X-ray diffraction theory and the comparison of the calculations to the experimental data have shown that our model is well suited to describe the underlying physics. The physical parameters which provide the best match between simulation and experiment are in good agreement with literature data.

It turned out, that an interplay of electron-phonon coupling and transport leads to the very specific acoustic response of the two materials. "Weak" electron-phonon coupling in gold in combination with efficient electronic transport leads to a distribution of the energy over the whole film thickness causing a close to rectangular shape ot the pulse train. In contrast, in palladium fast electronic transport is suppressed and the energy is confined close to the surface by strong electron-phonon coupling, inducing a nearly exponential pulse shape. We also performed fluence dependent experiments and could show, that our linear acoustic model is capable of describing the behavior over the relevant range of fluences.

Even though the modeling approach is a well established and successful way of understanding X-ray diffraction of ultrafast acoustic experiments, it suffers from various problems such as growing complexity for more difficult cases and geometries. To complement the modeling, it is a huge advantage to have a method for directly retrieving the strain from transient diffraction patterns. This is challenging, because of the phase problem in diffraction experiments.

To solve this problem, we have developed a novel algorithm for direct strain retrieval based on deep neural networks. By using pairs of randomly created strain pulses together with simulated transient diffraction patterns, a neural network was trained to analyze diffraction patterns and directly retrieve the strain pulse. Experiments on artificial examples as well as on the two previously discussed materials have proven, that the algorithm is successful in retrieving the acoustic pulses from time-resolved diffraction patterns directly. Most importantly, no a priori physical model has to be assumed, which makes the algorithm promising for future experiments on more complex systems and situations.

Moreover, we have discussed the advantages as well as the limitations of the algorithm. It turned out, that the currently discussed data only contain limited information about the exact shape of the strain pulse. This originates in the limited phonon wave vector range of the investigated material systems in the given angular range of the experimental setup. Switching to a Bragg peak with a lower Bragg angle and thus less dispersion can increase this range.

Therefore, the next step will be to deploy the algorithm for the analysis of more suitable experimental situations. First experiments on (111)-oriented GaAs samples have already been presented at the end of this thesis. This will allow for a further classification of the features of the algorithm and the optimal working conditions.

With an optimized algorithm, we aim to investigate more complex systems such as heterostructures containing e.g. perovskites, nanoparticles or 2D materials. Additionally, we want to reduce the number of required time points for a retrieval, which would ultimately allow to follow and investigate transient changes of acoustic pulses such as non-linear effects. Finally, the goal is to exploit all these findings to be able to generate tailored strain pulses for the selective, ultrafast manipulation of material properties.

Literature

[1] M. Afshari. Ultrafast acoustic response of semiconductor heterostructures analyzed by time-resolved hard X-ray diffraction. Dissertation. *University of Duisburg-Essen*, (2018).

[2] M. Afshari, P. Krumey, D. Menn, M. Nicoul, F. Brinks, A. Tarasevitch, and K. Sokolowski-Tinten. Time-resolved diffraction with an optimized short pulse laser plasma X-ray source. *Struct. Dyn.*, **7**(1):014301, (2020).

[3] A. I. Akhiezer. *Zh. Eksp.:Teor. Fiz.*, **8**:1330, (1938).

[4] D. M. Allen. The Relationship Between Variable Selection and Data Agumentation and a Method for Prediction. *Technometrics*, **16**(1):125–127, (1974).

[5] J. Als-Nielsen and D. McMorrow. Elements of Modern X-Ray Physics. *Wiley*, **1**, (2001).

[6] S. I. Anisimov, B. L. Kapeliovich, and T. L. Perelman. Electron emission from metal surfaces exposed to ultrashort laser pulses. *Zh. Eksp. Teor.Fiz.*, **66**:776–781, (1974).

[7] N. Bach and S. Schäfer. Ultrafast strain propagation and acoustic resonances in nanoscale bilayer systems. *Struct. Dyn.*, **8**(3):035101, (2021).

[8] M. Bargheer, N. Zhavoronkov, R. Bruch, H. Legall, H. Stiel, M. Woerner, and T. Elsaesser. Comparison of focusing optics for femtosecond X-ray diffraction. *Appl. Phys. B*, **80**(6):715–719, (2005).

[9] M. Bargheer, N. Zhavoronkov, Y. Gritsai, J. C. Woo, D. S. Kim, M. Woerner, and T. Elsaesser. Coherent Atomic Motions in a Nanostructure Studied by Femtosecond X-ray Diffraction. *Science*, **306**(5702):1771–1773, (2004).

[10] A. Bedford and D. S. Drumheller. Introduction to elastic wave propagation. *John Wiley & Sons, Ltd.*, **2**, (1994).

[11] Y. Beyazit, J. Beckord, P. Zhou, J. P. Meyburg, F. Kühne, D. Diesing, M. Ligges, and U. Bovensiepen. Local and Nonlocal Electron Dynamics of Au/Fe/MgO(001) Heterostructures Analyzed by Time-Resolved Two-Photon Photoemission Spectroscopy. *Phys. Rev. Lett.*, **125**:076803, (2020).

[12] G. L. Bir and G. E. Pikus. Symmetrie and Strain Induced Effects in Semiconductors. *Wiley*, (1974).

[13] U. Bovensiepen and P. Kirchmann. Elementary relaxation processes investigated by femtosecond photoelectron spectroscopy of two-dimensional materials. *Laser Photonics Rev.*, **6**(5):589–606, (2012).

[14] S. D. Brorson, A. Kazeroonian, J. S. Moodera, D. W. Face, T. K. Cheng, E. P. Ippen, M. S. Dresselhaus, and G. Dresselhaus. Femtosecond room-temperature measurement of the electron-phonon coupling constant γ in metallic superconductors. *Phys. Rev. Lett.*, **64**:2172–2175, (1990).

[15] C. Brüggemann, A. V. Akimov, A. V. Scherbakov, M. Bombeck, C. Schneider, S. Höfling, A. Forchel, D. R. Yakovlev, and M. Bayer. Laser mode feeding by shaking quantum dots in a planar microcavity. *Nat. Photonics*, **6**(1):30–34, (2012).

[16] Y. A. Burenkov, D. S. Y. Burdukov, Yu. M., and S. P. Nikanorov. *Sov. Phys. Solid State*, **15**:1175 – 1177, (1973).

[17] A. Cavalleri, C. W. Siders, F. L. H. Brown, D. M. Leitner, C. Tóth, J. A. Squier, C. P. J. Barty, K. R. Wilson, K. Sokolowski-Tinten, M. Horn von Hoegen, D. von der Linde, and M. Kammler. Anharmonic Lattice Dynamics in Germanium Measured with Ultrafast X-Ray Diffraction. *Phys. Rev. Lett.*, **85**:586–589, (2000).

[18] T. Chase, M. Trigo, A. H. Reid, R. Li, T. Vecchione, X. Shen, S. Weathersby, R. Coffee, N. Hartmann, D. A. Reis, X. J. Wang, and H. A. Dürr. Ultrafast electron diffraction from non-equilibrium phonons in femtosecond laser heated Au films. *Applied Physics Letters*, 108(4):041909, (2016).

[19] P. Chen, I. V. Tomov, and P. M. Rentzepis. Time resolved heat propagation in a gold crystal by means of picosecond x-ray diffraction. *J. Chem. Phys.*, **104**(24):10001–10007, (1996).

[20] A. H. Chin, R. W. Schoenlein, T. E. Glover, P. Balling, W. P. Leemans, and C. V. Shank. Ultrafast structural dynamics in InSb Probed by Time-Resolved X-ray Diffraction. *Phys. Rev. Lett.*, **83**:336–339, (1999).

[21] T. Ciodaro, D. Deva, J. M. de Seixas, and D. Damazio. Online particle detection with Neural Networks based on topological calorimetry information. *J. Phys. Conf. Ser.*, **368**:012030, (2012).

[22] T. Czerniuk, D. Wigger, A. V. Akimov, C. Schneider, M. Kamp, S. Höfling, D. R. Yakovlev, T. Kuhn, D. E. Reiter, and M. Bayer. Picosecond Control of Quantum Dot Laser Emission by Coherent Phonons. *Phys. Rev. Lett.*, **118**:133901, (2017).

[23] C. David, P. Avizonis, H. Weichel, and K. Pyatt. Density and temperature of a laser induced plasma. *IEEE J. Quantum Electron.*, **2**(9):493–499, (1966).

[24] M. F. DeCamp, D. A. Reis, P. H. Bucksbaum, B. Adams, J. M. Caraher, R. Clarke, C. W. S. Conover, E. M. Dufresne, R. Merlin, V. Stoica, and J. K. Wahlstrand. Coherent control of pulsed X-ray beams. *Nature*, **413**(6858):825–828, (2001).

[25] M. F. DeCamp, D. A. Reis, A. Cavalieri, P. H. Bucksbaum, R. Clarke, R. Merlin, E. M. Dufresne, D. A. Arms, A. M. Lindenberg, A. G. MacPhee, Z. Chang, B. Lings, J. S. Wark, and S. Fahy. Transient Strain Driven by a Dense Electron-Hole Plasma. *Phys. Rev. Lett.*, **91**:165502, (2003).

[26] W. S. Fann, R. Storz, H. W. K. Tom, and J. Bokor. Electron thermalization in gold. *Phys. Rev. B*, **46**:13592–13595, (1992).

[27] C. Farabet, C. Couprie, L. Najman, and Y. LeCun. Learning Hierarchical Features for Scene Labeling. *IEEE Trans. Pattern Anal. Mach. Intell.*, **35**(8):1915–1929, (2013).

[28] A. Feist, N. Rubiano da Silva, W. Liang, C. Ropers, and S. Schäfer. Nanoscale diffractive probing of strain dynamics in ultrafast transmission electron microscopy. *Struct. Dyn.*, **5**(1):014302, (2018).

[29] T. Feurer, A. Morak, I. Uschmann, C. Ziener, H. Schwoerer, E. Förster, and R. Sauerbrey. An incoherent sub-picosecond X-ray source for time-resolved X-ray-diffraction experiments. *Appl. Phys. B*, **72**(1):15–20, (2001).

[30] M. V. Fischetti and S. E. Laux. Band structure, deformation potentials, and carrier mobility in strained Si, Ge, and SiGe alloys. *J. Appl. Phys.*, **80**(4):2234–2252, (1996).

[31] H. X. Gao and L.-M. Peng. Parameterization of the temperature dependence of the Debye–Waller factors. *Acta Crystallogr. A*, **55**(5):926–932, (1999).

[32] Y. Gao, Z. Chen, Z. Bond, A. Loether, L. E. Howard, S. LeMar, S. White, A. Watts, B. C. Walker, and M. F. DeCamp. Reconstructing longitudinal strain pulses using time-resolved x-ray diffraction. *Phys. Rev. B*, **88**:014302, (2013).

[33] Y. Gao and M. F. DeCamp. Generation of acoustic pulses from a photoacoustic transducer measured by time-resolved x-ray diffraction. *Appl. Phys. Lett.*, **100**(19):191903, (2012).

[34] Y. Gavrilova. A Guide to Deep Learning and Neural Networks. `https://serokell.io/blog/deep-learning-and-neural-network-guide#components-of-neural-networks`, (2020).

[35] R. W. Gerchberg and W. O. Saxton. A practical algorithm for the determination of phase from image and diffraction plane pictures. *Optik*, **35**:237–246, (1972).

[36] X. Glorot, A. Bordes, and Y. Bengio. Deep Sparse Rectifier Neural Networks. *J. Mach. Learn. Res.*, **15**, (2010).

[37] N. N. Greenwood and A. Earnshow. Chemie der Elemente. *VCH Weinheim*, **1**, (1988).

[38] R. H. M. Groeneveld, R. Sprik, and A. Lagendijk. Femtosecond spectroscopy of electron-electron and electron-phonon energy relaxation in Ag and Au. *Phys. Rev. B*, **51**:11433–11445, (1995).

[39] D. Gross. Bruchmechanik mit einer Einführung in die Mikromechanik. *Springer*, (2007).

[40] T. Guo, C. Spielmann, B. C. Walker, and C. P. J. Barty. Generation of hard x rays by ultrafast terawatt lasers. *Rev. Sci. Instrum.*, **72**(1):41–47, (2001).

[41] H. A. Hauptman. The Phase Problem of X-ray Crystallography: Overview, Electron Crystallography. *Springer*, **347**:131–138, (1997).

[42] K. He and J. Sun. Convolutional neural networks at constrained time cost. In *2015 IEEE Conference on Computer Vision and Pattern Recognition (CVPR)*, pages 5353–5360, (2015).

[43] K. He, X. Zhang, S. Ren, and J. Sun. Deep Residual Learning for Image Recognition. In *2016 IEEE Conference on Computer Vision and Pattern Recognition (CVPR)*, pages 770–778, (2016).

[44] M. Herzog, A. Bojahr, J. Goldshteyn, W. Leitenberger, I. Vrejoiu, D. Khakhulin, M. Wulff, R. Shayduk, P. Gaal, and M. Bargheer. Detecting optically synthesized quasi-monochromatic sub-terahertz phonon wavepackets by ultrafast x-ray diffraction. *Appl. Phys. Lett.*, **100**(9):094101, (2012).

[45] M. Herzog, W. Leitenberger, R. Shayduk, R. M. van der Veen, C. J. Milne, S. L. Johnson, I. Vrejoiu, M. Alexe, D. Hesse, and M. Bargheer. Ultrafast manipulation of hard x-rays by efficient Bragg switches. *Appl. Phys. Lett.*, **96**(16):161906, (2010).

[46] M. Herzog, D. Schick, P. Gaal, R. Shayduk, C. v. Korff Schmising, and M. Bargheer. Analysis of ultrafast X-ray diffraction data in a linear-chain model of the lattice dynamics. *Appl. Phys. A*, **106**(3):489–499, (2012).

[47] G. Hinton, L. Deng, D. Yu, G. E. Dahl, A.-r. Mohamed, N. Jaitly, A. Senior, V. Vanhoucke, P. Nguyen, T. N. Sainath, and B. Kingsbury. Deep Neural Networks for Acoustic Modeling in Speech Recognition: The Shared Views of Four Research Groups. *IEEE Signal Process. Mag.*, **29**(6):82–97, (2012).

[48] C. Y. Ho, R. W. Powell, and P. E. Liley. Thermal Conductivity of the Elements: A Comprehensive Review. *J. Phys. Chem. Ref. Data*, **3**(1):502, (1974).

[49] J. Hohlfeld, S. S. Wellershoff, J. Güdde, U. Conrad, V. Jähnke, and E. Matthias. Electron and lattice dynamics following optical excitation of metals. *Chem. Phys.*, **251**(1):237–258, (2000).

[50] H. Ibach and H. Lüth. Festkörperphysik. *Springer*, **7**, (2009).

[51] A. Jarnac, X. Wang, . U. J. Bengtsson, J. C. Ekström, H. Enquist, A. Jurgilaitis, D. Kroon, A. I. H. Persson, V.-T. Pham, C. M. Tu, and J. Larsson. Communication: Demonstration of a 20 ps X-ray switch based on a photoacoustic transducer. *Struct. Dyn.*, **4**(5):051102, (2017).

[52] M. Jocic, Đorđe Obradović, V. Malbasa, and Z. Konjovic. Image tagging with an ensemble of deep convolutional neural networks. *7th International Conference on Information Society and Technology ICIST*, (2017).

[53] P. B. Johnson and R. W. Christy. Optical Constants of the Noble Metals. *Phys. Rev. B*, **6**:4370–4379, (1972).

[54] D. P. Kingma and J. Ba. Adam: A Method for Stochastic Optimization. *ICLR*, (2015).

[55] C. Kittel. Einführung in die Festkörperphysik. *Oldenburg*, **6**, (1983).

[56] B. Klar and F. Rustichelli. Dynamical Neutron Diffraction by Ideally Curved Crystals. *Il Nuovo Cimento*, **13**(2):249–271, (1973).

[57] A. Koc, M. Reinhardt, A. von Reppert, M. Rössle, W. Leitenberger, M. Gleich, M. Weinelt, F. Zamponi, and M. Bargheer. Grueneisen-approach for the experimental determination of transient spin and phonon energies from ultrafast x-ray diffraction data: gadolinium. *J. Phys. Condens. Matter*, **29**(26):264001, (2017).

[58] C. v. Korff Schmising, A. Harpoeth, N. Zhavoronkov, Z. Ansari, C. Aku-Leh, M. Woerner, T. Elsaesser, M. Bargheer, M. Schmidbauer, I. Vrejoiu, D. Hesse, and M. Alexe. Ultrafast magnetostriction and phonon-mediated stress in a photoexcited ferromagnet. *Phys. Rev. B*, **78**:060404, (2008).

[59] A. Krizhevsky, I. Sutskever, and G. E. Hinton. ImageNet Classification with Deep Convolutional Neural Networks. In *Advances in Neural Information Processing Systems*, volume **25**. Curran Associates, Inc., (2012).

[60] P. Krumey. Zeitaufgelöste Röntgenbeugung an Metall-Isolator Heterostrukturen. Master Thesis. *University of Duisburg-Essen*, (2021).

[61] K. T. Lai, D. Finkelstein-Shapiro, A. Devos, and P.-A. Mante. Ultrafast strain waves reconstruction from coherent acoustic phonons reflection. *Appl. Phys. Lett.*, **119**(9):091106, (2021).

[62] B. C. Larson, J. Z. Tischler, and D. M. Mills. Nanosecond resolution time-resolved x-ray study of silicon during pulsed-laser irradiation. *J. Mater. Sci*, **1**(1):144–154, (1986).

[63] J. Larsson, A. Allen, P. H. Bucksbaum, R. W. Falcone, A. Lindenberg, G. Naylor, T. Missalla, D. A. Reis, K. Scheidt, A. Sjögren, P. Sondhauss, M. Wulff, and J. S. Wark. Picosecond X-ray diffraction studies of laser-excited acoustic phonons in InSb. *Appl. Phys. A*, **75**(4):467–478, (2002).

[64] Y. A. LeCun, L. Bottou, G. B. Orr, and K.-R. Müller. Neural Networks: Tricks of the Trade: Efficient BackProp. *Springer Berlin Heidelberg*, **2**:9–48, (2012).

[65] H. J. Lee, J. Workman, J. S. Wark, R. D. Averitt, A. J. Taylor, J. Roberts, Q. McCulloch, D. E. Hof, N. Hur, S.-W. Cheong, and D. J. Funk. Optically induced lattice dynamics probed with ultrafast x-ray diffraction. *Phys. Rev. B*, **77**:132301, (2008).

[66] R. Li, O. A. Ashour, J. Chen, H. E. Elsayed-Ali, and P. M. Rentzepis. Femtosecond laser induced structural dynamics and melting of Cu (111) single crystal. An ultrafast time-resolved x-ray diffraction study. *J. Appl. Phys.*, **121**(5):055102, (2017).

[67] Z. Lin, L. V. Zhigilei, and V. Celli. Electron-phonon coupling and electron heat capacity of metals under conditions of strong electron-phonon nonequilibrium. *Phys. Rev. B*, **77**:075133, (2008).

[68] D. R. Linde. CRC Handbook of Chemistry. *CRC Press: Taylor & Francis Group*, **88**, (2008).

[69] A. M. Lindenberg, I. Kang, S. L. Johnson, T. Missalla, P. A. Heimann, Z. Chang, J. Larsson, P. H. Bucksbaum, H. C. Kapteyn, H. A. Padmore, R. W. Lee, J. S. Wark, and R. W. Falcone. Time-resolved X-Ray diffraction from coherent phonons during a laser-induced phase transition. *Phys. Rev. Lett.*, **84**(1):111–114, (2000).

[70] A. Loether, Y. Gao, Z. Chen, M. F. DeCamp, E. M. Dufresne, D. A. Walko, and H. Wen. Transient crystalline superlattice generated by a photoacoustic transducer. *Struct. Dyn.*, **1**(2):024301, (2014).

[71] W. Lu. Ultrafast time-resolved x-ray diffraction using an optimized laser plasma based x-ray source. *University of Duisburg-Essen*, (2013).

[72] W. Lu, M. Nicoul, U. Shymanovich, F. Brinks, M. Afshari, A. Tarasevitch, D. von der Linde, and K. Sokolowski-Tinten. Acoustic response of a laser-excited polycrystalline Au-film studied by ultrafast Debye–Scherrer diffraction at a table-top short-pulse x-ray source. *AIP Adv.*, **10**(3):035015, (2020).

[73] J. Ma, R. P. Sheridan, A. Liaw, G. E. Dahl, and V. Svetnik. Deep Neural Nets as a Method for Quantitative Structure–Activity Relationships. *J. Chem. Inf. Model.*, **55**(2):263–274, (2015).

[74] J. P. Mathews, Q. P. Campbell, H. Xu, and P. Halleck. A review of the application of X-ray computed tomography to the study of coal. *Fuel*, **209**:10–24, (2017).

[75] M. Mattern, A. von Reppert, S. P. Zeuschner, J.-E. Pudell, F. Kühne, D. Diesing, M. Herzog, and M. Bargheer. Electronic energy transport in nanoscale Au/Fe hetero-structures in the perspective of ultrafast lattice dynamics. *Appl. Phys. Lett.*, **120**(9):092401, (2022).

[76] R. A. Matula. Electrical resistivity of copper, gold, palladium, and silver. *J. Phys. Chem. Ref. Data*, **8**(4):1147–1298, (1979).

[77] M. Milnikel. private communication. *University of Duisburg-Essen*, (2022).

[78] T. Missalla, I. Uschmann, E. Förster, G. Jenke, and D. von der Linde. Monochromatic focusing of subpicosecond x-ray pulses in the keV range. *Rev. Sci. Instrum.*, **70**:1288, (1999).

[79] K. P. Murphy. Machine Learning: A Probabalistic Perspective. *The MIT Press*, (2012).

[80] J. R. Neighbours and G. A. Alers. Elastic Constants of Silver and Gold. *Phys. Rev.*, **111**:707–712, (1958).

[81] M. Nicoul. Time-resolved X-ray diffraction with accelerator- and laser-plasma-based X-ray sources. Dissertation. *University of Duisburg-Essen*, (2011).

[82] M. Nicoul, U. Shymanovich, S. Kähle, T. Caughey, D. Sampat, K. Sokolowski-Tinten, and D. von der Linde. Bent crystal x-ray mirrors for time-resolved experiments with femtosecond laser-produced x-ray pulses. *J. Phys. Conf. Ser.*, **21**:207–210, (2005).

[83] M. Nicoul, U. Shymanovich, A. Tarasevitch, D. von der Linde, and K. Sokolowski-Tinten. Picosecond acoustic response of a laser-heated gold-film studied with time-resolved x-ray diffraction. *Appl. Phys. Lett.*, **98**(19):191902, (2011).

[84] S. Nie, X. Wang, H. Park, R. Clinite, and J. Cao. Measurement of the Electronic Grüneisen Constant Using Femtosecond Electron Diffraction. *Phys. Rev. Lett.*, **96**:025901, (2006).

[85] M. A. Nielsen. Neural Networks and Deep Learning. *Determination Press*, (2015).

[86] H. Park, X. Wang, S. Nie, R. Clinite, and J. Cao. Mechanism of coherent acoustic phonon generation under nonequilibrium conditions. *Phys. Rev. B*, **72**:100301, (2005).

[87] B. Perrin, C. Rossignol, B. Bonello, and J.-C. Jeannet. Interferometric detection in picosecond ultrasonics. *Physica B: Cond. Matter*, **263**:571–573, (1999).

[88] A. I. H. Persson, H. Enquist, A. Jurgilaitis, B. P. Andreasson, and J. Larsson. Real-time observation of coherent acoustic phonons generated by an acoustically mismatched optoacoustic transducer using x-ray diffraction. *J. Appl. Phys.*, **118**(18):185308, (2015).

[89] A. I. H. Persson, A. Jarnac, X. Wang, H. Enquist, A. Jurgilaitis, and J. Larsson. Studies of electron diffusion in photo-excited Ni using time-resolved X-ray diffraction. *Appl. Phys. Lett.*, **109**(20):203115, (2016).

[90] P. A. Prosekov, V. L. Nosik, and A. E. Blagov. Methods of Coherent X-Ray Diffraction Imaging. *Crystallogr. Rep.*, **66**(6):867–882, (2021).

[91] F. Pérez-Cota, R. Fuentes-Domínguez, S. La Cavera, W. Hardiman, M. Yao, K. Setchfield, E. Moradi, S. Naznin, A. Wright, K. F. Webb, A. Huett, C. Friel, V. Sottile, H. M. Elsheikha, R. J. Smith, and M. Clark. Picosecond ultrasonics for elasticity-based imaging and characterization of biological cells. *J. Appl. Phys.*, **128**(16):160902, (2020).

[92] F. Ramzan, M. U. G. Khan, A. Rehmat, S. Iqbal, T. Saba, A. Rehman, and Z. Mehmood. A Deep Learning Approach for Automated Diagnosis and Multi-Class Classification of Alzheimer's Disease Stages Using Resting-State fMRI and Residual Neural Networks. *J. Med. Syst.*, **44**(2):37, (2019).

[93] J. A. Rayne. Elastic Constants of Palladium from 4.2-300°K. *Phys. Rev.*, **118**:1545–1549, (1960).

[94] C. Reich, P. Gibbon, I. Uschmann, and E. Förster. Yield Optimization and Time Structure of Femtosecond Laser Plasma $K\alpha$ Sources. *Phys. Rev. Lett.*, **84**:4846–4849, (2000).

[95] C. Reich, I. Uschmann, F. Ewald, S. Düsterer, A. Lübcke, H. Schwoerer, R. Sauerbrey, E. Förster, and P. Gibbon. Spatial characteristics of Kα x-ray emission from relativistic femtosecond laser plasmas. *Phys. Rev. E*, **68**:056408, (2003).

[96] D. A. Reis, M. F. DeCamp, P. H. Bucksbaum, R. Clarke, E. Dufresne, M. Hertlein, R. Merlin, R. Falcone, H. Kapteyn, M. M. Murnane, J. Larsson, T. Missalla, and J. S. Wark. Probing impulsive strain propagation with X-ray pulses. *Phys. Rev. Lett.*, **86**(14):3072–3075, (2001).

[97] M. T. Ribeiro, S. Singh, and C. Guestrin. "Why Should I Trust You?": Explaining the Predictions of Any Classifier. KDD '16, page 1135–1144, New York, NY, USA, (2016). Association for Computing Machinery.

[98] H. M. Rietveld. A profile refinement method for nuclear and magnetic structures. *Journal of Applied Crystallography*, **2**(2):65–71, (1969).

[99] H. Robbins and S. Monro. A Stochastic Approximation Method. *Ann. Math. Stat.*, **22**(3):400 – 407, (1951).

[100] C. Rose-Petruck, R. Jimenez, T. Guo, A. Cavalleri, C. W. Siders, F. Rksi, J. A. Squier, B. C. Walker, K. R. Wilson, and C. P. J. Barty. Picosecond–milliångström lattice dynamics measured by ultrafast X-ray diffraction. *Nature*, **398**(6725):310–312, (1999).

[101] F. Rosenblatt. The perceptron: A probabalistic model for information storage and organization in the brain. *Psychol. Rev.*, **65**(6):386–408, (1958).

[102] C. Rossignol, N. Chigarev, M. Ducousso, B. Audoin, G. Forget, F. Guillemot, and M. C. Durrieu. In Vitro picosecond ultrasonics in a single cell. *Appl. Phys. Lett.*, **93**(12):123901, (2008).

[103] A. Rousse, P. Audebert, J. P. Geindre, F. Falliès, J. C. Gauthier, A. Mysyrowicz, G. Grillon, and A. Antonetti. Efficient Kα x-ray source from femtosecond laser-produced plasmas. *Phys. Rev. E*, **50**:2200–2207, (1994).

[104] P. Ruello and V. E. Gusev. Physical mechanisms of coherent acoustic phonons generation by ultrafast laser action. *Ultrasonics*, **56**:21–35, (2015).

[105] D. E. Rumelhart, G. E. Hinton, and R. J. Williams. Learning representations by back-propagating errors. *Nature*, **323**(6088):533–536, (1986).

[106] O. Russakovsky, J. Deng, H. Su, J. Krause, S. Satheesh, S. Ma, Z. Huang, A. Karpathy, A. Khosla, M. Bernstein, A. C. Berg, and L. Fei-Fei. ImageNet Large Scale Visual Recognition Challenge. *Int. J. Comput. Vis.*, **115**(3):211–252, (2015).

[107] W. C. Röntgen. On a New Kind of Rays. *Nature*, **53**(1369):274–276, (1896).

[108] M. Sanchez and R. J. Dejus. Status of XOP: v2.4: recent developments of the x-ray optics software toolkit. *Proc. SPIE*, **8141**:814115, (2011).

[109] S. Santurkar, D. Tsipras, A. Ilyas, and A. Madry. How Does Batch Normalization Help Optimization? In *Advances in Neural Information Processing Systems*, volume **31**. Curran Associates, Inc., (2018).

[110] Z. Sayers, B. Avşar, E. Cholak, and I. Karmous. Application of advanced X-ray methods in life sciences. *Biochim et Biophys Acta Gen Subj*, **1861**(1, Part B):3671–3685, (2017).

[111] D. Scherer, A. Müller, and S. Behnke. Evaluation of Pooling Operations in Convolutional Architectures for Object Recognition. In *Artificial Neural Networks – ICANN 2010*. Springer Berlin Heidelberg, (2010).

[112] D. Schick, A. Bojahr, M. Herzog, P. Gaal, I. Vrejoiu, and M. Bargheer. Following Strain-Induced Mosaicity Changes of Ferroelectric Thin Films by Ultrafast Reciprocal Space Mapping. *Phys. Rev. Lett.*, **110**:095502, (2013).

[113] D. Schick, A. Bojahr, M. Herzog, R. Shayduk, C. von Korff Schmising, and M. Bargheer. udkm1Dsim—A simulation toolkit for 1D ultrafast dynamics in condensed matter. *Comput. Phys. Commun.*, **185**(2):651–660, (2014).

[114] D. Schick, M. Herzog, A. Bojahr, W. Leitenberger, A. Hertwig, R. Shayduk, and M. Bargheer. Ultrafast lattice response of photoexcited thin films studied by X-ray diffraction. *Struct. Dyn.*, **1**(6):064501, (2014).

[115] D. Schick, M. Herzog, H. Wen, P. Chen, C. Adamo, P. Gaal, D. G. Schlom, P. G. Evans, Y. Li, and M. Bargheer. Localized Excited Charge Carriers Generate Ultrafast Inhomogeneous Strain in the Multiferroic $BiFeO_3$. *Phys. Rev. Lett.*, **112**:097602, (2014).

[116] P. Sedigh Rahimabadi, M. Khodaei, and K. R. Koswattage. Review on applications of synchrotron-based X-ray techniques in materials characterization. *XRay Spectrom*, **49**(3):348–373, (2020).

[117] H. Seiler, D. Zahn, M. Zacharias, P.-N. Hildebrandt, T. Vasileiadis, Y. W. Windsor, Y. Qi, C. Carbogno, C. Draxl, R. Ernstorfer, and F. Caruso. Accessing the Anisotropic Nonthermal Phonon Populations in Black Phosphorus. *Nano Lett.*, **21**(14):6171–6178, (2021).

[118] R. R. Selvaraju, M. Cogswell, A. Das, R. Vedantam, D. Parikh, and D. Batra. Grad-CAM: Visual Explanations from Deep Networks via Gradient-Based Localization. In *2017 IEEE International Conference on Computer Vision (ICCV)*, pages 618–626, (2017).

[119] R. Shayduk, J. Hallmann, A. Rodriguez-Fernandez, M. Scholz, W. Lu, U. Bösenberg, J. Möller, A. Zozulya, M. Jiang, U. Wegner, R.-C. Secareanu, G. Palmer, M. Emons, M. Lederer, S. Volkov, I. Lindfors-Vrejoiu, D. Schick, M. Herzog, M. Bargheer, and A. Madsen. Femtosecond x-ray diffraction study of multi-THz coherent phonons in SrTiO3. *Appl. Phys. Lett.*, **120**(20):202203, (2022).

[120] R. Shayduk, M. Herzog, A. Bojahr, D. Schick, P. Gaal, W. Leitenberger, H. Navirian, M. Sander, J. Goldshteyn, I. Vrejoiu, and M. Bargheer. Direct time-domain sampling of subterahertz coherent acoustic phonon spectra in $SrTiO_3$ using ultrafast x-ray diffraction. *Phys. Rev. B*, **87**:184301, (2013).

[121] U. Shymanovich, M. Nicoul, J. Blums, K. Sokolowski-Tinten, A. Tarasevitch, T. Wietler, M. Horn von Hoegen, and D. von der Linde. Diffraction of strongly convergent X-rays from picosecond acoustic transients. *Appl. Phys. A*, **87**(1):7–11, (2007).

[122] K. Sokolowski-Tinten, X. Shen, Q. Zheng, T. Chase, R. Coffee, M. Jerman, R. K. Li, M. Ligges, I. Makasyuk, M. Mo, A. H. Reid, B. Rethfeld, T. Vecchione, S. P. Weathersby, H. A. Dürr, and X. J. Wang. Electron-lattice energy relaxation in laser-excited thin-film Au-insulator heterostructures studied by ultrafast MeV electron diffraction. *Struct. Dyn.*, **4**(5):054501, (2017).

[123] R. K. Srivastava, K. Greff, and J. Schmidhuber. Highway Networks. *arXiv*, (2015).

[124] D. Strickland and G. Mourou. Compression of amplified chirped optical pulses. *Opt. Commun.*, **55**(6):447–449, (1985).

[125] I. Sutskever, O. Vinyals, and Q. V. Le. Sequence to Sequence Learning with Neural Networks. In *Proceedings of the 27th International Conference on Neural Information Processing Systems*, volume **2** of *NIPS'14*, page 3104–3112. MIT Press, (2014).

[126] C. Szegedy, W. Liu, Y. Jia, P. Sermanet, S. Reed, D. Anguelov, D. Erhan, V. Vanhoucke, and A. Rabinovich. Going deeper with convolutions. In *2015 IEEE Conference on Computer Vision and Pattern Recognition (CVPR)*, pages 1–9, (2015).

[127] S. Takagi. A Dynamical Theory of Diffraction for a Distorted Crystal. *J. Phys. Soc. Jpn.*, **26**(5):1239–1253, (1969).

[128] D. Taupin. Théorie dynamique de la diffraction des rayons X par les cristaux déformés. *Bulletin de la Société française de Minéralogie et de Cristallographie*, **87**, (1964).

[129] C. Thomsen, H. T. Grahn, H. J. Maris, and J. Tauc. Surface generation and detection of phonons by picosecond light pulses. *Phys. Rev. B*, **34**:4129–4138, (1986).

[130] J. Tompson, A. Jain, Y. LeCun, and C. Bregler. Joint Training of a Convolutional Network and a Graphical Model for Human Pose Estimation. In *Proceedings of the 27th International Conference on Neural Information Processing Systems - Volume 1*, NIPS'14, page 1799–1807. MIT Press, (2014).

[131] I. Vartanyants, C. Ern, W. Donner, H. Dosch, and W. Caliebe. Strain profiles in epitaxial films from x-ray Bragg diffraction phases. *Appl. Phys. Lett.*, **77**(24):3929–3931, (2000).

[132] D. von der Linde, K. Sokolowski-Tinten, C. Blome, C. Dietrich, A. Tarasevitch, A. Cavalleri, and A. Squier. 'Ultrafast' Extended to X-Rays: Femtosecond Time-Resolved X-Ray Diffraction. *Z. Phys. Chem.*, **215**:1527–1541, (2001).

[133] A. von Reppert, M. Mattern, J.-E. Pudell, S. P. Zeuschner, K. Dumesnil, and M. Bargheer. Unconventional picosecond strain pulses resulting from the saturation of magnetic stress within a photoexcited rare earth layer. *Struct. Dyn.*, **7**(2):024303, (2020).

[134] A. von Reppert, L. Willig, J.-E. Pudell, M. Rössle, W. Leitenberger, M. Herzog, F. Ganss, O. Hellwig, and M. Bargheer. Ultrafast laser generated strain in granular and continuous FePt thin films. *Appl. Phys. Lett.*, **113**(12):123101, (2018).

[135] L. Waldecker, R. Bertoni, R. Ernstorfer, and J. Vorberger. Electron-Phonon Coupling and Energy Flow in a Simple Metal beyond the Two-Temperature Approximation. *Phys. Rev. X*, **6**:021003, (2016).

[136] X. Wang, S. Nie, J. Li, R. Clinite, J. E. Clark, and J. Cao. Temperature dependence of electron-phonon thermalization and its correlation to ultrafast magnetism. *Phys. Rev. B*, **81**:220301, (2010).

[137] H. Wen, P. Chen, M. P. Cosgriff, D. A. Walko, J. H. Lee, C. Adamo, R. D. Schaller, J. F. Ihlefeld, E. M. Dufresne, D. G. Schlom, P. G. Evans, J. W. Freeland, and Y. Li. Electronic Origin of Ultrafast Photoinduced Strain in $BiFeO_3$. *Phys. Rev. Lett.*, **110**:037601, (2013).

[138] O. B. Wright. Ultrafast nonequilibrium stress generation in gold and silver. *Phys. Rev. B*, **49**:9985–9988, (1994).

[139] H. Wu, J. Zhang, K. Huang, K. Liang, and Y. Yu. FastFCN: Rethinking Dilated Convolution in the Backbone for Semantic Segmentation. *arXiv*, (2019).

[140] M. D. Zeiler and R. Fergus. Visualizing and Understanding Convolutional Networks. In *Fleet D., Pajdla T., Schiele B., Tuytelaars T. (eds) Computer Vision – ECCV 2014*, volume **8689**. Springer, (2014).

[141] S. P. Zeuschner, T. Parpiiev, T. Pezeril, A. Hillion, K. Dumesnil, A. Anane, J. Pudell, L. Willig, M. Rössle, M. Herzog, A. von Reppert, and M. Bargheer. Tracking picosecond strain pulses in heterostructures that exhibit giant magnetostriction. *Struct. Dyn.*, **6**(2):024302, (2019).

[142] N. Zhavoronkov, Y. Gritsai, M. Bargheer, M. Woerner, T. Elsaesser, F. Zamponi, I. Uschmann, and E. Förster. Microfocus Cu K? source for femtosecond x-ray science. *Opt. Lett.*, **30**(13):1737–1739, (2005).

[143] A. G. Zhidkov, S. A. Pikuz, A. Y. Faenov, O. V. Chefonov, A. V. Ovchinnikov, M. B. Agranat, and A. Zigler. Generation of hard x rays by femtosecond laser pulse interaction with solid targets in atmosphere. *Opt. Lett.*, **37**(5):884–886, (2012).

Appendix

A Diffractometry of the Au/GaAs sample

Figure 51 shows static X-ray diffraction measurements obtained with a Bruker D8 Advance diffractometer with a copper anode at 40 keV and 40 mA. As can be seen, the Au (111) peak is the dominant gold peak. The (220) peak is hidden in the shoulder of the GaAs(400) peak.

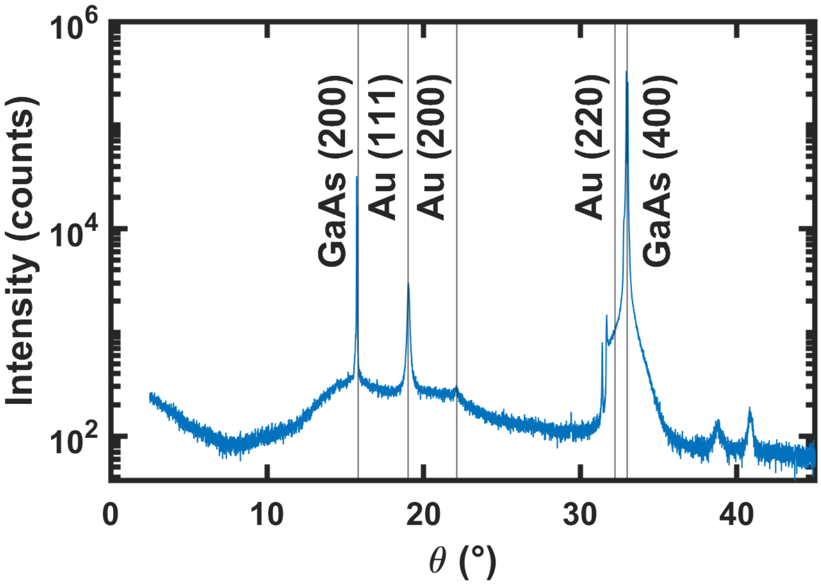

Figure 51: **Static diffractometry of the Au/GaAs sample.** This figure shows the static diffractometry spectrum of the gold on GaAs sample. The peaks at the left edge of the (400) GaAs peak are GaAs peaks originating from X-rays at a different wavelength emitted by a small amount of wolfram from the cathode, which is unintentionally deposited on the anode with time. The (111) peak of gold is clearly the dominant one for gold.

B Electron-phonon coupling strength in palladium

To determine the electron-phonon coupling strength Marius Milnikel has performed fluence dependent measurements of the transient Debye-Waller effect on laser-excited 17 nm thick polycrystalline films of palladium on top of a Si_3N_4 substrate. The diffraction patterns were integrated azimuthally. By fitting Gaussian peaks superimposed on a linear background to the data, the transient evolution of the diffraction intensity can be determined for every Bragg peak.

It was proven that the lattice response is completely incoherent and yet Debye-Waller like by plotting the negative logarithm of the intensity normalized to the unpumped intensity $-\log(\frac{I_{hkl}(\Delta t)}{I^0_{hkl}})$ against the squared length of the reciprocal lattice vector G^2_{khl} for the respective Bragg peak yielding a linear dependence. The resulting r.m.s displacement was converted to a temperature rise by using the results of Gao et al. [31].

The transient temperature rise as a function of time delay for different fluences is shown in figure 52. The solid lines represent fits to the data using a two temperature model calculation. A constant electron-phonon coupling strength of $G = 1.4 \times 10^{18}\,\frac{\mathrm{W}}{\mathrm{m^3\,K}}$ yields the best result for all fluences.

Fitting a simple exponential curve to all data sets delivers a coupling time of around half a picosecond without a pronounced fluence dependence in the given temperature range. This is fast compared to the relevant time scales of the acoustic wave emission discussed in this work. For further information and a more detailed discussion see the dissertation of Marius Milnikel [77].

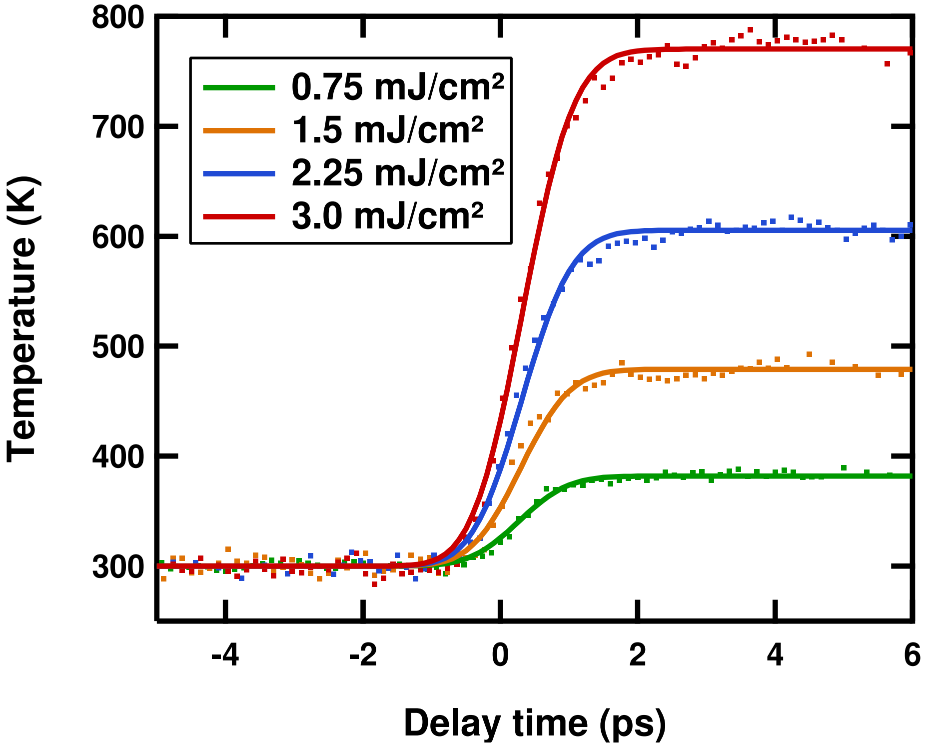

Figure 52: **Debye-Waller experiments on palladium.** The graph shows the temperature as a function of delay time inside the palladium film after optical excitation for different fluences. The solid lines represent fits to the experimental data using a two temperature simulation with a constant electron-phonon coupling strength of $G = 1.4 \times 10^{18} \, \frac{\mathrm{W}}{\mathrm{m^3\,K}}$.

C Matlab code

In this section, the Matlab code used for this work is given. The code for the calculation of transient diffraction patterns has already been reported in reference [1].

The deep learning tasks were performed in the framework of the Matlab experiment manager, which requires a setup function as an input to train the respective neural network.

1. Creation of training data sets for deep neural networks

```matlab
%% Parameters of the pulse
tmin = 160;         % Minimum and maximum thickness
tmax = 180;
Rmin = 0.25;        % Minimum and maximum reflectivity
Rmax = 0.6;
avStrainMin = 1e-4; % Minimum and maximum average strain
avStrainMax = 1e-2;
NbrSin = 10;        % Number of Fourier coefficients
NbrCos = 0;

idxStart    = 1;
idxEnd      = 30000;

%% Parameters of the DXRD calculations
ThetaMin    = -0.5952;
ThetaMax    = 0.5958;
dTheta      = 0.0045455;
TMin        = 0;
dt          = 2;
TMax        = 100;

theta       = (ThetaMin:dTheta:ThetaMax)';
time        = TMin:dt:TMax;

%% Create Parameters, calculate diffraction patterns and save everything
for ijk = idxStart:idxEnd
    % Choose the average strain and the Fourier coefficients; log10 ...
       ensures
    % uniform distribution over orders of magnitude
    avStrain    = round(10.^(-((-log10(avStrainMin) - ...
    -log10(avStrainMax))*rand + -log10(avStrainMax))), 6);
    t           = (tmax-tmin)*rand+tmin;
    R           = (Rmax-Rmin)*rand+Rmin;

    % This function chooses Fourier coefficients randomly, builds the
    % bipolar pulse and normalizes it to the correct average strain
    [BipolarPulse, FC]  = Fourier(2*t, NbrSin, NbrCos, avStrain);
    Pars                = [avStrain; t; R; FC]; % Parameter Vector

    % Create the result folder and save the parameters
    H = DataHash(Pars);
    ResultFolder = fullfile('Data', H);
    mkdir(ResultFolder);
    save(fullfile(ResultFolder, 'FC'), 'Pars')

    % Simulate and save TRXD and convoluted TRXD (cTRXD)
    [cTRXD, TRXD] = modeling(BipolarPulse, R, theta, time);
    save(fullfile(ResultFolder, 'Results'), 'cTRXD', 'CRC');

    % Display status
```

```
        disp(['Simulation ' num2str(ijk-idxStart+1) ' of '...
        num2str(idxEnd-idxStart+1) ' finished']);
    end
```

2. Setup function for experiment manager

```
function [Xtrain,Ytrain,layers,options] = Setup_Function(params)
% Xtrain:   Diffraction patterns for training
% Ytrain:   Parameters for training
% layers:   Network architecture
% options:  Training options
% params:   Variables for training; only contains RNGseed

%% set parameters
rng(params.RNGseed)
inSize       = [224 224];     % Input size of the network architecture
TrainingDataSize = 30000;     % Size of training and validation set
addConst     = 1e-1;          % Additive constant
SNR          = 90;            % Signal to noise ratio
ValPat       = 5;             % Validation patience
ILR          = 5e-05;         % Initial learning rate

%% Load the data; v containts the parameters, M contains the ...
    diffraction patterns
[v,M] = importData('DataSetAu.mat',inSize, SNR, addConst, ...
    TrainingDataSize);

n       = size(M,3);    % Get number of imported pairs
idx     = randperm(n);  % Randomly permute the training set
valSize = floor(0.1*n); % Set size of validation set to 10 %

idxtrain     = idx(1:end-valSize);        % Set indices for training ...
    and validation
idxval       = idx(end-valSize+1:end);

Xtrain = M(:,:,idxtrain);               % Assign diffraction patterns ...
    and parameters
Ytrain = v(idxtrain,:);
[Ytrain,mu,sigma] = zscore(Ytrain);      % Normalize data using z-score

Xval = M(:,:,idxval);
Yval = v(idxval,:);
Yvalnorm = (Yval-mu)./sigma;

save('zscorePar', 'mu', 'sigma')         % Sava parameters to undo ...
    z-score after retrieval

%% Define network architecture
layers = getResNet18(outSize);  % Create ResNet18 with correct number ...
    of output parameters

%% Specify training options
options = trainingOptions('adam', ...
'InitialLearnRate',ILR, ...
'MaxEpochs',300, ...
'L2Regularization',5e-6,...
'Shuffle','every-epoch', ...
'ValidationFrequency',30, ...
'ValidationPatience', ValPat,...
'Verbose',false, ...
```

```
'MiniBatchSize', 256,...
'ValidationData',{Xval,Yvalnorm}, ...
'Plots','training-progress');
end
```

3. Training data import function

```
function [v,M] = importData(filename,inSize, SNR, addConst, SetSize)
% Import the training data and do some preprocessing
% v: Parameter vector
% M: Diffraction patterns
% filename: Name of the training data set
% inSize: Input size of the network architecture
% SNR: Signal to noise ratio
% addConst: Additive constant
% SetSize: Number of elements used for training

load(filename)
n = SetSize;                % Number of elements of the training data set
i = randperm(numel(Matrix));% Permute the elements to choose randomly
i = i(1:n);

for idx = 1:numel(i)
    % Preprocessing of parameter vector (1: avStrain, 2: thickness, 3:
    % reflectivity, 4-end: Fourier coefficients)
    v(idx,:)         = Vector{i(idx)};          % Assign parameters to v
    v(idx, 4:end)    = v(idx,4:end)./v(idx,1); % Normalize FC to av. ...
        strain
    v(idx, 1)        = log(v(idx,1));           % Take log of av. strain

    % Preprocessing of images
    img = imresize(Matrix{i(idx)},inSize(1:2)); % Resize images
    if SNR
    img = awgn(img, SNR);        % Add noise to the patterns
    end
    img = normLog(img, addConst);    % Add addConst and take log of ...
        patterns
    M(:,:,idx) = img;                % Assign patterns to array M
end
```

4. Analysis script for measured patterns with trained networks

```
clear; close
load('..\..\MRC_Au_DL.mat');     % Load the file containing the ...
    experimental data
idxTrial     = 1;                % Trial number, e.g. if a ...
    hyperparameter was varied
NbrTrials    = 10;               % Number of training iterations
inSize       = [224 224];        % Input size of the network
addConst     = 1e-1;             % Training addConst for undoing ...
    preprocessing
NbrSin       = 10;               % Number of FC coefficients
NbrCos       = 0;
NbrCoef = NbrSin + NbrCos;

% Create a list with all result folders for that trial
k = (1:NbrTrials)+NbrTrials*(idxTrial-1);

```

```
FolListC     = dir('Trial*');
m            = numel(FolListC);

jj = 1;
for i = 1:m
    for j = k
        if strcmp(FolListC(i).name, ['Trial_' num2str(j)])
        FolList(jj) = FolListC(i);
        jj = jj + 1;
        end
    end
end
n = numel(FolList);

% Analyze the experimental pattern with all trained networks in the list
for i = 1:n
    load(fullfile(FolList(i).folder, FolList(i).name, 'output.mat')); ...
              % Load network
    load(fullfile(FolList(i).folder, FolList(i).name, ...
        'zscorePar.mat'));    % Load z-score parameters

    % Analyze the measured time-resolved pattern (MTRXD)
    [ParPred, PulsePred] = testNetOnMRC(MTRXD, nnet, mu, sigma, ...
        NbrSin, NbrCos, addConst);
    Par(i,:)     = ParPred;       % Parameter array
    Pulse{i}     = PulsePred;     % Pulse cell
    RCint        = calcCRC(PulsePred, ParPred(3), theta, time); % ...
        Calculate the diffraction patterns
    Weight(i)    = 100*(100-MAPEmat(MRC, RCint));    % Define a weight
end

% Calculate the weighted results
Weight                    = Weight/sum(Weight);                 % ...
    Normalize the weights
[av_Strain, err_Strain] = weightedMean(Weight,Par(:,1));     % Mean of ...
    the average strain
[av_FC, err_FC] = weightedMean(Weight, Par(:,4:end));        % Mean of ...
    the Fourier coefficients
[av_t, err_t]     = weightedMean(Weight, Par(:, 2));         % Mean of ...
    the thickness
[av_R, err_R]     = weightedMean(Weight, Par(:, 3));         % Mean of ...
    the reflectivity

% Build the average pulse and Fourier coefficients
av_Pulse         = FourierFunctions.build(2*av_t, av_Strain, ...
    av_FC(1:NbrSin), ...
av_FC(NbrSin+1:NbrCoef));
av_FCn           = ...
    av_FC*av_Strain/FourierFunctions.averageStrainFC(2*av_t, ...
av_FC(1:NbrSin), av_FC(NbrSin+1:NbrCoef));

% Calculate the error
errFCn       = sqrt((av_Strain*err_FC).^2+(av_FC*err_Strain).^2);
relerrFCn    = abs(errFCn./av_FCn);
relerrd      = abs(err_t/av_t);
relerrR      = abs(err_R/av_R);

function [CoeffPred, PulsePred] = testNetOnMRC(Matrix, net, mu, ...
    sigma, NbrSin, NbrCos, addConst)
% This function prepares the measured data and gives it as an input ...
    to the
% network.
```

```
% Matrix contains the measured data.
% imageSize, net, mu and sigma are the parameters of the neural network

% Undo preprocessing of diffraction pattern
img                  = normLog(Matrix, addConst);
MRCprep(:, :, 1)     = img;

% Get the network predictions and undo preprocessing of parameters
score            = net.predict(MRCprep);
CoeffPred        = score.*sigma + mu;
CoeffPred(:,1)   = exp(CoeffPred(:,1));    % Undo the log in preparation

% Build the pulse
PulsePred = FourierFunctions.build(2*CoeffPred(2), CoeffPred(1), ...
    CoeffPred(4:3+NbrSin), CoeffPred(4+NbrSin:3+NbrSin+NbrCos));
end
```

Acknowledgment

I would like to thank all the people who supported me during my work on this thesis.

First of all, I want to express my sincere gratitude to my supervisor Klaus Sokolowski-Tinten. I really enjoyed the joined work, the scientific discussions and support, but also the nice working atmosphere.

I also thank Prof. Dr. Uwe Bovensiepen for the opportunity to do this work in his group. Besides that, I value the scientific input, discussions and the encouragement during my time as a member of the group.

Special thanks goes Philipp Krumey and Dr. Mohammadmahdi Afshari for countless shared hours and nights in the lab with a lot of work, but also a lot of fun.

I want to express my great appreciation to Dr. Alexander Tarasevitch for his support regarding the laser system. Thank you for the motivated help and the often short-term repairing efforts, whenever I had issues preventing me from progressing with my work.

I am very thankful for all members of the AG Bovensiepen for creating a great working atmosphere. It was always a pleasure to collaborate with you and besides working, spend various funny and easygoing hours at the coffee break, lunch, conferences or in our free time.

Special thanks goes to the supporting cast of our group: Tina Boese, Michael Bieske and Roland Kohn. Apart from help with the administration, mechanical problems or IT issues I enjoyed our coffee meetings and the discussions early in the morning, before most of the other group members arrived.

I really appreciated to embark on this journey with my fellow Ph.D. colleagues Yasin Beyazit, Manuel Bridger, Oscar Naranjo and Marius Milnikel. I really enjoyed all the fun, we had together, but also the support and helpful discussions in more difficult parts of the journey.

I also want to thank my family and friends, who were always my backbone and gave me strength in the more difficult times, especially my parents and my brothers.

Last but not least: I would like to thank my wife for standing by my side and sharing the time with me. Especially but not only, when the road was rocky and in the most difficult times of my life. I hope for many more wonderful years to come.

DOI: 10.17185/duepublico/76987
URN: urn:nbn:de:hbz:465-20221024-154109-4